AEROELASTIC ANALYSIS AND OPTIMIZATION OF MEMBRANE MICRO AIR VEHICLE WINGS

By

BRET KENNEDY STANFORD

A DISSERTATION PRESENTED TO THE GRADUATE SCHOOL
OF THE UNIVERSITY OF FLORIDA IN PARTIAL FULFILLMENT
OF THE REQUIREMENTS FOR THE DEGREE OF
DOCTOR OF PHILOSOPHY

UNIVERSITY OF FLORIDA

2008

To my family, despite making fun of me for being in school for so long
To Angel, despite making fun of me for a bunch of other reasons
And to Fatty too, for only scratching me when I really deserve it, which is often

ACKNOWLEDGMENTS

Thank you to Dr. Peter Ifju, who offered his guidance on a countless number of research projects, and still let me work on the ones he thought were dumb. Unquestionably the coolest, smartest, most up-beat professor I've ever been around.

Thank you to Dr. Rick Lind, for consistently pointing out when I need to shave, or get a haircut, or more frequently, both.

Thank you to Dr. Roberto Albertani, for sharing with me his passion for all things wind tunnel related, and for sharing his equipment up at the REEF.

Thank you to Dr. Raphael Haftka and Dr. David Bloomquist for serving on my committee and sitting through my long, scientifically-questionable presentations without complaining.

Thank you to Dr. Dragos Viieru, for imparting me with his vast knowledge of CFD.

Thank you to Dr. Wei Shyy, for all his help my first few semesters of grad school.

A final thank you to all the people who hung around the labs I worked in. Frank Boria, who helped teach me the real names for various tools and hardware, which had previously been known to me only as shiny metal things. A thanks-in-advance to Frank for taking all of my future phone calls concerning mortgages, insurance, child rearing, etc, no matter how distraught and hysterical they may be. Mujahid Abdulrahim, for discussing with me the ethics of returning a rental car completely caked in mud, and going in reverse through a drive-thru. Wu Pin, for relating countless unintentionally funny and creepy stories that I'll never forget, despite my best efforts. I'll always wonder how you got into this country.

TABLE OF CONTENTS

LIST OF TABLES

LIST OF FIGURES

Abstract of Dissertation Presented to the Graduate School
of the University of Florida in Partial Fulfillment of the
Requirements for the Degree of Doctor of Philosophy

AEROELASTIC ANALYSIS AND OPTIMIZATION OF MEMBRANE MICRO AIR VEHICLE WINGS

By

Bret Kennedy Stanford

May 2008

Chair: Peter Ifju
Major: Aerospace Engineering

Fixed-wing micro air vehicles are difficult to fly, due to their low Reynolds number, low aspect ratio nature: flow separation erodes wing efficiency, the wings are susceptible to rolling instabilities, wind gusts can be the same size as the flight speed, the range of stable center of gravity locations is very small, etc. Membrane aeroelasticity has been identified has a tenable method to alleviate these issues. These flexible wing structures are divided into two categories: load-alleviating or load-augmenting. This depends on the wing's topology, defined by a combination of stiff laminate composite members overlaid with a membrane sheet, similar to the venation patterns of insect wings. A series of well-validated variable-fidelity static aeroelastic models are developed to analyze the working mechanisms (cambering, washout) of membrane wing aerodynamics in terms of loads, wing deformation, and flow structures, for a small set of wing topologies. Two aeroelastic optimization schemes are then discussed. For a given wing topology, a series of numerical designed experiments utilize tailoring of laminate orientation and membrane pre-tension. Further generality can be obtained with aeroelastic topology optimization: locating an optimal distribution of laminate shells and membrane skin throughout the wing. Both optimization schemes consider several design metrics, optimal compromise designs, and experimental validation of superiority over baseline designs.

CHAPTER 1
INTRODUCTION

Motivation

The rapid convergence of unmanned aerial vehicles to continually smaller sizes and greater agility represents successful efforts along a multidisciplinary front. Technological advances in materials, fabrication, electronics, propulsion, actuators, sensors, modeling, and control have all contributed towards the viable candidacy of micro air vehicles (MAVs) for a plethora of tasks. MAVs are, by definition, a class of unmanned aircraft with a maximum size limited to 15 cm, capable of operating speeds of 15 m/s or less. Ideally, a MAV should be both inexpensive and expendable, used in situations where a larger vehicle would be impractical or impossible, to be flown either autonomously or by a remote pilot. Military and defense opportunities are perhaps easiest to envision (in the form of over-the-hill battlefield surveillance, bomb damage assessment, chemical weapon detection, etc.), though MAVs could also play a significant role in environmental, agriculture, wildlife, and traffic monitoring applications.

MAVs are notoriously difficult to fly; an expected consequence of a highly maneuverable and agile vehicle that must be flown either remotely or by autopilot [1]. The aerodynamics are beset by several unfavorable flight issues:

1. The operational Reynolds number for MAVs is typically between 10^4 and 10^5. Flow over the upper wing surface can be characterized by massive flow separation, a possible turbulent transition in the free shear layer, and then reattachment to the surface, leaving behind a separation bubble [2]. Such flow structures typically result in a loss of lift, and an increase in drag, and a drop in the overall efficiency [3].

2. The low aspect ratio wing (on the order of unity) promotes a large wing tip vortex swirling system [4], which interferes with the longitudinal circulation of the wing [5]. Entrainment of the aforementioned separated flow can lead to tip vortex destabilization [6]; the resulting bilateral asymmetry may be the cause of the rolling instabilities known to plague MAV flight.

3. Sudden wind gusts may be of the same order of magnitude as the vehicle flight speed (10-15 m/s). Maintaining smooth controllable flight can be difficult [7] [8].

4. The range of flyable (statically stable) CG locations is generally only a few millimeters long, which represents a strenuous weight management challenge [9].

These problems, along with a broad range of dynamics and control issues, can be alleviated through the appropriate use of wing shape adaptation. Active morphing mechanisms have been successfully used on a small class of unmanned air vehicles [1], but the limited energy budgets and size constraints of micro air vehicles make such an option, at present writing, infeasible. As such, the current work is restricted to passive shape adaptation.

Passive shape adaptation can be successfully built into a MAV wing through the use of a flexible membrane skin [10]. The basic structure of these vehicles is built around a composite laminate skeleton. Bi-directional graphite/epoxy plain weave or uni-directional plies are usually the materials of choice, due to durability, low weight, high strength, and ease of fabrication: all qualities well-exploited in the aviation industry [11]. The carbon fiber skeleton is affixed to an extensible membrane skin, of which several choices are available: latex, silicone, plastic sheets, or polyester [12]. The distribution of carbon fiber and membrane skin in the wing determines the aeroelastic response, and is demonstrated by two distinct designs. The first utilizes thin strips of uni-directional carbon fiber imbedded within the membrane skin, oriented in the chordwise direction (Figure 1-1). The trailing edge of the batten-reinforced (BR) design is unconstrained, and the resulting nose-down geometric twist of each flexible wing section should alleviate the flight loads: decrease in C_D, decrease in $C_{L\alpha}$, delayed stall (as compared to a rigid wing) [13].

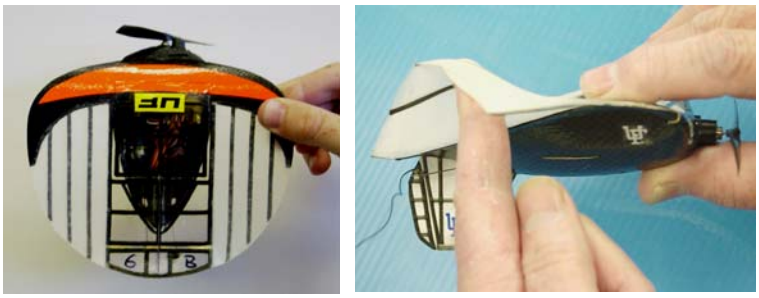

Figure 1-1. Batten-reinforced membrane wing design.

A second design leaves the interior of the membrane skin unconstrained, while the perimeter of the skin is sealed to a thin curved strip of carbon fiber (Figure 1-2). The perimeter-reinforced (PR) wing deformation is closer in nature to an aerodynamic twist. Both the leading and the trailing edges of each membrane section are constrained by the relatively-stiff carbon fiber. The positive cambering (inflation) of the wing should lead to an increase in C_L and a decrease (more negative) in $C_{m\alpha}$ [14].

Figure 1-2. Perimeter-reinforced membrane wing design.

While both of these wing structures can adequately perform their intended tasks (load alleviation for the BR wing, load enhancement for the PR wing), several sizing/stiffness variables exist within both designs, leading to an aeroelastic tailoring problem. Conventional variables such as the laminate fiber orientation [11] can be considered, but the directional stiffness induced by varying the pre-tension within the membrane skin may play a larger role within the aeroelastic response [15]. Systematic optimization of a single design metric will typically lead to a wing structure with poor performance in other important aspects. For example, tailoring the PR wing structure for maximum static stability may provoke an unacceptable drag penalty, and vice-versa. Of the aerodynamic performance metrics considered here (lift, drag, efficiency, static stability, gust suppression, and mass) many are expected to conflict, as with most engineering optimization applications. Formal multi-objective optimization procedures can be used to tailor flexible MAV wing designs that strike an adequate

compromise between conflicting metrics, filling in the trade-off curves.

While thorough exploration of this aeroelastic tailoring design space can provide a fundamental understanding of the relationship between spatial stiffness distribution and aerodynamic performance in a flexible MAV wing, further steps towards generality can be achieved by removing the constraint that the wing structures must utilize a BR or a PR design. Topology optimization is typically used to find the location of holes within a homogenous structure, by minimizing compliance under a constraint upon the volume fraction [16]. Here it is used to find the location of membrane skin within a carbon fiber skeleton that will optimize a given aerodynamic objective function.

This work will be able to highlight wing topologies with superior efficacy to those designs considered above (for example, a wing with better gust suppression qualities than the BR wing), as well as designs that strike a compromise between conflicting metrics (for example, a topological combination of the BR and the PR wings). While the results may be more rewarding than those obtained from tailoring, aeroelastic topology optimization is significantly more complex. Tailoring requires 5-10 sizing and stiffness variables, but the topology optimization may utilize thousands of variables: the wing is divided into a series of panels, each of which may be membrane or carbon fiber. This necessitates a gradient-based algorithm, while evolutionary algorithms or response surface approaches are feasible for the former problem.

Both aeroelastic tailoring and topology optimization are effective tools for exploiting the passive shape adaptation of flexible MAV wings, but the computational cost is prohibitive. It is not uncommon for aeroelastic optimization studies to require hundreds, or even thousands, of function evaluations. Numerical modeling of flexible MAV wings is very challenging and expensive: flow separation, transition, and reattachment [17], vortex shedding and pairing [18],

and wing tip vortex formation/destabilization [6] are all known to occur within the flow over low aspect ratio wings at low Reynolds numbers. Structurally, the membrane skins used for MAV construction are beset by both geometric and material nonlinearities [19]; the orthotropic nature of the carbon fiber laminates must also be computed.

At present, no numerical model exists which can accurately predict all of the three dimensional unsteady features of an elastic MAV wing (flow transition being a particular challenge [8]). As such, an important step in aeroelastic optimization of MAV wings is careful development of lower-fidelity numerical models. Both inviscid vortex lattice methods and laminar Navier-Stokes solvers are investigated, along with linear and nonlinear membrane finite elements (only static aeroelastic models are considered here). In light of the low-fidelity tools that must be used (to maintain computational cost at a reasonable level), a second important step in aeroelastic optimization is extensive experimental model validation. Three levels of model validation are employed: validation of the structural response of individual components of the membrane wing, validation of the aeroelastic behavior of various baseline membrane wings, and validation of the superiority of the computed optimal wings (found either through tailoring or topology optimization) over the baselines.

Further complications arise from complex objective functions. As discussed above, gust response is an important performance metric for micro air vehicles [7], but systematic optimization would require an unsteady model, non-homogenous incoming flow, and subsequent time integration. Similarly, delaying the onset of wing stall would require several sub-iterations to locate the stalling angle. Both objectives can be reasonably replaced by a minimization of the lift slope, which is more amenable to a systematic optimization. Finally, the computational complexity is further exacerbated by the multi-objective nature of the problem. Wing structures

that optimize a single objective function are of limited value; of greater importance is the array of designs that lie along the Pareto optimal front.

This front is a trade-off curve comprised of non-dominated designs, one of which can be selected based on additional considerations not included in the optimization: manufacturability, flight specifications (duration, payload), etc. Computation of the Pareto front is costly when gradient-based search routines are used for optimization, typically involving successive optimization runs with various convex combinations of the objective functions. The success of this technique depends on the convexity of the Pareto optimal front. More efficient methods for computing the Pareto front are available if evolutionary algorithms or response surface methods are employed.

Problem Statement

The static aeroelasticity of membrane micro air vehicle wings represents the intersection of several rich aerodynamics and mechanics problems; numerical modeling can be very challenging and expensive. Furthermore, MAVs are beset with many detrimental flight issues, and are very difficult to fly: systematic numerical optimization schemes can be used to offset these problems, improving flight duration, gust suppression, or static stability. Many optimization studies can be considered for MAVs; the current work utilizes aeroelastic optimization, which will require hundreds of costly function evaluations to adequately converge to an optimal design. As the feasibility of such a scheme relies on a moderate computational cost, what is the lowest fidelity aeroelastic model that can be appropriately used?

Model development requires extensive experimental validation, and several challenges exist here as well. The forces generated by a MAV wing are very small, and highly-sensitive instrumentation is needed. For deformation measurements, only vision-based non-contacting methods are appropriate. What particular components are required to construct an adequate

experimental test-bed for flexible MAVs? What performance metrics should be compared between numerical and experimental results for sufficient model validation?

Upon suitable validation of the aeroelastic model, two optimization studies are developed: tailoring and topology optimization. Considering the former, with a given spatial distribution of laminated carbon fiber and membrane skin throughout the wing, what is the optimal chordwise and spanwise membrane pre-tension and carbon fiber laminate lay-up schedule? For the aeroelastic topology optimization studies, with a given membrane pre-tension and laminate orientation, what is the optimal distribution of carbon fiber and membrane skin throughout the wing? What performance metrics should be optimized? As these metrics will surely conflict, what multi-objective optimization schemes are appropriate for computation of the Pareto front? Can the numerically-indicated optimal wing design structures be built and tested, and will the experimental results also indicate superiority over similarly-tested baseline designs?

Dissertation Outline

This work begins with a detailed literature review of micro air vehicle aerodynamics (low Reynolds number flows, low aspect ratio wings, unsteady flow phenomena), aeroelasticity (membrane sailwings, flexible filaments), and optimization (rigid wing airfoil and planform optimization, tailoring). I review the literature pertaining to topology optimization as well, with a particular emphasis upon aeronautical and aeroelastic applications.

I then discuss the apparatus and procedures used for experimental characterization of the membrane micro air vehicle wings. This includes a low-speed closed loop wind tunnel, a high sensitivity sting balance, and a visual image correlation system. Information is also given detailing wing fabrication and preparation. I summarize the computational framework, including both linear and nonlinear structural finite element models. Three-dimensional viscous and inviscid flow solvers are formulated, along with aeroelastic coupling and ad hoc techniques

devised to handle the membrane skin pre-tension. The estimated validity range of each model is discussed.

I detail the deformation patterns, flow structures, and aerodynamic characterization of a series of baseline flexible and rigid MAV wings, obtained both numerically and experimentally for comparison purposes. Once the predictive capability of the aeroelastic model is well-verified, these data sets are studied to uncover the working mechanisms behind the passive shape adaptation and their associated aerodynamic advantages.

I then use a non-standard aeroelastic tailoring study to identify the optimal wing type and structural composition for a given objective function, as well as various combinations thereof. Wing types are limited to rigid, batten-reinforced, and perimeter-reinforced designs; structural composition variables include anisotropic membrane pre-tension and laminate lay-up schedule. Multi-objective optimization is conducted using a design of experiments approach, with a series of aerodynamic coefficients and derivatives as metrics. The tailoring concludes with experimental validation of the performance of selected optimal designs.

Finally, I formulate a computational framework for aeroelastic topology optimization of a membrane micro air vehicle wing. A gradient-based search is used, with analytically computed sensitivities of the same aerodynamic metrics as used above. The optimal wing topology is discussed as a function of flight condition, grid density, initial guess, and design metric. I optimize a convex combination of two conflicting objective functions to construct the Pareto front, with a demonstrated superiority over the baseline wing structures employed in the tailoring study. As before, the work concludes with experimental validation of the performance of selected optimal designs.

Contributions

1. Develop a set of variable-fidelity aeroelastic models for low Reynolds number, low aspect ratio membrane micro air vehicle wings.

2. Develop a highly-sensitive non-intrusive experimental test-bed for model deformation and flight loads.

3. Optimization-based system identification of the wing structure's material properties.

4. Experimental aeroelastic model validation of flight loads and wing deformation.

5. Optimize multiple flight metrics by tailoring membrane pre-tension and laminate orientation.

6. Develop computational framework for topology optimization of membrane wings, with an analytical sensitivity analysis of the coupled aeroelastic system.

7. Able to provide scientific insight into the relationship between optimal wing flexibility, flow structures, and the resulting beneficial effects upon flight loads and efficiency.

8. Experimental validation of the superiority of selected optimal designs over baselines.

CHAPTER 2
LITERATURE REVIEW

Micro Air Vehicle Aerodynamics

A long history of flight testing, computational modeling, and wind tunnel work has generally pushed the design methodology of successful fixed wing MAVs to a thin, cambered, low aspect ratio "flying wing". Maximizing the wing area for a given size constraint obviously leads to a low aspect ratio design. Further desire to minimize the size of a MAV negates the use of horizontal stabilizers, replaced with a reflex airfoil for longitudinal static stability, wherein negative camber present towards the trailing edge helps offset the longitudinal pitching moment of the remainder of the wing. The superiority of thin wings for MAV applications can be shown by both three dimensional inviscid simulations [20] and two-dimensional viscous simulations [21] [22], where the drop in the adverse pressure gradients increases the lift and decreases the drag towards stall. Similar tools, as well as wind tunnel testing, indicates the advantage of cambered wings over flat plates [5]; beyond the obvious increase in lift, higher lift-to-drag ratios are reported by Laitone [23]. Much work has also been done on locating suitable MAV planform shapes. Torres identifies the inverse-Zimmerman as ideal, based upon size restrictions, required angle of attack, and drag performance; the optimum shifts to an elliptical shape as the aspect ratio is increased [3].

Low Reynolds Number Flows

Low Reynolds number laminar flow is likely to separate against an adverse pressure gradient aft of the pressure recovery location (velocity peak) on the upper wing surface, even for fairly low angles of attack. The formation of a turbulent boundary layer aft of a separation bubble is a very mutable process: Reynolds number, pressure distributions, airfoil geometry, surface roughness, turbulence intensity, acoustic noise, wall heating, and α-direction (whether

the angle of attack is being increased or decreased can lead to hysteresis [24]) are all cited by Young and Horton [2] as highly influential on the formation of a bubble. Furthermore, the flow will only reattach to the surface if there is enough energy to maintain circulating flow against dissipation [25].

An extensive survey of low Reynolds number ($3 \cdot 10^4$ - $5 \cdot 10^5$) airfoils is given by Carmichael [17] (there are quite a few others, as reviewed by Shyy et al. [26]). The study finds that, for the lower end of tested Reynolds numbers, the laminar separated flow does not have time to reattach to the surface. Above $5 \cdot 10^4$, the flow will reattach, forming a long separation bubble over the wing. At the upper end of the range of Reynolds numbers discussed by Carmichael, the size of the bubble decreases, generally resulting in a decrease in form drag. Increasing the angle of attack generally enhances the turbulence in the flow, which can also prompt quicker reattachment and shorter bubbles [8]. The length of the separation bubble can generally be inferred from the plateau-like behavior of the pressure distribution: the flow speeds up before the bubble (dropping the pressure), and slows down after the bubble [27].

This description is a time-averaged scenario: in an unsteady sense, the inflectional velocity profile across the separation bubble can develop inviscid Kelvin-Helmhotlz instabilities and cause the shear layer to roll up. This leads to periodic vortex shedding and the required matching downstream [18], and can cause the separation bubble to move back and forth [28]. Further work detailing low Reynolds number flow over rigid airfoils can be found by Nagamatsu [29], Masad and Malik [30], and Schroeder and Baeder [31].

Low Aspect Ratio Wings

Early work in low aspect ratio aerodynamics was sparked by an inability to fit experimental data with linear aerodynamics theories, as reported by Winter [32] for aspect ratios between 1.0 and 1.25. The measured lift is typically higher than predicted (similar to vortex lift

discrepancies seen on delta wings [27]), as the strong wing tip vortices interfere with the longitudinal wing circulation. The most obvious indication of such an interaction is the high stalling angles of low aspect ratio wings, where the downward momentum of the tip vortices can keep the flow attached to the upper wing surface. Experimental work by Sathaye et al. [33] using an array of pressure ports was able to confirm the deviation of the lift distribution from elliptic wing theory.

Lian et al. [28] report a computed dip in the previously constant pressure coefficients over the upper wing surface at 75% of the semi-span for high angles of attack, but only minor changes on the bottom surface at the wing tip. These low pressure cells at the wing tip will grow in intensity and spread inward towards the root as the angle of attack (and thus the strength of the swirling system) is increased [34]. The cells are a nonlinear contribution to the wing's lift; their growth with angle of attack increases $C_{L\alpha}$ with angle of attack as well. Torres [3] gives a general cutoff between a linear and a nonlinear C_L-α relationship at an aspect ratio of 1.25. Low aspect ratio corrections to the lift predicted by linear theory (among many) are given by Bartlett and Vidal [35], while Polhamus [36] is able to collapse the measured profile drag data at various aspect ratios to a single curve through the use of an effective two-dimensional lift coefficient.

Further experimental work is given by Kaplan et al. [37], who use measurements of the trailing vortex structure off of low aspect ratio flat plates for adequate comparison with force balance measurements. The authors indicate that the nonlinear lift curves may also be caused by a loss of leading edge suction, and a rotation of the force vector into a flow-normal direction. Viieru et al. [38] discusses the use of endplates to temper the induced drag from the tip vortices, with reported improvements in the lift-to-drag ratio at small to moderate angles of attack.

Low Reynolds Number - Low Aspect Ratio Interactions

Several interactions between the low aspect ratio and low Reynolds number aerodynamics

of MAVs are reported in the literature. Mueller and DeLaurier cite aspect ratio as the most important design variable, followed by wing planform and Reynolds number. Free stream turbulence intensity and trailing edge geometry are reported to be non-factors, and Reynolds number is only important near stall [39]. Flow visualization experiments by Gursul et al. [40] on swept, non-slender, low aspect ratio wings find the presence of primary and secondary vortices, with stagnant flow regions outboard of the former. Vortex merging and other unsteady interactions within the shear layers are found to be highly dependent on Reynolds number.

Kaplan et al. [37] report a fluctuation in the location of the vortex core off of a semi-elliptical wing at 8,000 Reynolds number. Numerical simulations and flow visualization by Tang and Zhu [6] of an accelerating elliptical wing show an unstable interaction between a longitudinal secondary separated vortex and the tip vortices. This destabilization (for angles of attack above 11º) causes the tip vortex system to swing back and forth along the wing, leading to bilateral asymmetry problems in roll. The authors also note a stationary separated vortex (rather than the customary shedding) for angles above 33º, possibly due to the vertical components of the tip vortices.

Cosyn and Vierendeels [41], Brion et al. [42], and Stanford et al. [43], discuss numerical wing modeling of lift and drag for comparison with wind tunnel experiments: the lack of a three-dimensional turbulent-transition model is generally cited as the reason for poor correlation at higher angles of attack. Results documenting the aerodynamics of a complete micro air vehicle (wing with fuselage, stabilizers, propellers, etc) are scarce: wind tunnel experimentation by Zhan et al. document longitudinal and lateral stability as a function of vertical stabilizer placement and wing sweep [44]. Similar stability data is given by Ramamurti et al. [45] for a MAV wing with counter-rotating propellers.

Gyllhem et al. [46] reports that the presence of a fuselage, motor, and stabilizers surprisingly improves the computed maximum lift and stall angle (compared to simulations with just the wing), but increases the drag as well. Experimental work by Albertani [47] finds just the opposite: a decrease in lift of the entire vehicle, but less of a penalty when passive shape adaptation is built into the wing. Waszak et al. [13] are able to show significant improvements in efficiency if a streamlined MAV fuselage is used.

Rigid Wing Optimization

Though the main scope of the current work is to improve the aerodynamic qualities of fixed micro air vehicle wings through the judicious use of aeroelastic membrane structures, much successful work has been done with multidisciplinary optimization of the shape, size, and components of a rigid MAV wing. These studies must often make use of low fidelity models due to the large number of function evaluations required for a typical optimization run, and may not be able to capture the complicated flow physics described above. Nonetheless, insight into the relationship between sets of sizing/shape variables and a given objective function can still be gained.

Early work is given by Morris [48], who finds the smallest vehicle that will satisfy given constraints throughout a theoretical mission, using several empirical and analytical expressions for the performance evaluation. Rais-Rohani and Hicks investigate a similar problem, using a vortex lattice method (for computations of aerodynamic performance and stability, along with propulsion and weight modules) and an extended interior penalty function method to reduce the size of a biplane MAV [49]. Kajiwara and Haftka emphasize the unconventional need for simultaneous design of the aerodynamic and the control systems at the micro air vehicle scale, due to limited energy budgets [50].

Torres [3] uses a genetic algorithm to minimize a weighted combination of payload, endurance, and agility metrics, with various discrete (wing and tail planform) and continuous (aspect ratio, propeller location, angle of attack, etc) variables. Aerodynamic analysis is provided by a combination of experimental data, analytical methods, and interpolation techniques. The author cites convergence problems stemming from the discrete variables. Genetic algorithms are also used in the work of Lundström and Krus [51] and Ng et al. [52]. The latter indicates that these algorithms are more suited for the potentially disjointed design spaces presented by MAV optimization efforts. A comparison between a genetic algorithm and gradient-based sequential quadratic programming used to design winglets for a swept wing MAV indicates the superiority of the former, with a vortex lattice method used for aerodynamic analysis. However, a genetic algorithm may only be feasible for lower fidelity tools, due to the large number of function evaluations required for convergence.

Higher fidelity aerodynamics tools (namely, thin-layer or full Navier-Stokes equation solvers) are employed in recent studies. For example, a combined 2-D thin layer Navier-Stokes model and a 3-D panel method is used by Sloan et al. [53], who use the outcome to construct a response surface to optimize the wing geometry for minimum power consumption. As above, the study reveals the superiority of thin wings, and finds that optimal airfoil shapes are insensitive to aspect ratio. Lian et al. [54] use a full Navier-Stokes solver to maximize the lift-to-drag ratio of a rigid MAV wing subject to various lift and wing convexity constraints, with sequential quadratic programming search methods. Efficiency improvements are feasible by decreasing the camber at the root and increasing at the tip, thereby decreasing the amount of flow separation. Improvements are found to be more substantial at moderate angles of attack.

Given the computational complexities associated with MAV simulation, several research

efforts use wind tunnel hardware-in-the-loop for optimization. Load measurements from a sting balance are fed into an optimizer as the objective function or constraints. Genetic or other types of evolutionary algorithms are invariably used, as a sensitivity analysis requires finite difference computations which are easily distorted by experimental error. Examples with MAVs are given by Boria et al. [55] (optimize lift and efficiency with airfoil morphing), Hunt et al. [56] (optimize the forward velocity and efficiency of an ornithopter, with flapping rate and tail position as variables), and Day [57] (planform optimization of a wing with variable feather lengths).

Micro Air Vehicle Aeroelasticity

The role of aeroelasticity in the study of membrane micro air vehicle wings differs greatly from conventional aircraft. While certain aeroelastic instabilities do exist (typically involving the lift slope approaching infinity [15], unstable flapping of a poorly constrained trailing edge [58], or luffing [59]), classical problems like torsional divergence and flutter have little bearing on MAV design, due to the low aspect ratio nature of the wings and the small operating dynamic pressures [60]. Great savings are available in the form of load redistribution however, as mentioned above: potential improvements in lift, drag, stall, and longitudinal static stability can all be obtained. Lateral control improvements are also obtainable with membrane wings [1] [61]. Furthermore, chordwise bending of a wing section (aerodynamic twist) can often be ignored in conventional aircraft (except, for example, when constructed from laminates with many off-axis plies [11]), but such deformation is very prevalent in low aspect ratio membrane wings.

Two-Dimensional Airfoils

The aeroelastic membrane structure is dominated by three-dimensional structural and aerodynamic effects, but much useful insight can be gained from two-dimensional simulations and experiments. Such endeavors are obviously easier to undertake for PR-type membrane wings, but three-dimensional reinforcement must be taken into account for a pure membrane (or

string in two dimensions) with geometric twist, as the structure alone cannot sustain a flight load in a stable manner. A second option involves considering an elastic sheet with some bending/flexural stiffness. A large variety of work can be found in the literature concerning two-dimensional flexible beams in flow. For problems on a MAV scale, work tends to focus on flags and organic structures such as leaves, seaweed, etc.

Fitt and Pope [58] derive an integro-differential flag equation for the shape of a thin membrane with bending stiffness in unsteady inviscid flow, considering both a hinged and a clamped leading edge boundary condition. Argentina and Mahadevan [62] solve a similar problem, and are able to predict a critical speed that marks the onset of an unstable flapping vibration, noting that the complex instability is similar to the resonance between a pivoting airfoil in flow and a hinged-free beam vibration. Over-prediction of the unstable flapping speed (when compared to experimental data) leads to the possibility of a stability mechanism wherein skin friction induces tension in the membrane. Alben et al. [63] discuss the streamlining of a two-dimensional flexible filament for drag reduction. In particular, they are able to show that the drag on a filament at high angles of attack decreases from the rigid U_∞^2 scaling to $U_\infty^{4/3}$.

Early work in the study of membrane wings without bending stiffness is given by Voelz [64], who describes the classical two-dimensional sail equation: an inextensible membrane with slack, fixed at the leading and trailing edges, immersed in incompressible, irrotational, inviscid steady flow. Using thin airfoil theory, along with a small angle of attack assumption, Voelz is able to derive a linear integro-differential equation for the shape of the sail as a function of incidence, freestream velocity, and slack ratio. Various numerical solution methods are available, including those by Thwaites [65] (eigenfunction methods) and Nielsen [66] (Fourier series methods), to solve for lift, pitching moments, and membrane tension.

Multiple solutions are found to exist at small angles of attack with a finite slack ratio: approaching 0° from negative angles provides a negatively-cambered sail, though the opposite is true if this mark is approached from a positive value. The sail is uncertain as to which side of the chord-line it should lie [65], a phenomenon which ultimately manifests itself in the form of a hysteresis loop [15]. Variations on this problem are considered by Haselgrove and Tuck [67], where the trailing edge of the membrane is attached to an inextensible rope, thereby introducing a combination of adaptive aerodynamic and geometric twist. Increasing the length of the rope is seen to improve static stability, but decrease lift.

Membrane elasticity is included in the work of Murai and Maruyama [68], Jackson [69], and Sneyd [70], indicating a nonlinear C_L-α relationship as strains develop within the membrane at high incidence. Viscous flow models are employed in the work of Cyr and Newman [71] and Smith and Shyy [72]. The latter cites viscous effects as having much more influence on the aerodynamics of a sail wing than the effects of the assumptions made with linear thin airfoil theory. Specifically, inviscid solutions tend to over-predict lift at higher angles of attack (or large slack ratios), due to a loss of circulation caused by viscous effects about the trailing edge. A comparison of lift and tension versus angle of attack with experimental data (provided by Newman and Low [73], among others) yields mixed results; surprisingly, the lift is over-predicted by the viscous flow model, yet the tension is under-predicted.

Smith and Shyy also note a substantial discrepancy in the available experimental data in reported values of slack ratios, sail material properties, and Reynolds numbers, which may play a role in the mixed comparisons [74]. Comparison of numerical and experimental data for two-dimensional sails is also discussed by Lorillu et al. [75], who report satisfactory correlation for the flow structures and deformed membrane shape. Unsteady laminar-turbulent transitional

flows over a membrane wing are studied by Lian and Shyy [8] (who correlate the frequency spectrum of the vibrating membrane wing to the vortex shedding).

Three-Dimensional Wings

Three complicating factors can arise with the simulation of a three-dimensional membrane wing, rather than the planar case [76]. First, the tension is not constant (in space or direction), but is in a state of plane-stress. Secondly, the wing geometry can vary in the spanwise direction, and must be specified. Finally, the membrane may possess a certain degree of orthotropy [59]. Most importantly, analytical solutions cannot generally be found. Simplifying assumptions to this problem are given by Sneyd et al. [77] (triangular planform) and Ormiston [15] (rectangular sailwing). Sneyd et al. reduce both the aerodynamics and the membrane deformation to two-dimensional phenomena, where the third dimension is felt through a trailing edge cable.

Ormiston assumes both spanwise and chordwise deformation (but not aerodynamics), and is able to effectively decouple the two modules by using only the first term of a Fourier series to describe the inflated wing shape. Boudreault uses a higher-fidelity vortex lattice solver, but also prescribes the wing shape, here using cubic polynomials [78]. Holla et al. [79] use an iterative procedure to couple a double lattice method to a structural model, but assume admissible mode shapes to describe the deformation of a rectangular membrane clamped along the perimeter. The stress in the membrane is assumed to be always equal to the applied pre-stress (inextensibility, which overwhelms the nonlinearities in the membrane mechanics). A similar framework is used by Sugimoto in the study of circular membrane wings, where the wing shape is completely determined by a linear finite element solver [80].

Jackson and Christie couple a vortex lattice method to a nonlinear structural model for the simulation of a triangular membrane wing. Comparisons between a rigid wing, a membrane wing fixed at the trailing edge, and one with a free trailing edge elucidate the tradeoffs in lift

between adaptive camber and adaptive washout [76]. Charvet et al. [81] study the effect of non-homogenous incoming flow (vertical wind gradients and gusts) on a flexible sail. Schoop et al. use a nonlinear membrane stress-strain relationship (hyperelasticity) with a vortex lattice solver for simulation of a flat rectangular membrane wing [82].

Lian et al. [28] compute the unsteady aeroelasticity of a batten-reinforced membrane micro air vehicle wing, with a nonlinear hyperelastic solver and a turbulent viscous flow solver, using thin plate splines as an interfacing technique. Battens are simulated with a dense membrane. The results indicate self-exciting membrane vibration on the order of 100 Hz, with a maximum wing speed about 2% of the freestream, though overall aerodynamics are similar to that of a rigid wing prior to stall. Stanford and Ifju [14] discuss steady laminar aeroelasticity of a perimeter-reinforced membrane micro air vehicle wing, and are able to show the expected increase in lift and stability. Significant drag penalties are seen to arise with increasing Reynolds numbers, though the opposite is true for the rigid wing.

Complexities involving membrane wing models with both membranes and elastic shells (such as batten reinforcement) can be found in the work of Stanford et al. [83] (linear mechanics) and Ferguson et al. [84] (nonlinear). Higher-ordered membrane modeling with wrinkling (the loss of one or more principle stresses) as pertaining to membrane wings is given in the work of Smith and Shyy [85] and Heppel [86].

A large volume of work can be found dealing with experimental characterization of membrane wings. Early wind tunnel work by Fink [87] details a full-scale investigation of an 11.5 aspect ratio sail wing with a rigid leading edge, wingtip, and root, and a cabled trailing edge. The deformation is reported to be fairly smooth prior to stall, but visible rippling develops along the membrane at the onset of stall. At low angles of attack, the slope of the lift curve is

unusually steep (an instability discussed by Ormiston [15], among others), as the strains in the skin are low enough to allow for large changes in camber. Greenhalgh and Curtiss conduct wind tunnel testing to study the effect of planform on a membrane wing; only a parabolic planform is capable of sustaining flight loads without the aid of a trailing edge support member [88].

Galvao et al. [89] conduct tests on a membrane sheet stretched between two rigid posts, at Reynolds numbers between $3 \cdot 10^4$ and 10^5. The results show a monotonic increase in membrane camber with angle of attack and dynamic pressure, up to stall, as well as the aforementioned steep lift slopes. De-cambering of the wing as the pressure on the upper surface increases due to imminent flow separation is seen to ameliorate the stall behavior, as compared to a rigid plate.

Flow visualization of a batten-reinforced membrane MAV wing exhibits a weaker wing tip vortex system than rigid wings [13], possibly due to energy conservation requirements [90]. Parks measures the vortex core of a BR wing 5% to 15% higher above the wing than for the rigid case, though the flexible wing is seen to have a denser core-distribution of velocity for moderate angles of attack [91]. Gamble and Reeder [92] measure the flow structures resulting from interactions between propeller slipstream and a BR wing. The rigid wing spreads the axial component of the propwash further along the wing (resulting in a higher measured drag), whereas the membrane wing can absorb the downwash and upwash. A region of flow separation is measured at the root of the rigid wing, significantly larger and stronger than that measured from the membrane wing; the superiority decreases with larger Reynolds numbers.

Albertani et al. [9] detail loads measurements of both BR and PR wings, with dramatic improvements in longitudinal static stability of both membrane wings over their rigid counterpart. The BR wing has a noticeably smoother lift behavior in the stalled region, though neither deforms into a particularly optimal aerodynamic shape: both incur a drag penalty.

Deformation measurements of a membrane wing under propwash indicate unsymmetrical (about the root) wing shapes, a phenomenon which diminishes with higher angles of attack and dynamic pressures [47]. Stults et al. use laser vibrometry to measure the modal parameters (shapes, damping, frequency spectra) of a BR wing, which are then fed into a computational model for simulation of static and dynamic deformations in both steady freestream and a gust [93].

Aeroelastic Tailoring

Although aeroelastic tailoring is generally defined as the addition of directional stiffness into a wing structure so as to beneficially affect performance [11], this has traditionally meant the use of unbalanced composite plates/shells. Despite the use of such laminated materials on many MAV wing frames [94], there does not appear to be any tailoring studies on fixed micro air vehicle wings. Some investigators have applied the concept to the design of flapping ornithopter wings [95] [96], where a bend/twist coupling can vary the twist-induced incidence of a wing to improve thrust. Conventional tailoring studies can also be found applied to a larger class of unmanned aerial vehicles [97] [98]. The latter study by Weisshaar et al. uses laminate tailoring to improve the lateral control of a vehicle with an aspect ratio of 3. With ailerons, a wing tailored with adaptive wash-in is shown to improve roll performance and roll-reversal speed, though wash-out is preferred for a leading edge slat [98].

In addition to conventional laminate-based tailoring, drastic changes in the performance of a membrane wing are attainable by altering the pre-tension distribution within the extensible membrane. Holla et al. [79], Fink [87], Smith and Shyy [72], Murai and Maruyama [68], and Ormiston [15] all note the enormous impact that membrane pre-tension has on aerodynamics: for the two-dimensional case, higher pre-tension generally pushes flexible wing performance to that of a rigid wing. For a three-dimensional wing, the response can be considerably more complex, depending on the nature of the membrane reinforcement. Well-reported effects of increasing the

membrane pre-tension include: decrease in drag [89], decrease in $C_{L\alpha}$ [15], linearized lift behavior [72], increase in the zero-lift angle of attack [68], and more abrupt stalling patterns [89]. Ormiston details aeroelastic instabilities in terms of the ratio of spanwise to chordwise pre-tension [15].

Adequate control of membrane tension has long been known as a crucial concern to sailors in order to efficiently exploit wind power [99]. Tension-control is similarly important to the performance and agility of fighter kites: a wrinkled membrane surface will send the kite into an unstable spin. When pointed in the desired direction, pulling the control line tenses and deforms the kite, which thus attains forward velocity [100]. Biological inspiration for aerodynamic tailoring of membrane tension can be seen in the wing structures of pterosaurs and bats. In addition to membrane anisotropy (pterosaur wings have internal fibrous reinforcement to limit chordwise stretching [101], while bat wings skins are measured to be 100 times stiffer in the chordwise direction than the spanwise [102]), the tension can be controlled through a single digit (pterosaurs) [59], or varied throughout the wing via multiple digits (bats) [103].

Work formally implementing membrane tension as a variable for optimizing aerodynamic performance is very rare. Levin and Shyy [104] study a modified Clark-Y airfoil with a flexible membrane upper surface, subjected to a varying freestream velocity. Response surface techniques are used to maximize the power index averaged over a sinusoidal gust cycle, with membrane thickness variation, elastic modulus, and pre-stress used as variables. The maximum power index is found to coincide with the lower bound placed upon pre-stress, though lift and efficiency are also seen to be superior to a rigid wing.

Topology Optimization

The basics of topology optimization are given by Bendsøe and Sigmund [16] and Zuo et al. [105]: the design domain is discretized, and the relative density of each element can be 0 or 1.

Traditionally, this is done on a structure with static loads by minimizing the compliance under an equality constraint upon the volume fraction, though recent work can be seen in the design of compliant mechanisms [106] and channel flows [107] as well. Solving the problem with strictly discrete variables is rare; Beckers [108] uses a dual method to solve the large-scale discrete problem, while Deb and Goel [109] use a genetic algorithm. This latter option, though attractive, requires a very large number of function evaluations even for a small number of variables.

The topology optimization problem is typically solved using the SIMP approach (solid isotropic material with penalization): the density of each element is allowed to vary continuously between 0 and 1. A nonlinear power-law interpolation provides an implicit penalty which pushes the density to 0 or 1: intermediate densities are unfavorable, as their stiffness is small compared to their volume [16]. An adjoint sensitivity analysis of the discrete system is required to compute the sensitivity of the compliance (or other objective functions) with respect to each element density, as the number of variables is much larger than the number of constraints [110]. A mesh-independent filter upon the gradients is also typically employed, in order to limit the minimum size of the structure and eliminate checkerboards. Computation of the topological Pareto trade-off curve can be done using a multi-objective genetic algorithm [109], or by successively optimizing a weighted sum of conflicting objectives [111].

Aeronautical applications are given by Borrvall and Petersson [112], who divide a computational domain into either fluid or solid walls to find the minimum drag profile of submerged bodies in Stokes flows. Pingen et al. [107] solve a similar problem, using a lattice Boltzmann method as an approximation to the Navier-Stokes equations. Drag is minimized by a football shape (with front and back angles of 90°) at low Reynolds numbers (where reducing surface area is important), and a symmetric airfoil at higher Reynolds numbers (where

streamlining is more important).

Several examples can be found in the literature pertaining to compliance minimization of a flexible aircraft structure. Flight loads are typically obtained from an aerodynamics model, but the redistribution of these loads with wing deformation (aeroelasticity) is not included. Balabanov and Haftka [113] optimize the internal structure of a transport wing, using a ground structure approach (the domain is filled with interconnected trusses, and the cross-sectional area of each is a design variable [16]) for compliance minimization. Eschenauer and Olhoff [114] optimize the topology of an internal wing rib under both pull-up load maneuvers and internal tank pressures, using a bubble method. Krog et al. [115] also optimize the topology of wing box ribs, and discuss methods for interpretation of the results to form an engineering design, followed by sizing and shape optimization. Luo et al. [116] compute the optimal topology of an entire aerodynamic missile body, considering both static loads and natural frequencies.

Santer and Pellegrino [117] replace the leading edge of a wing section with a compliant morphing mechanism, which is subjected to topology optimization. Rather than a compliance-based objective function, the author's use airfoil efficiency, but as above, do not include aeroelastic load redistribution. Such an aeroelastic topology optimization is an under-served area in the literature. Maute and Allen [118] consider the topological layout of stiffeners within a swept wing, using a three-dimensional Euler solver coupled to a linear finite element model. Results from an adjoint sensitivity analysis of the three-field couple aeroelastic system [110] [119] are fed into an augmented Lagrangian optimizer to minimize mass with constraints upon the lift, drag, and wing displacement. The authors are able to demonstrate the superiority of designs computed with aeroelastic topology optimization, rather than considering a constant pressure distribution.

Gomes and Suleman [120] use a spectral level set method to maximize aileron reversal speed by reinforcing the upper skin of a wing torsion box via topology optimization. Maute and Reich [106] optimize the topology of a compliant morphing mechanism within an airfoil, by considering both passive and active shape deformations. The authors are able to locate superior optima with this aeroelastic topology optimization approach, as compared to a jig-shape approach: optimizing the aerodynamic shape, and then locating the mechanism that leads to such a shape.

At present, there is no research pertaining to aeroelastic topology optimization of membrane wings, or micro air vehicle wings. Biological inspiration for this concept can be found in the venation of insect wings however. For example, a pleated grid-like venation can be seen in dragonfly wings, posteriorly curved veins in fly wings, and a fan-like distribution of veins in the locust hindwing [121]. On the whole, the significance of this variation in wing stiffness distribution between species is not well understood.

CHAPTER 3
EXPERIMENTAL CHARACTERIZATION

As will be extensively discussed below, numerical modeling of flexible MAV wings, while conducive to optimization studies, is very challenging: at the present time, no model exists which can accurately predict all of the unsteady flow phenomenon known to occur over a micro air vehicle. As such, experimental model validation is required to instill confidence in the employed models, highlight numerical shortcomings, and provide additional aeroelastic wing characterization. All of the aerodynamic characterization experiments discussed in this work are run in a closed-loop wind tunnel, a diagram of which can be seen in Figure 3-1. Only longitudinal aerodynamics are of interest, and only α-sweep capability is built into the test setup.

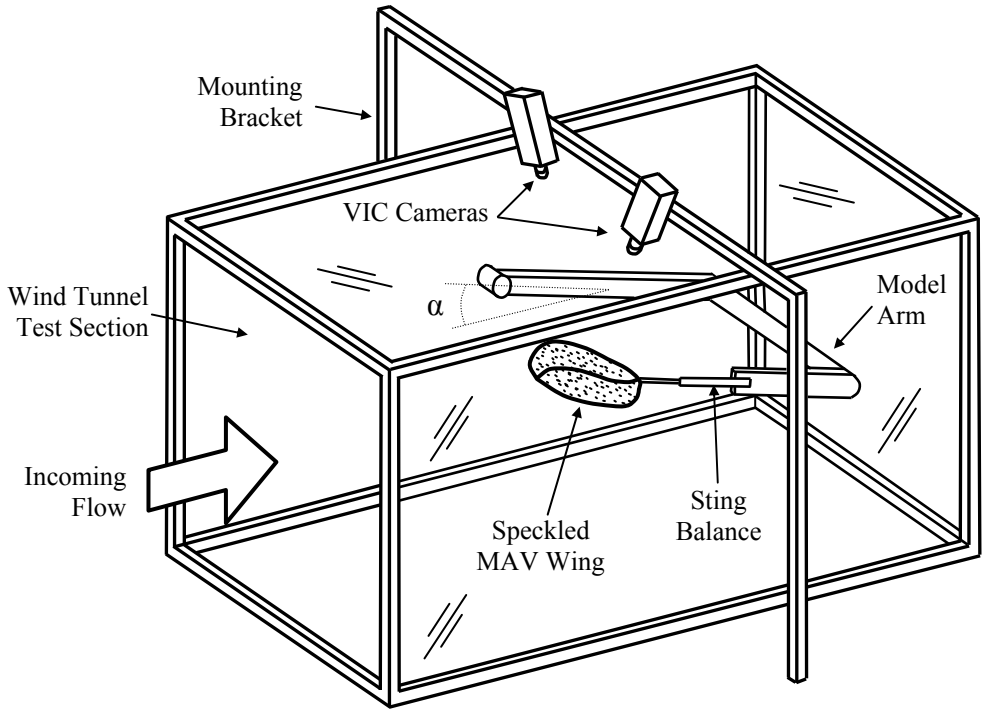

Figure 3-1. Schematic of the wind tunnel test setup.

Closed Loop Wind Tunnel

The test facility used for this work is an Engineering Laboratory Design, Inc. (ELD) 407B closed-loop wind tunnel, with the flow loop arranged in a horizontal configuration. The test

section has an inner dimension of 0.84 m on each side and is 2.44 m deep. The velocity range is between 2 and 45 m/s, and the maximum Reynolds number is 2.7 million. The flow is driven via a two-stage axial fan with an electric motor powered by three-phase 440 V at 60 Hz. The controller is operated remotely with appropriately dedicated data acquisition software, wherein the driving frequency is based upon a linear scaling of an analog voltage input. Suitable flow conditions are achieved through hexagonal aluminum honeycomb cell, high-porosity stainless steel screens, and turning vane cascades within the elbows of the closed loop. Centerline turbulence levels are measured on the order of 0.2%. Optical glass window access is available on the sidewalls and the ceiling.

A Heise model PM differential pressure transducer rated at 12.7 cm and 127 cm of water (with a manufacturer-specified ± 0.002% sensitivity and a ± 0.01% repeatability) is used to measure the pressure difference from a pitot-static tube mounted within the test section, whose stagnation point is located at the center of the section's entrance. The Heise system is capable of measuring wind speeds up to 45 m/s. A four-wire resistance temperature detector is mounted to the wall of the test section for airflow temperature measurements.

Strain Gage Sting Balance

Several outstanding issues exist with measuring the aerodynamic loads from low Reynolds number flyers. Several such airfoils are known to exhibit hysteresis loops at high angles of attack. If the flow does not reattach to the wing surface (typically for lower Reynolds numbers below $5 \cdot 10^4$ [17]) counterclockwise hysteresis loops in the lift data may be evident; the opposite is true if a separation bubble exists via reattachment [24]. Adequate knowledge of such a loop is obviously important as it effects vehicle control problems via stall and spin recovery. As described by Marchman [122], the size of the hysteresis loop measured in a wind tunnel can be incorrectly decreased by poor flow quality: large freestream turbulence intensity levels or

acoustic disturbances (noise emitted from the turbulent boundary layer along the tunnel walls, the wind tunnel fan, etc. [24]). Mounting techniques are also presumed to cause an incorrect relationship between Reynolds number and the zero-lift angle of attack among several sets of published data [122].

Sensitivity is another concern, particularly in drag force measurements which may be as low as 0.025 N (computed for a wing with a chord of 100 mm and a Reynolds number of $5 \cdot 10^4$). An electrical resistance strain gage sting balance is typically used for force and moment measurements. While strain gages typically provide the greatest sensitivity and simplicity, they are also prone to temperature drift, electromagnetic interference, creep, and hysteresis.

An internal Aerolab 01-15 6-component strain gage sting balance is used for force/moment measurements in the current work. Wind tunnel models are mounted to the sting balance by a simple jaw mechanism. Each of the six channels is in a full Wheatstone-bridge configuration, with five channels dedicated to forces, and one to a moment. Two forces are coincident with the vertical plane of the model (traveled during an α-sweep), two are in the plane normal to the previous (traveled during a β-sweep), one force is in the axial direction, and the moment is dedicated to roll. Data acquisition is done with a NI SCXI 1520 8 channel programmable strain gage module with full bridge configuration, 2.5 excitation volts, and a gain of 1000.

Other modules included in the system are a SCXI 1121 signal conditioner, 1180 feed-through with 1302 breakout and 1124 D/A module. A NI 6052 DAQPad firewire provides A/D conversion, multiplexing, and the PC connection. For a given flight condition, the output signals from the six components are sampled at 1000 Hz for 2 seconds. The average of this data is sent to one module for calculation of the relevant aerodynamic coefficients, and the standard deviation of the data is stored for further uncertainty analysis. Signals from each channel are

recorded before and after a testing sequence, with no airflow through the tunnel, to provide an estimation of the overall drift.

The sting balance is mounted to a custom-fabricated aluminum model arm within the wind tunnel (seen in Figure 3-1). A U-shape is built into the arm, so that the structure curves well behind the model and aerodynamic interactions are minimal. The arm extends through a hole in the wall of the test section, and is then attached to a gearbox and a brushless servomotor for pitching control. The motor is run by a single axis motion controller; a high precision US Digital absolute encoder, connected to an SCXI 1121 module provides angle of attack feedback. Pitching rates are on the order of 1 °/s. For a given flight condition, the aforementioned instrumentation (the Heise and thermocouple connected through an RS232, and the sting balance) is used to measure the pressure, temperature, and voltage signals. A set of tare voltages (obtained prior to the test, with no flow through the tunnel) are subtracted from the sting balance data, which is then filtered through the calibration matrix, and normalized by the subsequent computations of flow velocity and air density. The numerous systems described above are integrated to allow for completely automated wind tunnel testing for force/moment data, along with a LABview GUI written for user inputs of the wing geometry, angle of attack array, and the commanded wind speed.

Standard procedures [123] are used to calibrate the sting balance down to an adequate sensitivity: 0.01N in drag (though still just 40% of the minimum given above). Such a resolution is comparable to that found in the work of Pelletier and Mueller [34], but superior precision is used by Kochersberger and Abe [124] and Moschetta and Thipyopas [125]. The calibration matrix is determined through the use of known weights applied at control points in specified directions. This calibration is able to predict the relationship between load and signal for a given

channel, as well as potential interactions (second-order interactions are not included) in both single and multiple load configurations. Further information on the calibration of strain gage sting balances for micro air vehicle measurements is given by Mueller [126] and Albertani [47].

Uncertainty Quantification

Two types of uncertainty are thought to contribute to the eventual error bounds of the sting balance data. The resolution error is indicative of a measurement device's resolution limit: for example, the inclinometer used to measure the pitch of a model can measure angles no finer than 0.1°, an uncertainty that can be propagated through the equations to find its theoretical effect on the aerodynamic coefficients using the Kline-McClintock technique [127]. The following resolution errors are used: 3 Pa of dynamic pressure from the Heise, $1.2 \cdot 10^{-7}$ V from the output voltage of the strain gages (estimated from the quantization error of the 16-bit DAQ cards), 0.001 m^2 from wing area measurements, and 0.002 m from chord length measurements. The second source is the precision error, a measure of the repeatability of a measurement. This is well quantified by the standard deviation of the voltage signals from 2000 samples at each angle of attack, as described above. Uncertainty bounds are computed with a squared sum of the resolution and precision errors (where the latter is magnified by Student's t at 95% confidence and infinite degrees of freedom). The precision of the strain gage signals is found to contribute the most error to the aerodynamic coefficients, particularly in the stalled regions. Typical uncertainty percentages are 5% for C_L, 7% for C_D, 9% for L/D, and 20% for C_m. Theses values can be expected to double during stall.

Wind Tunnel Corrections

Corrections are applied to the coefficients of lift, drag, and pitching moment based upon wind tunnel blockage, and model flexibility effects. The solid blockage effect is due to the presence of the model within the wind tunnel, thus decreasing the effective area of the test

section and increasing the flow velocity (and the coefficients) in the vicinity of the model [128]. Wake blockage occurs when the flow outside of the model's wake must increase, in order to satisfy the flow continuity in a closed tunnel. In an open freestream, the velocity outside of the wake would be equal to the freestream velocity. The effect of wake blockage is proportional to the wake size, and therefore proportional to drag [3]. Streamline curvature blockages are the effect of the tunnel walls on the streamlines around the model. The streamlines are compressed, increasing the effective camber and lift [129]. Such corrections generally decrease both lift and drag, while the pitching moment is made less negative, with percentage changes on the order of 2-3%.

Finally, flexibility effects within the wind tunnel setup must be accounted for. These effects are primarily caused by the elasticity of the internal strain gage sting balance; under load the wind tunnel model will pitch up via a rigid body rotation. Visual image correlation (described below) is used to measure the displacement at points along the wing known to be nominally rigid (specifically, the sting balance attachment points along the wing root). This data then facilitates the necessary transformations and translations of the wing surface, and is used to correct for the angle of attack. $\Delta\alpha$ is a positive monotonically increasing function of both lift and dynamic pressure, and can be as large as 0.7º at high angles of attack [47].

Visual Image Correlation

Wind tunnel model deformation measurements are a crucial experimental tool towards understanding the role of structural composition upon aerodynamic performance of a MAV wing. The flexible membrane skin generally limits applications to non-contacting optical methods, several of which have been reported in the literature. Galvao et al. [89] use stereo photogrammetry for displacement measurements of a membrane wing, with a reported resolution between 35 and 40 μm. Data is available at discrete markers placed along the wing. Projection

moiré interferometry requires no such marker placement (a fringe pattern is projected onto the wing surface), and the resulting data set is full-field. However, displacement resolutions reported by Fleming et al. [130] are relatively poor (250 μm), the dual-camera system must be rotated during the α-sweep, and only out-of-plane data is available, making strain calculations (if needed) impossible. Burner et al. [131] discuss the use of photogrammetry, projection moiré interferometry, and the commercially available Optotrak^{TM} system. The authors find no single technique suitable for all situations, and that a cost-benefit tradeoff study may be required. Furthermore, the methods need not be mutually exclusive, as situations may arise wherein they can be used in combination. For the current work, a visual image correlation system (VIC), originally developed by researchers at the University of South Carolina [132], is used to measure wing geometry, displacements, and plane strains.

The underlying principle of VIC is to calculate the displacement field by tracking the deformation of a subset of a random speckle pattern applied to the specimen surface. The random pattern is digitally acquired by two cameras before and after loading. The acquisition of images is based on a stereo-triangulation technique, as well as the computing of the intersection of two optical rays: the stereo-correlation matches the two 2-D frames taken simultaneously by the two cameras to reconstruct the 3-D geometry. The calibration of the two cameras (to account for lenses distortion and determine pixel spacing in the model coordinates) is the initial fundamental step, which permits the determination of the corresponding image locations from views in the different cameras. Calibration is done by taking images (with both cameras) of a known fixed grid of black and white dots.

Temporal matching is then used: the VIC system tries to find the region (in the image of the deformed specimen) that maximizes a normalized cross-correlation function corresponding to

a small subset of the reference image (taken when no load is applied to the structure) [132]. The image space is iteratively swept by the parameters of the cross-correlation function, to transform the coordinates from the original reference frame to coordinates within the deformed image. An originally square subset in the un-deformed image can then be mapped to a subset in the deformed image. As it is unlikely that the deformed coordinates will directly fall onto the sampling grid of the image, accurate grey-value interpolation schemes [133] are implemented to achieve optimal sub-pixel accuracy without bias. This procedure is repeated for a large number of subsets to obtain full-field data.

In order to capture the three-dimensional features and deformation of a wind tunnel model, twin synchronized cameras, each looking from a different viewing angle, are installed above the wind tunnel ceiling, as can be seen in Figure 3-1. As the cameras must remain stationary through the experiment (to preserve the information garnered from the calibration procedure), a mounting bracket is constructed to straddle the tunnel, and prevent the transmission of vibration. Optical access into the test section is through an optical glass ceiling. The results of conducting visual image correlation tests with a glass interface between the cameras and the specimen have been studied, with little benign effects reported [134]. Furthermore, the cameras are initially calibrated through the window to ensure minimal distortion. Two 250 W lamps illuminate the model, enabling the use of exposure times of 5 to 10 ms.

The twin cameras are connected with a PC via an IEEE 1394 firewire cable, and a specialized unit is used to synchronize the camera triggers for instantaneous shots. A standard acquisition board installed in the computer carries out the digitalization of the images, and the image processing is carried out by custom software, provided by Correlated Solutions, Inc. Typical data results that can be obtained from the VIC system consist of the geometry of the

surface in discrete x, y, and z coordinates (where the origin is located at the centroid of the speckled area of interest, and the outward normal points towards the cameras, by default), and the corresponding displacements along the wing (u, v, and w). The VIC system places a grid point every N pixels, where N is user defined. A final post-processing option involves calculating the in-plane strains (ε_{xx}, ε_{yy}, and ε_{xy}). This is done my mapping the displacement field onto an unstructured triangular mesh, and conducting the appropriate numerical differentiation (the complete definition of finite strains is used).

Data Procession

The objective of most of the wind tunnel tests given in the remainder of this work is to determine the deformation of the wings under steady aerodynamic loads, at different angles of attack and free stream velocities, while simultaneously acquiring aerodynamic force data. Each angle of attack requires a separate wind-off reference image: failure to do so will inject rigid body motions (as the body moves sequentially from one angle of attack to the next) into the displacement fields. If each reference image taken for VIC is of the fully assembled wing, the amount of pre-strain in the wing is not included in the measured strain field, but only those caused by the aerodynamic loads. This condition needs to be carefully considered in the evaluation of the results, since the areas of relaxation of the pre-existing tension will generate areas of "virtual" compression within the skin. The thin membrane cannot support a genuine compressive stress (it will wrinkle), but negative Poisson strains are possible.

An alternative procedure uses the un-stretched sheet of latex rubber (prior to adhesion on the wing) as a reference image. This provides the state of pre-strain in the membrane, as well as the absolute strain field during wind tunnel testing, but makes the displacement fields very difficult to interpret and is not used here. The pre-strain data is merely recorded (with a separate set of reference and deformed images), but not used as a reference for further aerodynamic

testing. As mentioned above, the acquired displacement field will be composed of both elastic wing deformation and rigid body motion/translations originating from the sting balance, the latter of which must be filtered out. The computed strains are unaffected by these motions.

Uncertainty Quantification

In order to estimate the resolution error of the VIC system, a simple ad hoc experiment is conducted. A known displacement field is applied to a structure, and then compared with the field experimentally determined by way of image correlation. A thin latex membrane is stretched and fixed to a rigid aluminum ring with a diameter of 100 mm. The center of the membrane circle is then indented with a rigid steel bar with a spherical head of 8 mm diameter. The bar is moved against the membrane by a micrometer with minimum increments of 0.25 mm. Results, in terms of the error between commanded displacement (via the micrometer) and the measured displacement at the apex of the membrane profile, directly beneath the axis of the indentation bar, are given in Figure 3-2.

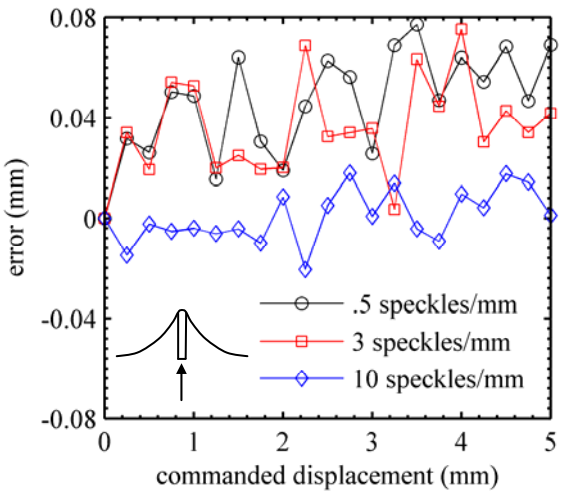

Figure 3-2. Quantification of the resolution error in the VIC system.

Three different VIC setups are shown: 0.5, 3, and 10 speckles per millimeter of membrane, the latter of which corresponds to 2 pixels per speckle (with half the membrane in view). As

expected, the error is smallest for the finest speckle pattern, whose readings randomly oscillate about zero, with a peak error of 0.018 mm (0.6%). The coarser speckling patterns randomly oscillate at an offset error of 0.04 mm, with a peak error of 0.077 mm (2.2%). This places the resolution error for the VIC system between 10 and 20 μm, about twice the resolution reported for the photogrammetry system [89]. Though not explicitly discussed here, the strain resolution is estimated to be between 500 and 1000 με (a non-dimensional parameter independent of speckle size), a high value (compared to strain gages, for example) owing to the differentiation methods used.

Model Fabrication and Preparation

Only the wing (152 mm wingspan, 124 mm root chord, 1.25 aspect ratio) of the MAVs seen in Figure 1-1 and Figure 1-2 is considered in this work. The camber at the root is 6.8% (at x/c = 0.22), the reflex at the root is -1.4% (at x/c = 0.86), and 7º of positive geometric twist (nose up) is built into the wingtip. The MAV wing has 7º of dihedral between 2y/b = 0.4 and the wingtip. The fuselage, stabilizers, and propeller are omitted from both computations and experiments. The leading edge, inboard portion of the wing, and perimeter (of the PR wings) are constructed from a bi-directional plain weave carbon fiber laminate with 3000 fibers/tow, pre-impregnated with thermoset epoxy. The battens (for the BR wings) are built from uni-directional strips of carbon fiber. These materials are placed upon a tooling board (appropriately milled via CNC) and cured in a convection oven at 260º F for four hours. A wind tunnel attachment (to be fastened to the aforementioned jaw mechanism) is bonded along the root of the wing between x/c = 0.25 and 0.8.

The latex rubber skin adhered to this wing surface is 0.12 mm thick, and approximately isotropic. A random speckle pattern is applied to the latex sheet with flat black spray paint, and then coated with a layer of dulling spray. Each paint speckle, while relatively brittle, has a small

average diameter (less than 0.5 mm) and is generally not connected to another speckle pattern; the pattern should not provide significant reinforcement to the latex. If information concerning the state of pre-strain in the skin is desired, a picture of the un-stretched latex sheet is taken for future use as a reference in the VIC system. The latex is then appropriately stretched about a frame (or not at all if a slack membrane is desired), and adhered to the upper carbon fiber wing surface (which must be painted white) with spray glue. After the glue has dried, the excess latex is trimmed away. A picture of the resultant wind tunnel model is given in Figure 3-3.

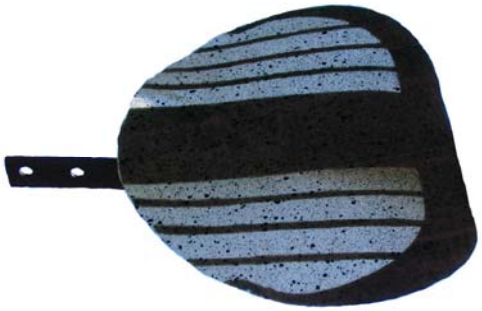

Figure 3-3. Speckled batten-reinforced membrane wing with wind tunnel attachment.

CHAPTER 4
COMPUTATIONAL FRAMEWORK AND VALIDATION

Several difficulties are associated with modeling the passive shape adaptation of a flexible micro air vehicle wing. From a fluid dynamics standpoint, the low aspect ratio wing (1.25) forces a highly three-dimensional flow field, and the low Reynolds number (10^5) implies strong viscous effects such as flow separation, transition, and potential reattachment. Structurally, the mechanics of the rubber membrane inflation are inherently nonlinear, and the orthotropy of the thin laminated shells used for the wing skeleton is dependent on the plain weave fiber orientation. Further difficulties arise with the inclusion of pre-tension within the membrane.

Only static aeroelasticity is considered here. Several computational membrane wing studies have included unsteady effects [28] [81], and are thus able to study phenomena such as vortex shedding [18], membrane vibration (unstable [62] or otherwise), unsteady interactions between the separated flow and the tip vortices [6], and wind gusts [8]. Past wind tunnel work, however, has indicated that MAV membrane inflation is essentially qausi-static for a large range of angles of attack up to stall [135], and that adequate predictive capability still exists for those flight conditions with obvious unsteady features [43].

Structural Solvers

The unstructured mesh used for finite element analysis can be seen in Figure 4-1. 2146 nodes are used to describe the surface of the semi-wing, connected by 4158 three-node triangle elements. The same mesh is used for both batten and perimeter-reinforced computations, by using different element-identification techniques, as seen in the figure. Greater local effects are expected in the membrane areas of the wing, and the mesh density is altered accordingly. Nodes that lie along the wing root between x/c = 0.25 and 0.8 are given zero displacement/rotation boundary conditions, to emulate the restrictive effect of the wind tunnel attachment (Figure 3-3).

All nodes that lie on the wing root are constrained appropriately as necessitated by wing symmetry.

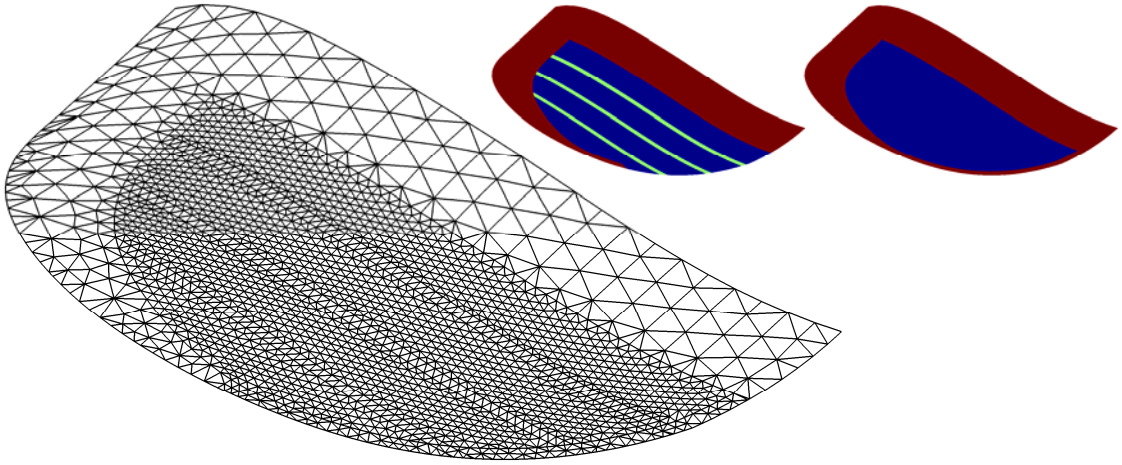

Figure 4-1. Unstructured triangular mesh used for finite element analysis, with different element types used for PR and BR wings.

Composite Laminated Shells

Discrete Kirchhoff triangle plate elements [136] are use to model the bending/twisting behavior of the carbon fiber areas of the wings: leading edge, root, perimeter, and battens. Due to the comparative stiffness of these materials, linear behavior is assumed. The orthotropy of the plates is introduced by the flexural stiffness matrix of the laminates, $\mathbf{D}_p$, relating three moments (two bending, one twisting) to three curvatures:

$$\mathbf{D}_p = \sum_{k=1}^{NL} \mathbf{Q}_k \cdot \left(h_k^3 / 12 + h_k \cdot z_k^2 \right) \tag{4-1}$$

where NL is the number of layers in the laminate, h_k is the thickness of the k^{th} ply, z_k is the normal distance from the mid-surface of the laminate to the mid-surface of the k^{th} ply, and $\mathbf{Q}_k$ is the reduced constituitive matrix of each ply, expressed in global coordinates. $\mathbf{Q}_k$ depends upon the elastic moduli in the 1 and 2 directions (equal for the bi-directional laminate, but not so for the uni-directional) E_1 and E_2, the Poisson's ratio ν_{12}, and the shear modulus G_{12}. The finite element stiffness matrix pertaining to bending/twisting is then found to be:

$$\mathbf{K}_p = \mathbf{T} \cdot \int_{A_o} \mathbf{B}_p^T \cdot \mathbf{D}_p \cdot \mathbf{B}_p \cdot dA \cdot \mathbf{T}^T \tag{4-2}$$

where **T** is a matrix which transforms each element from a local coordinate system to a global system, $\mathbf{B}_p$ is the appropriate strain-displacement matrix [137], and A_o is the un-deformed area of the triangular element. $\mathbf{K}_p$ is a 9x9 matrix whose components reflect the out-of-plane displacement w and two in-plane rotations at the three nodes.

Similarly, in-plane stretching of the laminates (a secondary concern, but necessarily included), is given by:

$$\mathbf{A}_p = \sum_{k=1}^{NL} \mathbf{Q}_k \cdot h_k \tag{4-3}$$

where $\mathbf{A}_p$ is a laminate matrix relating three in-plane stress resultants to three strains. Expressions similar to Eq. (4-2) are then formulated to compute $\mathbf{K}_m$, the 6x6 finite element stiffness matrix governing in-plane displacements u and v at the three nodes. $\mathbf{K}_m$ and $\mathbf{K}_p$ are then combined to form the complete 15x15 shell stiffness matrix of each element, $\mathbf{K}_e$. Drilling degrees of freedom are not included. Though some wing designs may use un-symmetric laminates, coupling between in-plane and out-of-plane motions is not included.

Loads Model Validation/Estimation. The following method is used to both validate the model presented above, and identify the relevant material properties of the laminates. A series of weights are hung from a batten-reinforced wing (with 2 layers of bi-directional carbon fiber oriented 45º to the chord line and 1 layer uni-directional battens, but no membrane skin) at nine locations: the two wing tips, the trailing edges of the six battens, and the leading edge, as shown in Figure 4-2. VIC is used to measure the resulting wing displacements. A linear curve is fit through the load-displacement data of all nine points due to all nine loadings. The slopes of these curves are used to populate the influence matrix in Table 4-1: the diagonal gives the motion

of a wing location due to a force at that location; the off-diagonals represent indirect relationships.

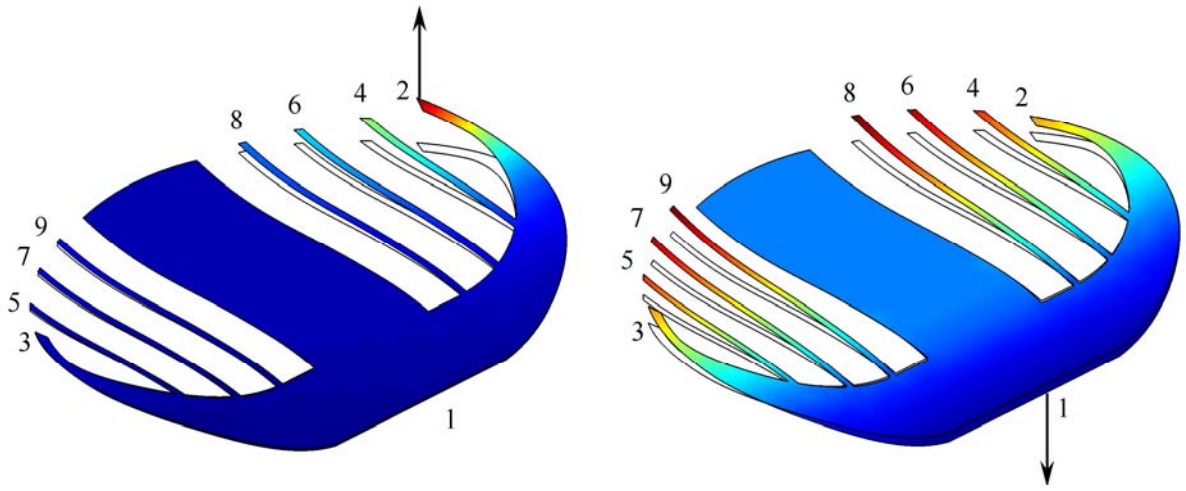

Figure 4-2. Computed deformations of a BR wing skeleton due to a point load at the wing tip (left) and the leading edge (right).

A genetic algorithm is then used for system identification. The six variables are the material parameters: E_1, ν_{12}, and G_{12} of both the plain weave and the battens. E_2 is assumed to be equal to E_1 for the plain weave, and equal to 10 MPa for the uni-directional battens. This latter value has little bearing on the results, as the 1 direction corresponds with the axis of the batten. The objective function is the sum of the squared error between the diagonals of the computed and the measured influence matrix. The error terms are appropriately normalized before summation and off-diagonal components are not considered in the optimization. For the genetic algorithm, the population size is 20, the elitism count is 2, reproduction is via a two-point crossover function with a 0.8 crossover fraction, and a uniform mutation function is used with a 0.01 mutation rate. Convergence is adequately achieved after 30 iterations, with each function evaluation call requiring a single finite element analysis.

The resulting numerical influence matrix is given in Table 4-2. This matrix is symmetric, whereas the experimental matrix is slightly un-symmetric, probably due to manufacturing errors.

For the plain weave, E_1 = 34.8 GPa, ν_{12} = 0.41, and G_{12} = 2.34 GPa. For the uni-directional battens, E_1 = 317.2 GPa, ν_{12} = 0.31, and G_{12} = 1.05 GPa. The model correctly predicts the very stiff leading edge (point 1), and the negative influence it has on the remainder of the wing (as shown on the right of Figure 4-2). The rest of the points along the wing positively influence one another. Errors between the two matrices are typically on the order of ± 5-10%; the numerical wing is generally stiffer than the actual wing. As expected, the weakest battens are the longest, found towards the root (points 8 and 9). The wingtips (points 2 and 3) generally have the greatest indirect influence on the rest of the wing (as shown on the left of Figure 4-2).

Force-displacement trends at the nine locations along the wing, due to loads at those points (the diagonal terms in the matrices) are given in Figure 4-3, showing a suitable match between model and experiment. With the exception of the leading edge, two data points are given for each load level, corresponding to the data from the left and right sides of the wing. Higher fidelity methods for system identification of a carbon fiber MAV skeleton are given by Reaves et al. [138], who utilize model update techniques with uncertainty quantification methods. This is largely done due to the uncertainty in the laminate lay-up, predominately in ply overlapping regions within the skeleton, which is not an issue for the current work.

Table 4-1. Experimental influence matrix (mm/N) at points labeled in Figure 4-2.

	1	2	3	4	5	6	7	8	9
1	1.58	-2.90	-2.97	-3.00	-3.07	-3.47	-3.54	-3.05	-3.03
2	-2.93	104.65	3.94	50.85	5.88	36.47	7.65	26.06	9.99
3	-3.07	3.67	118.46	8.18	52.24	9.39	38.29	13.33	29.22
4	-3.68	49.05	5.69	329.11	8.71	44.14	10.51	33.05	13.23
5	-3.78	5.68	50.15	9.17	366.92	11.89	45.19	14.98	33.68
6	-4.33	36.41	7.92	44.63	10.68	547.50	13.41	38.46	15.23
7	-4.37	7.77	36.74	11.46	44.35	13.28	513.83	17.40	38.19
8	-4.75	24.30	9.02	30.15	11.24	34.68	12.63	757.00	15.81
9	-4.76	9.22	25.09	12.34	30.30	14.32	35.51	17.65	742.25

Table 4-2. Numerical influence matrix (mm/N) at points labeled in Figure 4-2.

	1	2	3	4	5	6	7	8	9
1	1.49	-2.92	-2.92	-3.61	-3.61	-4.24	-4.24	-4.60	-4.60
2	-2.92	107.96	3.36	54.49	5.05	33.10	6.80	20.84	8.13
3	-2.92	3.36	107.96	5.05	54.49	6.80	33.10	8.13	20.84
4	-3.61	54.49	5.05	312.00	6.78	39.30	8.51	25.09	9.73
5	-3.61	5.05	54.49	6.78	312.00	8.51	39.30	9.73	25.09
6	-4.24	33.10	6.80	39.30	8.51	584.26	10.14	28.81	11.18
7	-4.24	6.80	33.10	8.51	39.30	10.14	584.26	11.18	28.81
8	-4.60	20.84	8.13	25.09	9.73	28.81	11.18	776.48	11.95
9	-4.60	8.13	20.84	9.73	25.09	11.18	28.81	11.95	776.48

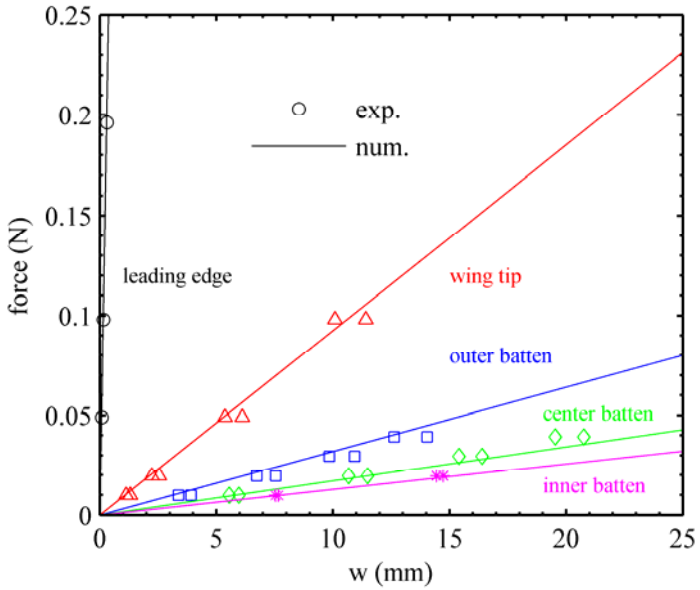

Figure 4-3. Compliance at various locations along the wing, due to a point load at those locations.

Membrane Modeling

In the modeling of thin, elastic membranes (with no resistance to a bending couple), three basic options are available. If there exists a significant pre-strain field throughout the sheet, linear modeling is possible by assuming inextensibility: the pre-strain overwhelms the strains that develop as a result external loading. As these strains grow in magnitude (or if the membrane is originally slack) a nonlinear model must be used, as the membrane's resistance depends upon the loading (geometric nonlinearity). However, a linear constituitive relationship is still typically

valid up to a point, after which the membrane becomes hyperelastic (material nonlinearity), and the stress-strain relationship changes with increasing load.

Linear Modeling. Geometric stress stiffening provides a relationship between in-plane forces and transverse deflection [137], and is indicative of a structure's reluctance to change its state of stress. For an initially flat membrane with a transverse pressure, the constitutive equation is:

$$N_x \cdot w_{,xx} + 2 \cdot N_{xy} \cdot w_{,xy} + N_y \cdot w_{,yy} + p = 0 \tag{4-4}$$

where w is the out-of-plane displacement (as above), N_x, N_{xy}, and N_y are the in-plane pre-stress resultants, and p is the applied pressure field. For an isotropic stress field with no shear, this equation reduces to the well known Poisson's equation [139]. This model assumes that the displacement along the membrane is purely out-of-plane; thus the membrane is inextensible in response to a pressure field (although extensibility is needed to apply the initial pre-stress field).

The resulting finite element model is fairly inexpensive, as each node has only one degree of freedom, and standard direct linear solvers can be used. This model is thought to be accurate for small pressures, small displacements, and large pre-stresses. Though it is not expected that the MAV wing displacements will be particularly large (typically less than 10% of the root chord), it is expected that a slack membrane skin may provide many aerodynamic advantages. As the solution to Eq. (4-4) becomes unbounded as the pre-stress approaches zero, higher fidelity models will also be pursued for the current work. MAV wing simulations with linear membrane models can be found in the work of Stanford and Ifju [14], Thwaites [65], and Sugimoto [80].

Nonlinear Modeling. The nonlinear membrane modeling discussed in this section will incorporate geometric nonlinearities, but Hooke's law is assumed to still be valid. For the inflation of a circular membrane, Pujara and Lardner [140] show that linear and hyperelastic

constituitive relationships provide the same numerical solutions up to deformations on the order of 30% of the radius, a figure well above the deflections expected on a membrane wing. Geometric nonlinearity implies that the deformation is large enough to warrant finite strains, and that the direction of the non-conservative pressure loads significantly changes with deformation. Eq. (4-4) is still valid, only now the stress resultants depend upon the state of pre-stress, as well as in-plane stretching, which in turn depends on the out-of-plane displacement. Furthermore, the rotation of the membrane is no longer well-approximated by the derivative of w, rendering the equilibrium equation nonlinear. Three displacement degrees of freedom are required per node (u, v, w), rather than the single w used above. Finite element implementation of such a model is described by Small and Nix [141] and Pauletti et al. [142].

The strain pseudo-vector within each element is given as:

$$\boldsymbol{\varepsilon} = \boldsymbol{\varepsilon}_o + \boldsymbol{\varepsilon}_L = \mathbf{B}_o \cdot \mathbf{X}_e + \mathbf{B}_L \cdot \mathbf{X}_e \tag{4-5}$$

where $\boldsymbol{\varepsilon}_o$ and $\boldsymbol{\varepsilon}_L$ represent the division of the linear (infinitesimal) and nonlinear contributions to the Green-Lagrange strain, $\mathbf{X}_e$ is a vector of the degrees of freedom in the elements (three displacements at the three nodes), and $\mathbf{B}_o$ and $\mathbf{B}_L$ are the appropriate strain-displacement matrices (the latter of which depends upon the nodal displacements) [143]. The pre-stress (if any) can be included into the model in one of two methods. First, they can be simply added to the stresses computed my multiplying the strain vector of Eq. (4-5) through the constituitive matrix. This may cause problems if the imposed pre-stress distribution does not exactly satisfy equilibrium conditions, or if there is excessive curvature in the membrane skin: the membrane will deform, even in the absence of an external force.

A second option is to use the pre-stresses in a finite element implementation of Eq. (4-4), then add the resulting stiffness matrix and force vectors to the nonlinear terms. For a flat

membrane with uniform pre-stress, the two methods are identical. The internal force in each element $\mathbf{P}_e$ can be computed from the principle of virtual work:

$$\mathbf{P}_e = \mathbf{T} \cdot \int_{V_o} \left[\mathbf{B}_o + \partial \left(\mathbf{B}_L \cdot \mathbf{X}_e \right) / \partial \mathbf{X}_e \right]^T \cdot \mathbf{A}_m \cdot \boldsymbol{\varepsilon} \cdot dV + \mathbf{T} \cdot \mathbf{K}_w \cdot \mathbf{X}_e \tag{4-6}$$

where $\mathbf{A}_m$ is the linear constitutive elastic matrix of the membrane, $\mathbf{A}_m \cdot \boldsymbol{\varepsilon}$ is the stress pseudo-vector within each element, and $\mathbf{K}_w$ is the stiffness matrix representation of Eq. (4-4), containing only terms related to the out-of-plane displacement w. The tangential stiffness matrix $\mathbf{K}_e$ is then the sum of the geometric $\mathbf{K}_\sigma$, constituitive $\mathbf{K}_c$, external $\mathbf{K}_{ext}$ and pre-stress stiffness matrix $\mathbf{K}_w$:

$$\mathbf{K}_\sigma = \mathbf{T} \cdot \int_{V_o} \mathbf{G}^T \cdot \mathbf{M} \cdot \mathbf{G} \cdot dV \cdot \mathbf{T}^T \tag{4-7}$$

$$\mathbf{K}_c = \mathbf{T} \cdot \int_{V_o} \left[\mathbf{B}_o + \partial \left(\mathbf{B}_L \cdot \mathbf{X}_e \right) / \partial \mathbf{X}_e \right]^T \cdot \mathbf{A}_m \cdot \left[\mathbf{B}_o + \partial \left(\mathbf{B}_L \cdot \mathbf{X}_e \right) / \partial \mathbf{X}_e \right] \cdot dV \cdot \mathbf{T}^T \tag{4-8}$$

$$\mathbf{K}_{ext} = -\partial \mathbf{F}_e / \partial \mathbf{X}_e \tag{4-9}$$

where $\mathbf{G}$ is a matrix linking the nodal degrees of freedom to a displacement gradient vector [144], $\mathbf{M}$ is a stress matrix whose elements can be found in [137], and $\mathbf{F}_e$ is the external force vector. Computation of the skew-symmetric external stiffness matrix is given in [142]. $\mathbf{F}_e$ must be written in the unknown deformed configuration:

$$\mathbf{F}_e = \mathbf{T} \cdot \left(p \cdot A / 3 \right) \cdot \left[\mathbf{I} \quad \mathbf{I} \quad \mathbf{I} \right]^T \cdot \mathbf{n} \tag{4-10}$$

where A is the deformed area of the triangle, p is the uniform pressure over the element, $\mathbf{I}$ is the identity matrix, and $\mathbf{n}$ is the unit normal vector to the deformed triangular finite element. The resulting non-linear set of equations is solved with Newton's recurrence formula [142].

The above method essentially separates the linear and nonlinear stiffness contributions. If the pre-stress in the membrane is very large, $\mathbf{K}_w$ will overwhelm its nonlinear counterparts, and membrane response will be essentially linear for small pressures and displacements. Continued

inflation will transition from linear to nonlinear response [145]. In the event of a slack membrane, the membrane's initial response to a pressure will have an infinite slope until strains develop and provide stiffness. Numerous membrane wing models use some variant of the geometrically nonlinear model described above: Stanford et al. [43], Ormiston [15], Smith and Shyy [72], Jackson and Christie [76], and Levin and Shyy [104].

Inflatable Diaphragm Validation. In order to validate the above membrane models, the material properties of the latex are first identified with a uni-axial tension test. The test specimen has a width of 20 mm, a length of 120 mm, and a thickness of 0.12 mm. The latex rubber sheets are formed in a rolling process, implying an orthotropy, though specimens cut from different orientations yield very similar results. VIC is used to monitor both the extensional and the Poisson strains: data is sampled at 50 pixel locations within the membrane strip, and then averaged. The resulting data can be seen in Figure 4-4, and is used to identity the linear elastic modulus and the Poisson's ratio. A linear fit through the stress-strain curve results in a modulus of 2 MPa; the nonlinear stress-softening behavior for higher strains is the hallmark of hyperelasticity [146]. The Poisson's ratio for small strains is 0.5, a result of the material's incompressibility.

Using these material parameters to construct the constitutive matrix $\mathbf{A_m}$, the finite element model can be appropriately validated with the Hencky test [144]: a flat circular membrane (with or without pre-tension), clamped along its boundary, and subjected to a uniform pressure [145]. A 57.15 mm radius is chosen in order to emulate the length scale of a micro air vehicle. Although the problem is axisymmetric, a full circular mesh is used for numerical computations. Experimentally, VIC is used to monitor the shape of the membrane, while a Heise pressure transducer measures the pressure within a chamber, to the top of which the membrane sheet is

fixed. Results are given in Figure 4-5, in terms of the displacement of the membrane center (normalized by the radius) versus pressure.

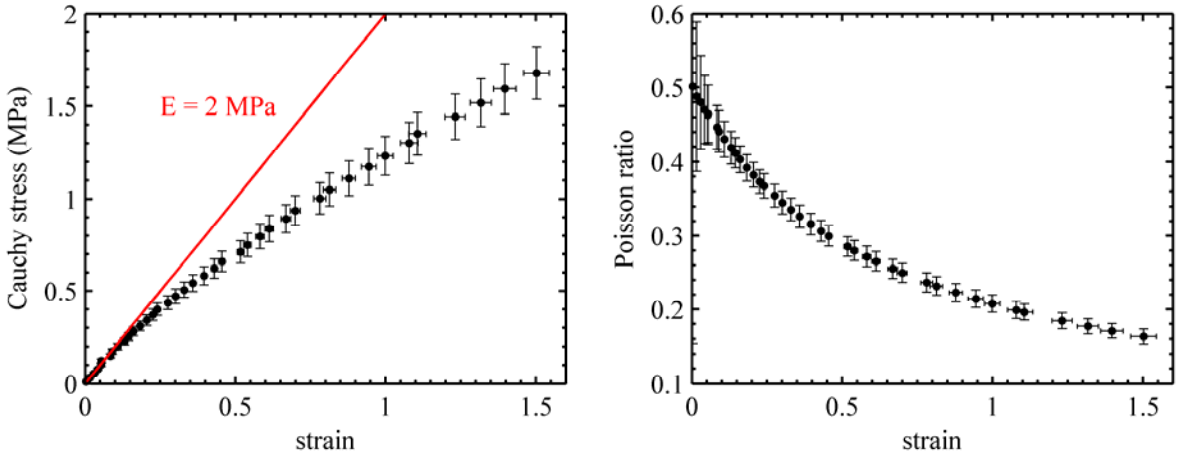

Figure 4-4. Uni-axial stretch test of a latex rubber membrane.

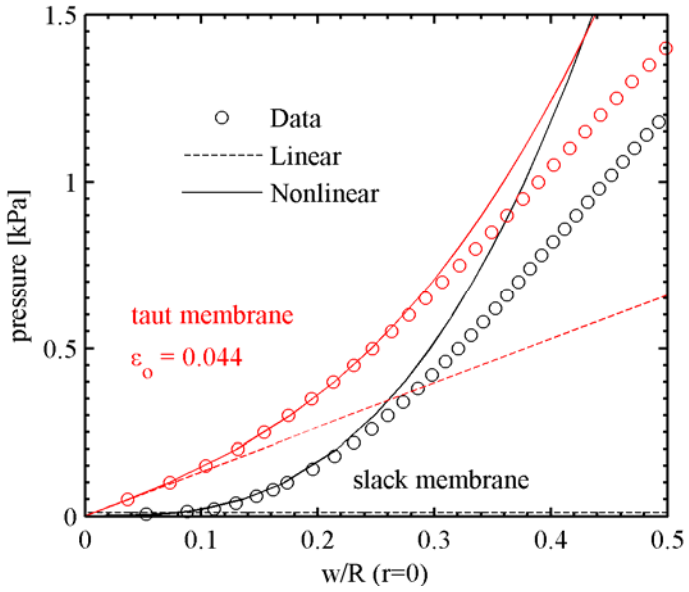

Figure 4-5. Circular membrane response to a uniform pressure.

Two cases are considered: a slack membrane, and a taut membrane. Computational results from both the linear and the nonlinear models formulated above are given. As expected, the response of the slack membrane to an applied pressure is at first unbounded, but becomes finite with the advent of the extensional strains. The linear model is useless for a slack membrane (unbounded), but the nonlinear model can predict this behavior. The correlation between model

and experiment is adequate up to w/R = 0.22 (slightly lower than the value given by Pujara and Lardner [140]), when the model begins to under-predict the inflated shape. Hyperelastic effects appear after this point: Hooke's law over-predicts the stress for a given strain level (Figure 4-4), and thus the membrane's resistance to a transverse pressure.

For the case with membrane pre-tension, VIC is used to measure the pre-strain in the membrane skin (applied radially [147]), the average of which is then used for finite element computations. The mean pre-strain is 0.044, with a coefficient of variation of 3.1%. For this case, the linear model now has a small range of validity, up to w/R = 0.15. Prior to this deformation level, linear and nonlinear models predict the same membrane inflation. The response then becomes nonlinear, due to the advent of finite strains, but also because a relevant portion of the uniform non-conservative pressure is now directly radially, rather than vertically. The nonlinear model and experiment now diverge at w/R = 0.3: the addition of a pre-tension field increases the range of validity of both the linear and the nonlinear membrane models.

Skin Pre-tension Considerations

A state of uniform membrane pre-tension, though numerically convenient [15] [80] [14], is essentially impossible to actually fabricate on a MAV wing. One reason is that the latex sheets used on the MAVs in this work are not much wider than the wingspan, subjecting the state of pre-stress to end-effects. This may perhaps be remedied with larger sheets and a biaxial tension machine, which hardly seems worth the effort for MAV construction. Another problem is the fact that the wing is not a flat surface. Even if a state of uniform pre-tension were attainable, it cannot be transferred to the wing without significant field distortions, particularly due to the camber in the leading edge. A typical pre-strain field is given in Figure 4-6, as measured by the VIC system off of a BR wing in the chordwise direction. The contour on the left is the pre-strain field after the spray adhesive has dried, but before the latex surrounding the wing has been de-

pinned from the stretching frame (as discussed above). The contour on the right of Figure 4-6 is the pre-strain after the excess latex has been trimmed away.

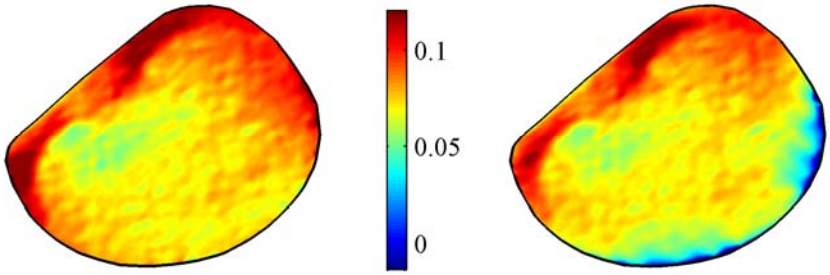

Figure 4-6. Measured chordwise pre-strains in a BR wing before the tension is released from the latex (left), and after (right).

The pre-strains measured from the carbon fiber areas of the wing (leading edge, root, battens) are meaningless, as the shell mechanics largely govern the response in these areas. The large extensional strains (~12%) at the leading edge are indicative of the fact that the wing skeleton is flattened against the membrane until the spray glue dries. At this point, the wing is allowed to re-camber, causing the latex adhered to its top surface to stretch. The anisotropic nature of the pre-tension field is very evident, with strains ranging from between 4% to 9% on the left semi-wing and slightly higher on the right. Furthermore, when the surrounding latex is de-pinned from its frame the membrane at the trailing edge contracts, leaving an area of almost no tension (right side of Figure 4-6). This is a result of the BR wing's free trailing edge, and would not be a problem with a perimeter-reinforced wing.

One numerical solution to such a problem is to interpolate the data of Figure 4-6 onto the finite element grid, and compute the pre-stress within each element, as discussed by Stanford et al. [43]. This method, though accurate, would require an experimental VIC analysis in conjunction with every numerical analysis; not a cost-effective method for thorough exploration of the design space. Eq. (4-4) however, is a natural smoothing operator [139]; simply averaging the pre-strains for the computations, though crude, can in some cases be relatively accurate. The

match between measured and predicted membrane deformation for the taut case in Figure 4-5 is very good, despite the fact that the numerical pre-strains were presumed uniform.

The error resulting from a uniform pre-stress assumption can be estimated with the following method. The pre-strain distribution throughout a flat circular membrane is considered a normally-distributed random variable: each finite element has a different pre-strain. The linear membrane model of Eq. (4-4) is then used to compute the displacement at the center of the membrane due to a hydrostatic pressure. The same membrane is then given a constant pre-strain distribution (the average value of the randomly-distributed pre-strain), and the central deflection is recomputed for comparison purposes. Monte Carlo simulations are then used to estimate the average error at the membrane center, for a given coefficient of variation of the pre-strain.

The results of the Monte Carlo simulation are given in Figure 4-7. Each data point is the percentage error between the central displacement computed with a non-homogenous random pre-strain, and that with a constant pre-strain. Each error percentage is the average of 500 finite element simulations. The radius of the circle is 57.15 mm, the thickness is 0.12 mm, the elastic modulus is 2 MPa, the Poisson's ratio is 0.5, and the hydrostatic pressure is fixed at 200 Pa. The mean pre-strain is 0.05, and the standard deviation is decided by the COV of each data point's abscissa. Nonlinear membrane modeling is not used. The smoothing nature of the Laplacian operator in Eq. (4-4) is very evident: even in the presence of 30% spatial pre-strain variability, the error in assuming a constant pre-strain is still less than 5%. On one hand, the error in Figure 4-7 is probably under-predicted, as strain cannot truly be a spatially-random variable: on a local scale measured strain may seem random, but on a global scale it must satisfy the compatibility equations [146]. Both of these scale-trends are evident in Figure 4-6. On the other hand, Figure 4-7 represents the worst case scenario, as nonlinear membrane effects will dilute the importance

of the pre-tension [145], whatever it's distribution throughout the membrane skin.

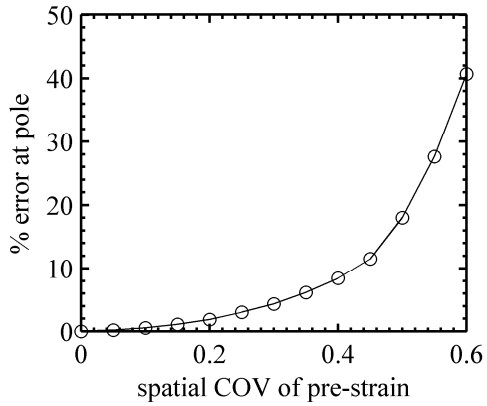

Figure 4-7. Monte Carlo simulations: error in the computed membrane deflection due to a spatially-constant pre-strain distribution assumption.

Though the above results indicate the appropriateness of using a constant membrane pre-stress for MAV wing computations (despite an inability to reproduce this in the laboratory), the tension relaxation at the free trailing edge of the BR wing (seen in Figure 4-6) should be corrected for. Regardless of the amount of pre-tension placed in a batten-reinforced membrane, the pre-stress traction normal to the free trailing edge will always be zero, producing a stress gradient. This can be accounted for in the following manner:

1. Specify the pre-stress field within the membrane skin (uniform or otherwise).
2. Compute the traction due to this pre-stress along the outward normal, at each edge in a membrane finite element that coincides with a free surface.
3. Apply a transverse pressure along each edge, equal and opposite to the computed traction.
4. Compute the resulting stress field (while holding the carbon fiber regions of the wing rigid), add this field to the prescribed stress in step 1, and use the result as the new pre-stress resultant field for aeroelastic computations.

The resulting pre-stress field will be very small along the free edge, and approach the original specified value deeper into the wing towards the leading edge, as can be seen in Figure 4-8. For this example, about a fourth of the membrane area is affected by the free edge, while the remainder retains a pre-stress close to the prescribed value (a result validated by Figure 4-6).

As mentioned above, this pre-stress correction only needs to be applied for simulations of a batten-reinforced wing.

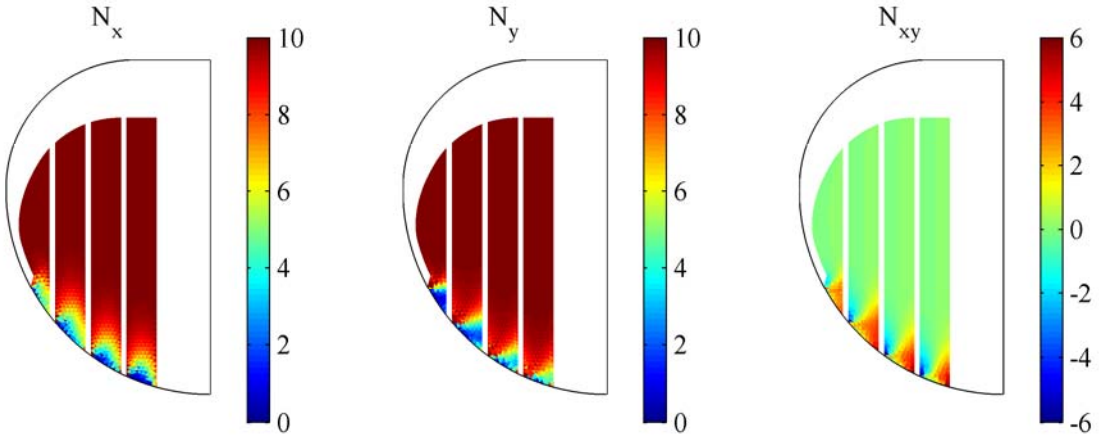

Figure 4-8. Computed pre-stress resultants (N/m) in the chordwise (left), spanwise (center), and shear (right) in a BR wing, corrected at the trailing edge for a uniform pre-stress resultant of 10 N/m.

Fluid Solvers

As discussed above, several viscous effects dominate the flow about a micro air vehicle wing: laminar separation, turbulent transition and reattachment, periodic shedding and pairing, and three-dimensional flow via wing tip vortex swirling. An inviscid flow solved such as the vortex lattice method is unable to predict any of these effects (drag, in particular, will be severely underestimated), but its small computational expense is attractive. Solving the steady Navier-Stokes equations represents a substantial increase in cost, but an equally large step forward in predictive capability. Some aspects of the flow (namely, turbulent transition over a separation bubble, and subsequent shedding), still cannot be predicted with the methods presented here.

Vortex Lattice Methods

This section briefly describes a well-developed family of methods for predicting the steady lifting flow and induced drag over a thin wing at small angles of attack. The continuous distribution of bound vorticity over the wing is approximated by discretizing the wing into a

paneled grid, and placing a horseshoe vortex upon each panel. Each horseshoe vortex is comprised of a bound vortex (which coincides with the quarter-chord line of each panel), and two trailing vortices extending downstream. Each vortex filament creates a velocity whose magnitude is assumed to be governed by the Biot-Savart law [27]. Furthermore, a control point is placed at the three-quarter-chord point of each panel.

The velocity induced at the m^{th} control point by the n^{th} horseshoe vortex is:

$$u_{m,n} = C^{x}_{m,n} \cdot \Gamma_n \quad v_{m,n} = C^{y}_{m,n} \cdot \Gamma_n \quad w_{m,n} = C^{z}_{m,n} \cdot \Gamma_n \tag{4-11}$$

where u, v, and w are the flow velocities in Cartesian coordinates, Γ is the vortex filament strength, and C^{i} are influence coefficients that depend on the geometry of each horseshoe vortex and control point combination. The complete induced velocity at each control point is the sum of the contributions from each horseshoe vortex, resulting in a linear system of equations.

The strength of each vortex must be found so that the resulting flow is tangent to the surface of the wing: the wing becomes a streamline of the flow. This requirement is enforced at each control point by:

$$\left\{ U_\infty \cdot \cos(\alpha) + u_m \quad v_m \quad U_\infty \cdot \sin(\alpha) + w_m \right\} \cdot \nabla F(x_m, y_m, z_m) = 0 \tag{4-12}$$

where U_∞ is the free-stream velocity, α is the angle of attack, and $F(x,y,z) = 0$ is the equation of the surface of the wing. Inserting the relevant terms of Eq. (4-11) into Eq. (4-12) provides a linear system of equations for the filament strength of each horseshoe vortex. Micro air vehicle simulations that utilize a vortex lattice method are typically forced to do so by the computational requirements of optimization (as is the case in the current work). Examples can be seen in the work of Ng and Leng [52], Sloan et al. [53], and Stanford et al. [61].

Steady Navier-Stokes Solver

The three-dimensional incompressible Navier-Stokes equations, written in curvilinear

coordinates, are solved for the steady, laminar flow over a MAV wing. As before, the fuselage, stabilizers, and propeller are not taken into account. The computational domain can be seen in Figure 4-9, with the MAV wing enclosed within. Inlet and outlet boundaries are marked by the flow vectors; velocity is specified at the inlet, and a zero-pressure boundary condition is enforced at the outlet. The configuration shown in Figure 4-9 is for simulations at a model inclination of 0° angle of attack. For non-zero angles, the lower and upper surfaces will also see a mass flux, rather than re-meshing the wing itself. The sidewalls are modeled as slip walls, and thus no boundary layer forms. The MAV wing itself is modeled as a no-slip surface.

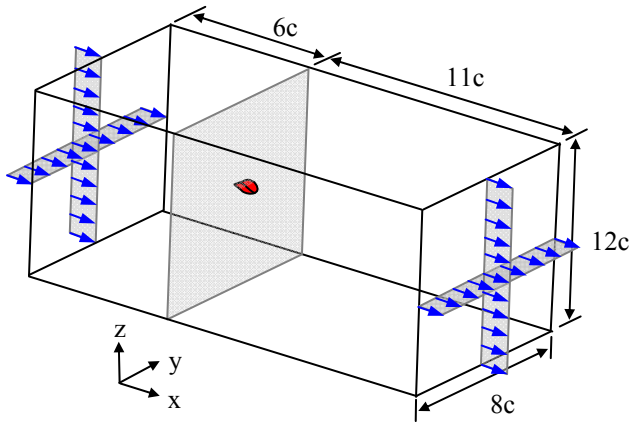

Figure 4-9. CFD computational domain.

Because no flow is expected to cross the root-chord of the wing (unsteady effects that may lead to bilateral asymmetry [6] are not included; nor is propeller slipstream [45]), symmetry is exploited by modeling only half of the computational domain (the plane of symmetry is also modeled as a slip wall). A detailed view of the resulting structured mesh (the nodes that lie on the plane of symmetry and the MAV wing) is given in Figure 4-10. 210,000 nodes fill half of the computational domain, with 1300 nodes on the wing surface. This is a multi-block grid, with four patches coinciding with the upper and lower wing surfaces. The wing itself has no thickness. Such a flow model should be able to adequately predict the strong tip vortex swirling

system (and the accompanying nonlinear lift and moment curves [3]), as well as the laminar flow separation against an adverse pressure gradient [2]. Similar laminar, steady flow computations for low Reynolds number flyers can be found in the work of Smith and Shyy [72], Viieru et al. [38], and Stanford et al. [43].

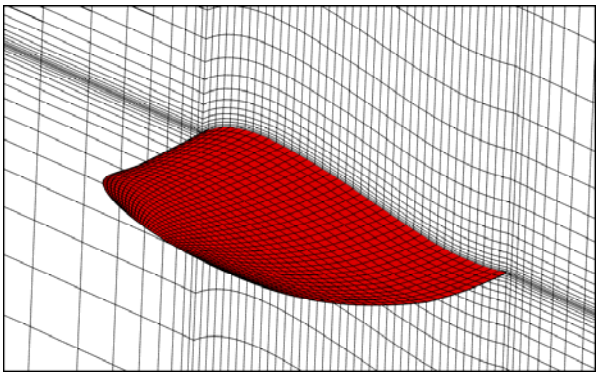

Figure 4-10. Detail of structured CFD mesh near the wing surface.

In order to handle the arbitrarily shaped geometries of a micro air vehicle wing with passive shape adaptation, the Navier-Stokes equations must be transformed into generalized curvilinear coordinates: $\xi(x,y,z)$, $\eta(x,y,z)$, $\zeta(x,y,z)$. This transformation is achieved by [148]:

$$\begin{bmatrix} \xi_x & \xi_y & \xi_z \\ \eta_x & \eta_y & \eta_z \\ \zeta_x & \zeta_y & \zeta_z \end{bmatrix} = \frac{1}{J} \cdot \begin{bmatrix} f_{11} & f_{12} & f_{13} \\ f_{21} & f_{22} & f_{23} \\ f_{31} & f_{32} & f_{33} \end{bmatrix} \tag{4-13}$$

where f_{ij} are metric terms, and J is the determinant of the transformation matrix:

$$J = \frac{\partial(x, y, z)}{\partial(\xi, \eta, \zeta)} \tag{4-14}$$

Using the above information, the steady Navier-Stokes equations can then be written in three-dimensional curvilinear coordinates [149]. The continuity equation and u-momentum equation are presented here in strong conservative form, with the implication that the v- and w-momentum equations can be derived in a similar manner.

$$U_\xi + V_\eta + W_\zeta = 0 \tag{4-15}$$

$$\begin{aligned}
&\frac{\partial(\rho \cdot U \cdot u)}{\partial \xi} + \frac{\partial(\rho \cdot V \cdot u)}{\partial \eta} + \frac{\partial(\rho \cdot W \cdot u)}{\partial \zeta} = \frac{\partial}{\partial \xi}\left[\frac{\mu}{J} \cdot \left(q_{11} \cdot u_\xi + q_{12} \cdot u_\eta + q_{13} \cdot u_\zeta\right)\right] \\
&+ \frac{\partial}{\partial \eta}\left[\frac{\mu}{J} \cdot \left(q_{21} \cdot u_\xi + q_{22} \cdot u_\eta + q_{23} \cdot u_\zeta\right)\right] + \frac{\partial}{\partial \zeta}\left[\frac{\mu}{J} \cdot \left(q_{31} \cdot u_\xi + q_{32} \cdot u_\eta + q_{33} \cdot u_\zeta\right)\right] \\
&- \left[\frac{\partial(f_{11} \cdot p)}{\partial \xi} + \frac{\partial(f_{21} \cdot p)}{\partial \eta} + \frac{\partial(f_{31} \cdot p)}{\partial \zeta}\right]
\end{aligned} \tag{4-16}$$

where ρ is the density, p is the pressure, μ is the viscosity, q_{ij} are parameters dictated by the transformation (expressions can be found in [149]), and U, V, and W are the contravariant velocities, given by the flux through a control surface normal to the corresponding curvilinear directions:

$$\begin{aligned}
U &= f_{11} \cdot u + f_{12} \cdot v + f_{13} \cdot w \\
V &= f_{21} \cdot u + f_{22} \cdot v + f_{23} \cdot w \\
W &= f_{31} \cdot u + f_{32} \cdot v + f_{33} \cdot w
\end{aligned} \tag{4-17}$$

In order to numerically solve the above equations, a finite volume formulation is employed, using both Cartesian and contravariant velocity components [148]. The latter can evaluate the flux at the cell faces of the structured grid and enforce the conservation of mass. A second order central difference operator is used for computations involving pressure and diffusive terms, while a second order upwind scheme handles all convective terms [150].

Fluid Model Comparisons and Validation

Validation of both the linear vortex lattice method and the nonlinear CFD is given in Figure 4-11, in terms of lift, drag, and longitudinal pitching moments (measured about the leading edge) at 13 m/s. Pre-stall, the CFD model is able to accurately predict lift and drag within the experimental error bars of the measured data. Drag is consistently over-predicted at higher angles of attack; turbulent reattachment of separated flow is know to decrease the profile

drag [8], but is not included in the model. The magnitude of the pitching moment is slightly over-predicted by the CFD, though the data still falls within the error bars, the slopes match well, and the onset of nonlinear behavior (due to the low aspect ratio [3]) is well-predicted. The CFD is also able to predict the onset of stall (via a loss of lift) at about 21°, but loses its predictive capability in the post-stall regime, as the flow is known to be highly unsteady.

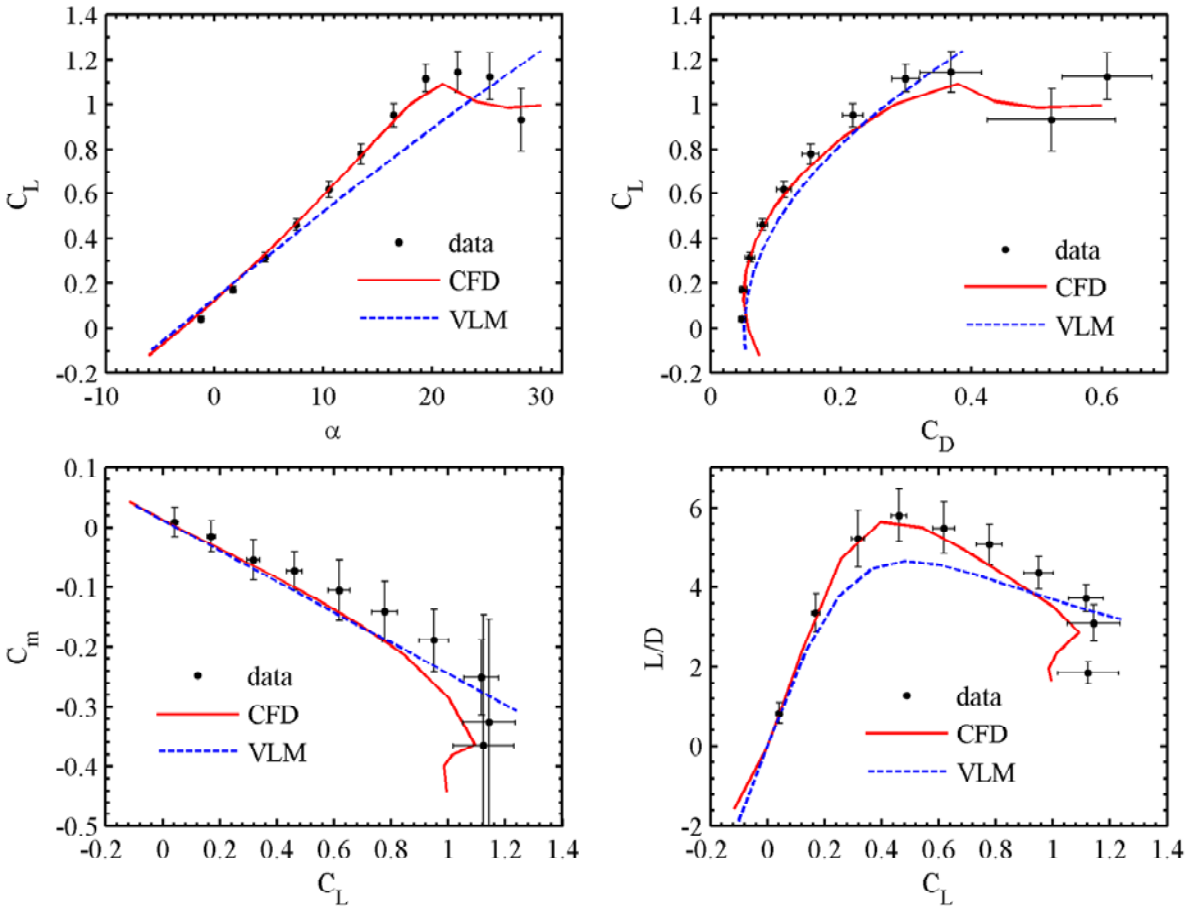

Figure 4-11. Computed and measured aerodynamic coefficients for a rigid MAV wing, Re = 85,000.

The vortex lattice method is accurate at low angles of attack, but the slope is under-predicted (possibly due to an inability to compute the low-pressure cells at the wing tips, similar to vortex lift discrepancies seen in delta wings [27]), and the wing never stalls. The drag predicted by the vortex lattice method is necessarily augmented by a non-zero C_{Do} (estimated

from the experimental data), and is moderately accurate up to 10° angle of attack. After this point, the inviscid drag is under-predicted due to massive flow separation over the wing. No significant differences can be seen between the pitching moments predicted by the CFD and the vortex lattice method, until the aforementioned nonlinear behavior appears, which the inviscid solver cannot predict.

Aeroelastic Coupling

Transfer of data between a structured CFD mesh and an unstructured FEA mesh is done with simple polynomial interpolation. If information from grid A is to be interpolated to grid B, the element from grid A (triangular for the FEA mesh, quadrilateral for the CFD mesh) is found which is closest to each node from grid B. Except for nodes that lie on the wing border, these elements will enclose their corresponding nodes. Polynomial shape functions for the desired variable are formulated to describe its distribution within the element, and then the value at the node is solved for. Such a method is found to adequately preserve the integrated forces and the strain energies from one mesh to another, and is fairly inexpensive.

The un-deformed (due to aerodynamic loads) wing shape technically depends upon the membrane pre-tension. This shape could be found with Eq. (4-4), setting the pressure source terms to zero, and letting the wing shape at nodes upon the carbon fiber-latex boundary be prescribed displacement boundary conditions. Such a scheme should result in slight concavities along the membrane surface [151]. This effect is considered small, however, and is ignored for the current work. Shear stress over the wing is also not included in the aeroelastic coupling.

Moving Grid Technique

For aeroelastic computations using the Navier-Stokes flow solver, a re-meshing algorithm is needed to perturb the structured grid surrounding the flexible wing (no such module is required when a vortex lattice method is used, as all of the nodes lie on the wing surface). For

the current work, a moving grid routine based upon the master-slave concept is used to maintain a point-matched grid block interface, preserve grid quality, and prevent grid cross-over. Master nodes are defined as grid points that lie on the moving surface (the wing surface of the micro air vehicle, in this case), while the slave nodes constitute the remaining grid points. A slave node's nearest surface point is defined as its master node, and its movement is given by:

$$\tilde{x}_s = x_s + \theta \cdot \left(\tilde{x}_m - x_m \right) \tag{4-18}$$

where x_s is the location of the slave node, x_m is the location of its master node, the tilde indicates a new position, and θ is a Gaussian distribution decay function:

$$\theta = \exp\left[-\beta \cdot \min\left\{ 500, \frac{\left(x_s - x_m\right)^2 + \left(y_s - y_m\right)^2 + \left(z_s - z_m\right)^2}{\left(\tilde{x}_m - x_m\right)^2 + \left(\tilde{y}_m - y_m\right)^2 + \left(\tilde{z}_m - z_m\right)^2 + \varepsilon} \right\} \right] \tag{4-19}$$

where ε is small number to avoid division by zero, and β is a stiffness coefficient; larger values of β promote a more rigid-body movement. Further information concerning this technique is given by Kamakoti et al. [152].

Numerical Procedure

The steady fluid structure interaction of a MAV wing is computed as follows:

1. If computations involve a batten-reinforced wing, correct for the membrane pre-tensions at the free trailing edge.
2. Solve for the aerodynamic pressures over the wing, using either the steady Navier-Stokes equations or the tangency condition of the vortex lattice method.
3. Interpolate the computed pressures from the flow solver grid to the FEA grid.
4. Solve for the resulting wing displacement using either the linear or the nonlinear membrane/carbon fiber model.
5. Interpolate the displacement onto the MAV wing of the flow solver grid.
6. If nonlinear CFD models are utilized, re-mesh the grid using the master/slave scheme.
7. Repeat steps 2-6 until suitable convergence is achieved: less than 0.1% change in the lift.

Less than ten iterations are usually adequate at modest angles of attack ($3^o<\alpha<18^o$). Typical results are given in Figure 4-12 for the lift and efficiency of both a BR and a PR wing, computed with a Navier-Stokes flow solver and a nonlinear membrane solver. The lift of the PR wing monotonically converges (lift increases camber, which further increases lift), while the history of a BR wing is staggered (lift decreases wing twist, decreasing lift). For the nonlinear modules, step 2 requires between 150 and 250 sub-iterations, while step 4 can typically converge within 20 sub-iterations. For the linear modules, the equations of state can be solved for directly.

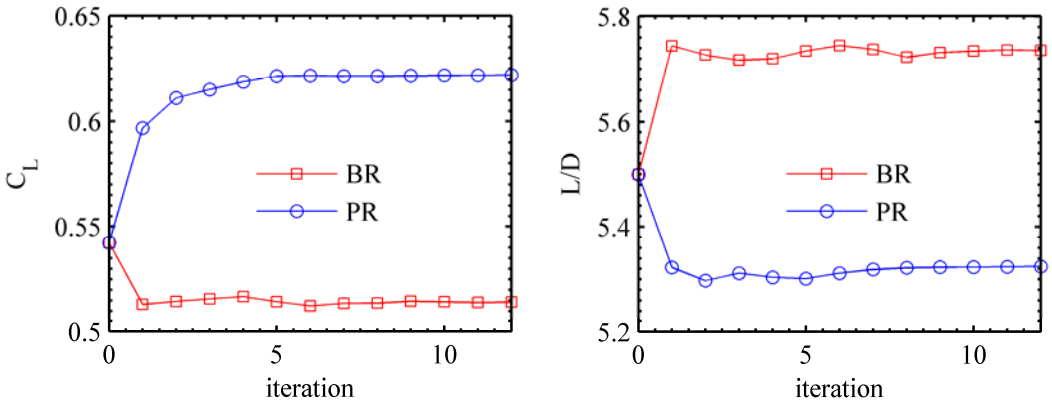

Figure 4-12. Iterative aeroelastic convergence of membrane wings, $\alpha = 9°$.

CHAPTER 5
BASELINE WING DESIGN ANALYSIS

Three "baseline" micro air vehicle wing designs are considered in this section: first, a completely rigid wing. Secondly, a batten-reinforced wing with no pre-tension in the membrane skin, two layers of bi-directional carbon fiber at ply angles of 45º to the chord line (at the root and leading edge), and one layer of uni-directional carbon fiber (fibers aligned in the chordwise direction) for the battens. Third, a perimeter-reinforced wing with no pre-tension in the membrane skin and two layers of bi-directional carbon fiber at ply angles of 45º to the chord line (at the root, leading edge, and perimeter).

As a large number of function evaluations are not required for this strictly analysis section, all numerical results are computed with the higher-fidelity methods discussed above: the steady Navier-Stokes solver and the nonlinear membrane solver. Furthermore, all results are found at U_∞ = 15 m/s, a value towards the upper range of MAV flight. A higher velocity is chosen to emphasize aeroelastic deformations. For a given flight condition, 10 VIC images are taken of the deformed wing (at 1 Hz) and averaged together. Sting balance results are, as discussed, sampled at 1000 Hz for 2 seconds, and then averaged.

Wing Deformation

Numerical and experimental out-of-plane displacements, normalized by the root chord, are given in Figure 5-1 for a BR wing, along with a section of the data at x/c = 0.5, at 15º angle of attack. As expected, the primary mode of wing deformation is a positive deflection of the trailing edge, resulting in a nose-down twist of each flexible wing section. Deformations are relatively small (~5%, or 6.2 mm), though still have a significant effect upon the aerodynamics. The membrane inflates from between the battens (clearly seen in the section plot) towards the leading edge, but at the trailing edge the wing shape is more homogenous and smooth, and no

distinction between batten and membrane can be made. This is presumably due to the pressure gradient, with very high forces at the leading edge which dissipates down the wing. The carbon fiber wing tips, though several orders of magnitude stiffer than the membrane, shows appreciable twisting, indicative of the large suction forces from the tip vortex. Correlation between model and experiment is acceptable, with the model slightly under-predicting the adaptive washout, and over-predicting the local membrane inflation between the battens. Wing shapes and magnitudes match well with time-averaged results reported by Lian et al. [28].

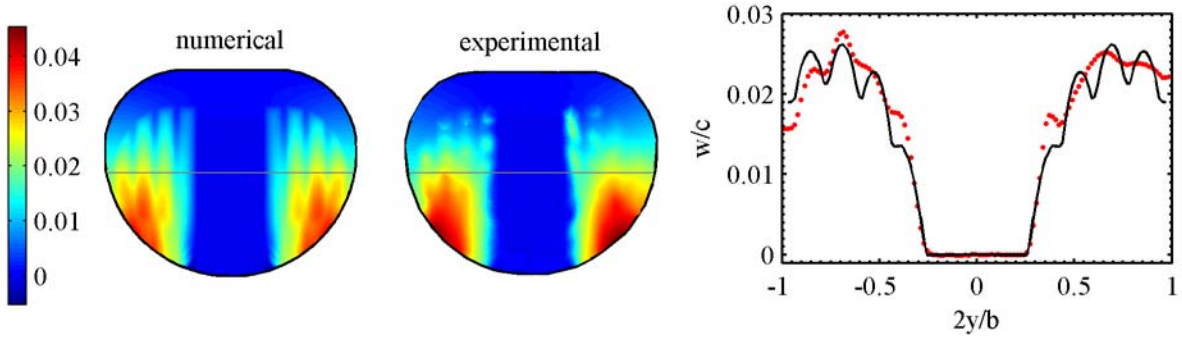

Figure 5-1. Baseline BR normalized out-of-plane displacement (w/c), $\alpha = 15^{o}$.

Chordwise strains for the same case as above can be seen in Figure 5-2. The directional stiffness of the battens generally prevents significant stretching in the chordwise direction. The model predicts appreciable strain (1.4%) at the carbon fiber/membrane interface towards the leading edge (due to inflation), almost no strain near the mid-chord region, and negative Poisson strains at the trailing edge. Strains in the carbon fiber regions, while computed, are much smaller than the membrane strains, and cannot be discerned in Figure 5-2. The measured chordwise strain is very small and noisy, with no evident differences between the carbon fiber and membrane regions. Much of the measured field lies below the system's strain resolution (~1000 με). Several noise spikes are also evident in this strain field, while the displacement field in Figure 5-1 has none; the strain differentiation procedure is more sensitive to experimental noise than the displacement temporal matching.

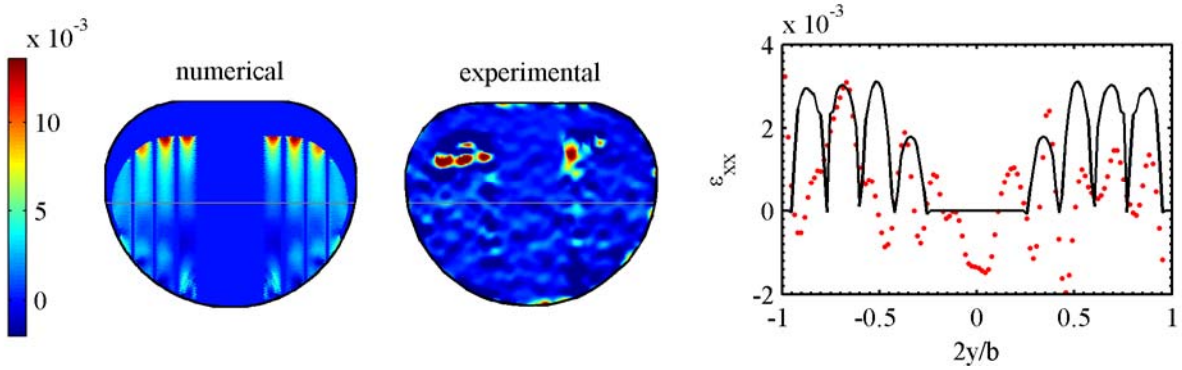

Figure 5-2. Baseline BR chordwise strain (ε_{xx}), $\alpha = 15°$.

A better comparison between model and experiment is given in Figure 5-3, with the spanwise strains. These extensions are essentially a product of the change in distance between the battens as they deform. Both model and experiment indicate a peak in ε_{yy} between the inner batten and the carbon fiber root, though the model indicates this maximum towards the leading edge (~1.2%), while the measurement places it farther aft. Strain concentrations at the trailing edge are visible in both fields. Though still noisy, the VIC system's spanwise strain can differentiate between battens and membrane. Suitable model validation is also seen in shear (Figure 5-4). Both peaks and distributions of the anti-symmetric shear are well predicted. The tips of the battens at the trailing edge cause a shear concentration, typically of opposite sign to the strain in the rest of the membrane segments between each batten.

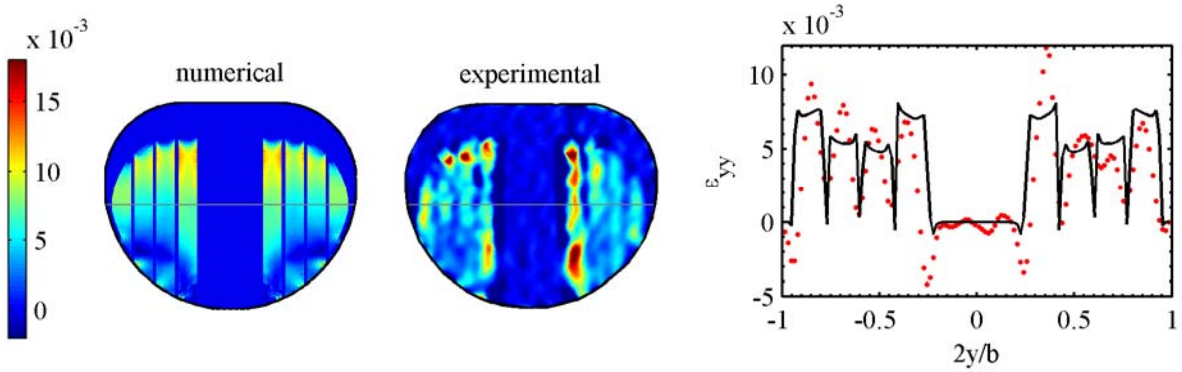

Figure 5-3. Baseline BR spanwise strain (ε_{yy}), $\alpha = 15°$.

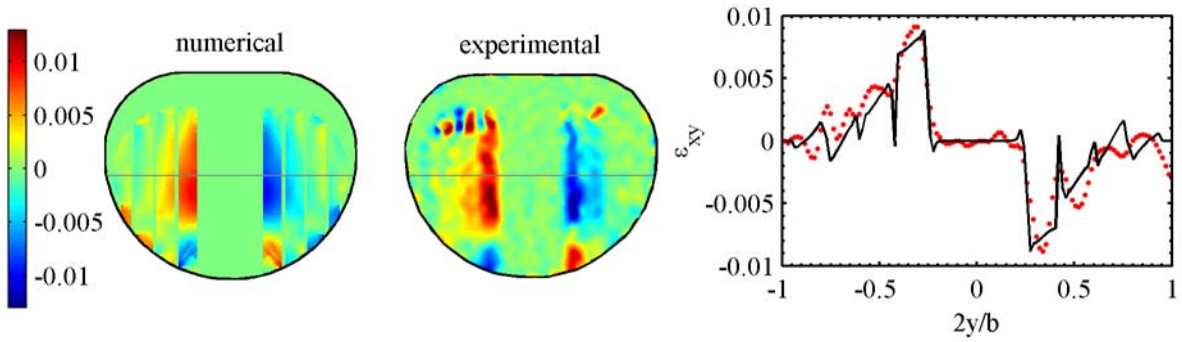

Figure 5-4. Baseline BR shear strain (ε_{xy}), $\alpha = 15^{o}$.

Normalized out-of-plane displacements for the perimeter-reinforced wing are given in Figure 5-5. Deformations are slightly larger than with the BR wing (6%), and are dominated by the membrane inflation between the carbon fiber leading and trailing edges. The membrane apex occurs approximately in the middle of the membrane skin, despite the pressure gradient over the wing. This location is a function of angle of attack, as the peak will move slightly forward with increased incidence [74], [43]. The carbon fiber wing tip twists less than previously, thought to be a result of the fact that the wingtip is not free in a PR configuration, but attached to the trailing edge by the laminate perimeter. Some bending of the leading edge at the root can also be seen, but not in the BR wing (Figure 5-1). Correspondence between model and experiment is suitable, with the model again under-predicting wing deformation, but accurately locating the apex. Slight asymmetries in the measured wing profile (also evident in the BR wing) are probably a result of manufacturing errors (particularly in the application of the membrane skin tension), and not due to flow problems in the wind tunnel.

As the amount of unconstrained membrane is greater in a PR wing than in a BR wing, chordwise strains (Figure 5-6) are much larger as well: peak stretching (3%) is located at the membrane/carbon fiber boundary towards the leading edge, as before. The magnitude and size of this high-extension lobe is over-predicted by the model. Both model and experiment show a region of compressive strain aft of this lobe, towards the trailing edge. This is a Possion strain

(and thus not a compressive stress), but the stress in this region does become slightly negative for higher angles of attack. Erroneous computation of compressive membrane stresses indicates the need for a wrinkling module. Though wrinkles in the membrane skin are not obviously visible in the VIC measurements (possibly an unsteady process averaged out with multiple images), wrinkling towards the onset of stall is a well-known membrane wing phenomena [87]. As before, no appreciable strain is measured or computed in the carbon fiber areas of the wing.

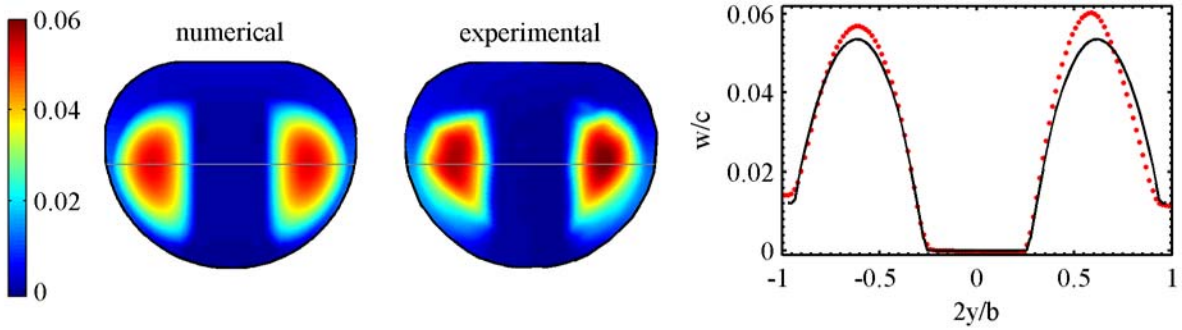

Figure 5-5. Baseline PR normalized out-of-plane displacement (w/c), α = 15º.

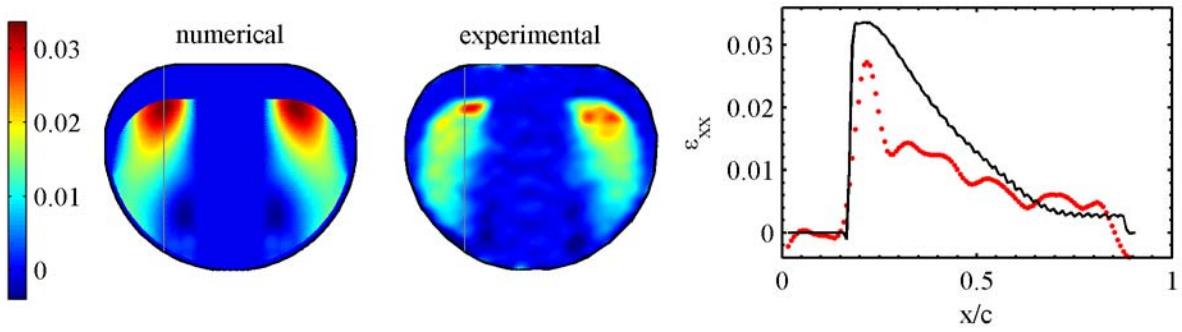

Figure 5-6. Baseline PR chordwise strain (ε_{xx}), α = 15º.

Peak spanwise stretching (Figure 5-7) occurs at the membrane carbon fiber interface towards the center of the wing root, and is well predicted by the model. The computed strain field erroneously shows a patch of negative Poisson strain towards the leading edge, due to the high chordwise strains in this area. One troubling aspect of the measured spanwise strains is the areas of negative strains along the perimeter of the membrane skin: namely on the sidewalls towards the root and the wingtip. Such strains have been measured in previous studies [9], but

their presence is peculiar. Basic membrane inflation mechanics indicates large extension at the boundaries rather than compression [145] (as is computed by the model).

The compression may be membrane wrinkling (which, again, is not evident from Figure 5-5, or may be an error in the VIC strain computations, potentially caused by the large displacement gradients in this area of the wing. A third possibility is that the VIC is measuring a bending strain at this point, where the radius of curvature is close to zero. The latex skin, though modeled as a membrane, does have some (albeit very small) bending resistance due to its finite thickness. The anti-symmetric shear strain field (Figure 5-8) shows good correspondence between model and experiment, with accurate computations in-board, but slight under-predictions of the high shear closer to the wingtip.

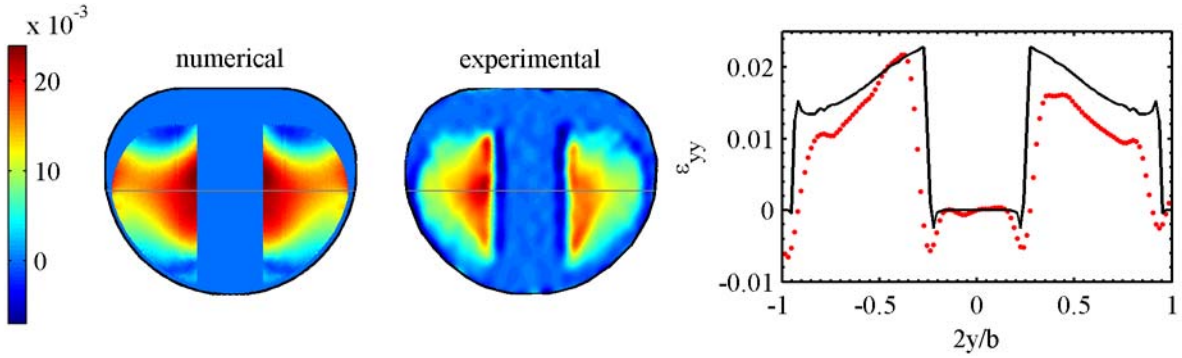

Figure 5-7. Baseline PR spanwise strain (ε_{yy}), $\alpha = 15^{o}$.

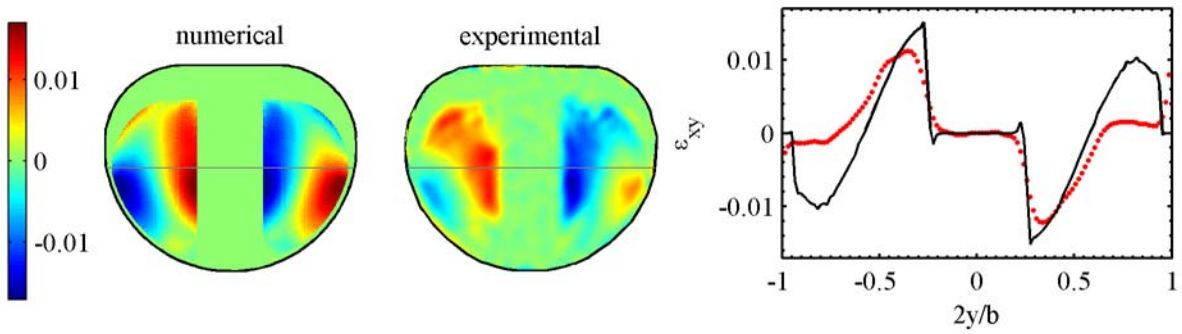

Figure 5-8. Baseline PR shear strain (ε_{xy}), $\alpha = 15^{o}$.

The aerodynamic twist (camber and camber location) and geometric twist angle

distributions for the baseline BR and rigid wings are given in Figure 5-9. The rigid wing is characterized by positive (nose-up) twist and a progressive de-cambering toward the wingtip. The carbon fiber inboard portion of the BR wing exhibits very similar wing twist to the rigid wing. Past 2y/b = 0.3 however, both model and experiment show that the membrane wing has a near-constant decrease in twist of 2-3º: adaptive washout. Though this geometric twist dominates the behavior of the BR wing, the membrane also exhibits some aerodynamic twist. This occurs predominately in the latex between the battens, about 1% of the chord in magnitude. The location of this camber has large variations: some portions of the wing are pushed back from 25% (rigid) to 75% (membrane), as shown by both model and experiment. Shifting the camber aft-ward on low Reynolds number wings is one method to hinder flow separation through control of the pressure gradient [27], and may play a role in the BR wing's delayed stall as well.

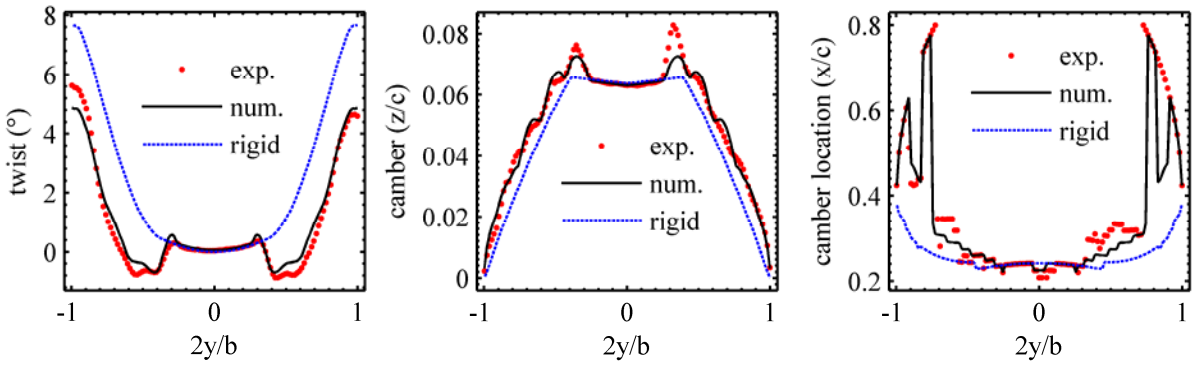

Figure 5-9. Baseline BR aerodynamic and geometric twist distribution, α = 15º.

The aerodynamic and geometric twist distributions for the baseline PR and rigid wings are given in Figure 5-10. Membrane inflation adaptively increases the camber by as much as 4%, though this figure is slightly under-predicted by the model. The location of this camber is shifted aft-ward, though not as much as with the BR wing. The flexible laminate used for the wing skeleton pushes the location of the camber at the root slightly forward. Like the BR wing deformation, shape changes over the PR wing are a mixture of both aerodynamic and geometric

twist (though the former dominates). The laminated perimeter deflects upward farther than the leading edge, resulting in a slight nose down twist. This is as much as 2º at the wingtips, slightly under-predicted by the model.

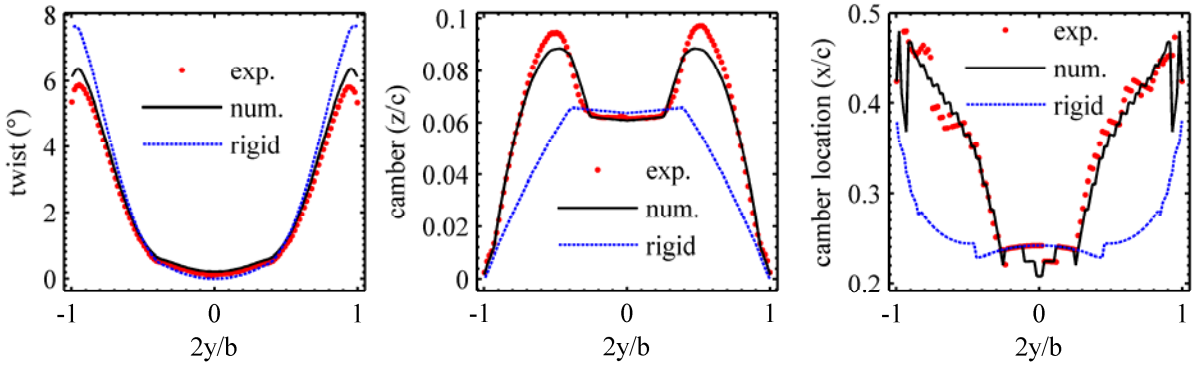

Figure 5-10. Baseline PR aerodynamic and geometric twist distribution, α = 15º.

Wing twist and camber throughout the entire α-sweep are given in Figure 5-11, at a flexible wing section at 2y/b = 0.65. The master slave moving grid algorithm [152] fails with BR wings at angles of attack higher than 20º: the steep displacement gradients between the carbon fiber root and the membrane skin leads to excessive shearing within the CFD mesh surrounding the wing.

The nose-down twist of both the BR and the PR wing increase monotonically with angle of attack, thought the former is obviously much larger. Experimentally measured BR wing twist has a linear trend (up to stall at about 22º) with α, while the numerical curve is more nonlinear, and under-predicts twist at moderate angles. Both model and experiment demonstrate a moderate increase in camber of the BR wing, with a linear trend in α up to stall. After stall, the camber of the BR wing increases substantially, from 5% to 8%.

The camber of the PR wing is much larger than the rigid wing, even at low and negative angles of attack. This is due to the lack of pre-tension: even a moderate amount of force will cause substantial deformations [147]. Both measurements and simulations of the PR wing are

difficult at lower angles than shown in Figure 5-11: the membrane is equally apt to lie on either side of the chordline [65], and steady-state solutions don't exist. PR wing camber variations with angle of attack are nonlinear (the development of finite strains cause a 1/3 power law response to the applied load [72]), and are slightly under-predicted by the model.

The location of this camber in a PR wing moves somewhat forward for modest angles, while the BR wing sees a significant aft-ward shift at the onset of stall. Both of these camber location trends are well-predicted by the model. Experimental error bars for camber, though not shown here, are on the order of 10% at low angles, less than 2% at moderate angles, and upwards of 20% in the stalled region [43]. This stems not from uncertainty but from unsteady membrane vibration, possibly due to vortex shedding as discussed by Lian and Shyy [8].

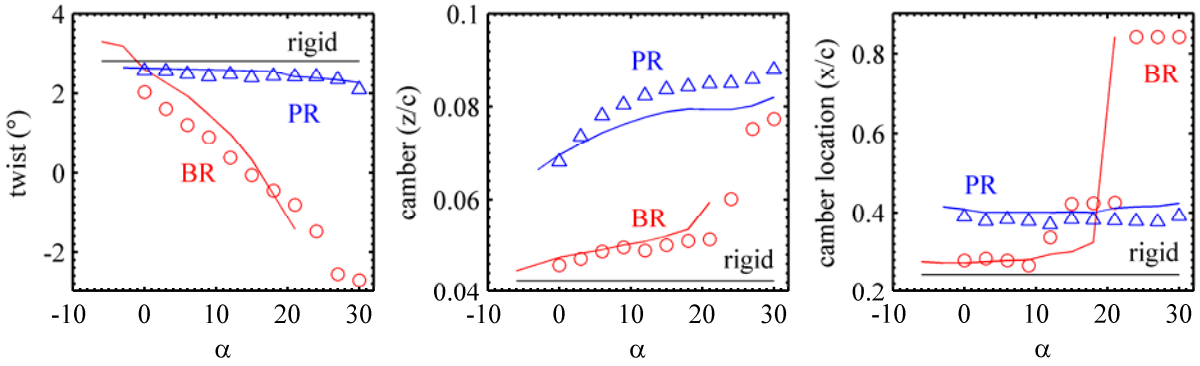

Figure 5-11. Aerodynamic and geometric twist at 2y/b = 0.65.

Aerodynamic Loads

Lift coefficients (both measured and predicted) throughout the α-sweep, with no model yaw, are given in Figure 5-12, for the three baseline wing designs discussed above. For all six data sets, lift slopes are very low (~0.05/º, about half of the value for two-dimensional airfoils [27]) as expected from low aspect ratio wings. The downward momentum from the tip vortices helps mitigate the flow separation, delaying stall to relatively high angles (18º-22º). Focusing first on the rigid wing, mild nonlinearities can be seen in the lift curve. Both model and

experiment indicate an increase in the slope by 25% between 0º and 15º angle of attack. This is presumably due to a growth in the low pressure cells at the wing tips of the low aspect ratio wing [3]. Such nonlinearities should become more prevalent for lower aspect ratios than considered here (1.25). Model and experiment show good agreement for the lift over the rigid wing prior to stall. At stall (where the static model's predictive capability is questionable due to unsteady flow separation [18] and tip vortices [6]) the model slightly under-predicts the stalling angle and $C_{L,max}$; the loss of lift is more severe in the experimental data.

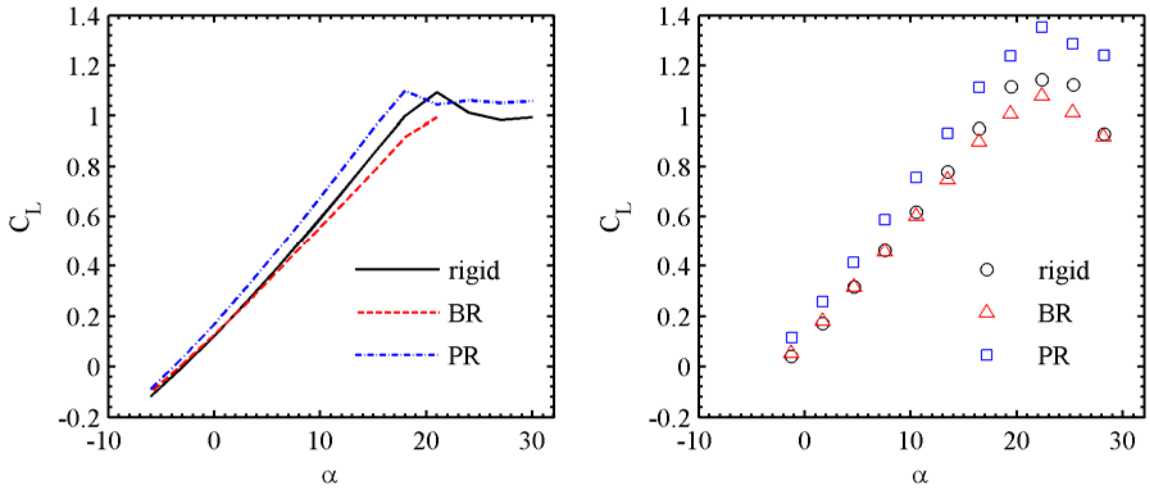

Figure 5-12. Baseline lift coefficients: numerical (left), experimental (right).

The adaptive inflation/cambering of the PR wing substantially increases the lift and the lift slope as compared to the rigid wing. The lift curve of the PR wing is less nonlinear than the rigid wing. This may be due to the nonlinear cambering seen in Figure 5-11, which is known to decrease the lift slope [15] and can offset the growth of the tip vortices. Drastic changes in the lift characteristics at low angles due to hysteresis effects [65], and a gradual onset of stall [89] are not evident in either the numerical or the experimental data, perhaps because a relevant portion of the wing is not composed of the flexible membrane. The model significantly under-predicts $C_{L,max}$ of the PR wing, and erroneously computes that the wing stalls before the rigid

wing. Similar experimental work [9] at lower speeds also show early stall, again indicating the sensitivity of Reynolds number to stall.

At angles of attack below 10º, the BR wing has very similar lift characteristics to the rigid wing, a fact also noted in the work of Lian et al. [28]. This is thought to be due to two offsetting characteristics of a wing with both aerodynamic and geometric twist [67]: the inflation in between each batten increases the lift, while the adaptive washout at the trailing edge decreases the lift. Both of these deformations can be seen in Figure 5-1. At higher angles of attack, the load alleviation from the washout dominates the deformation, and decreases both the lift and the lift slope, as indicated by both model and experiment. Delayed stall is not present in the measurements (though, as with the PR wing, has been measured at lower Reynolds numbers [9]), and numerical BR wing modeling cannot be taken past 20º due to aforementioned problems with the moving boundary.

Figure 5-13 shows drag coefficients through the α-sweep, with good experimental validation of the model. As before, the drag of the rigid and the BR wings are very similar for modest angles of attack. Above 10º the load alleviation at the trailing edge decreases the drag, a streamlining effect [63]. It should be noted however that for a given value of lift, the BR wing actually has slightly more drag than a rigid wing [9]. Regardless of whether the comparative basis is lift or angle of attack, the PR wing has a drag penalty over the rigid wing. This is in part due to the highly non-optimal airfoil shape of each membrane wing section: Figure 5-5 shows the tangent discontinuity of the wing shape at the membrane/carbon fiber interface towards the leading edge. Excessive inflation may also induce additional flow separation.

Longitudinal pitching moments (measured about the leading edge) are given as a function of lift for the three baseline designs in Figure 5-14. Of the three, the PR wing is not statically

stable (based upon a negative $C_{m,AC}$), and the hinged trailing edge portion (seen in Figure 1-1 and Figure 1-2) must be used for trimmed flight. Prior to stall, both the aeroelastic model and the experiment indicate very similar behavior between the rigid and the BR wing, with mild nonlinearities in the moment curves. This is ostensibly due to tip vortex growth, as before [3].

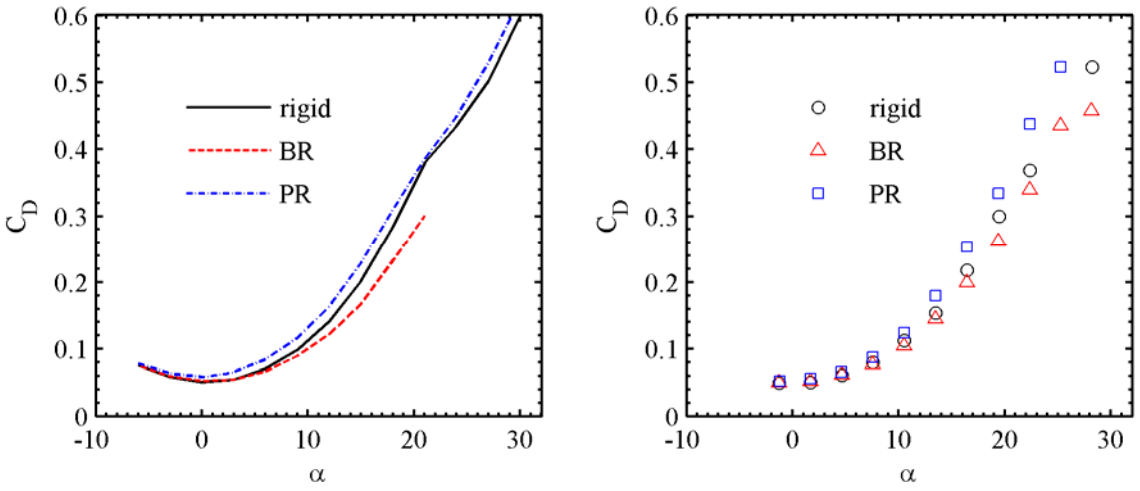

Figure 5-13. Baseline drag coefficients: numerical (left), experimental (right).

The PR wing has a 15% lower pitching moment slope than the rigid wing. This is a result of the membrane inflation, which shifts the pressure recovery towards the trailing edge, adaptively increasing the strength of the nose-down (restoring) pitching moment with increases in lift and α. Steeper C_m slopes indicate larger static margins: stability concerns are a primary target of design improvement from one generation of micro air vehicles to the next. The static margin of a MAV is generally only a few millimeters long; properly fitting all the micro-components on board can be difficult. Furthermore, the PR wing displays a greater range of linear C_m behavior, possibly due to the fact that the adaptive membrane inflation quells the strength of the low pressure cells [13].

Finally, L/D characteristics are given in Figure 5-15, as a function of lift. For low angles of attack (and lift), the three wings perform similarly. At higher angles of attack (prior to stall), the PR wing has the highest efficiency. The model incorrectly computes the BR wing to have

the best L/D for a small range of modest lift values. Correlation between model and experiment is generally acceptable for the rigid and BR wings, though the L/D of the PR wing is significantly under-predicted by the model, owing mostly to poor lift prediction at these angles (Figure 5-12). The camber of the PR wing is subsequently under-predicted as well (Figure 5-11), and may be a result of membrane vibration [89]. At no point does either model or experiment indicate that the rigid wing has the best efficiency; perhaps surprising, given the fact that neither wing deforms into a particularly optimal airfoil shape.

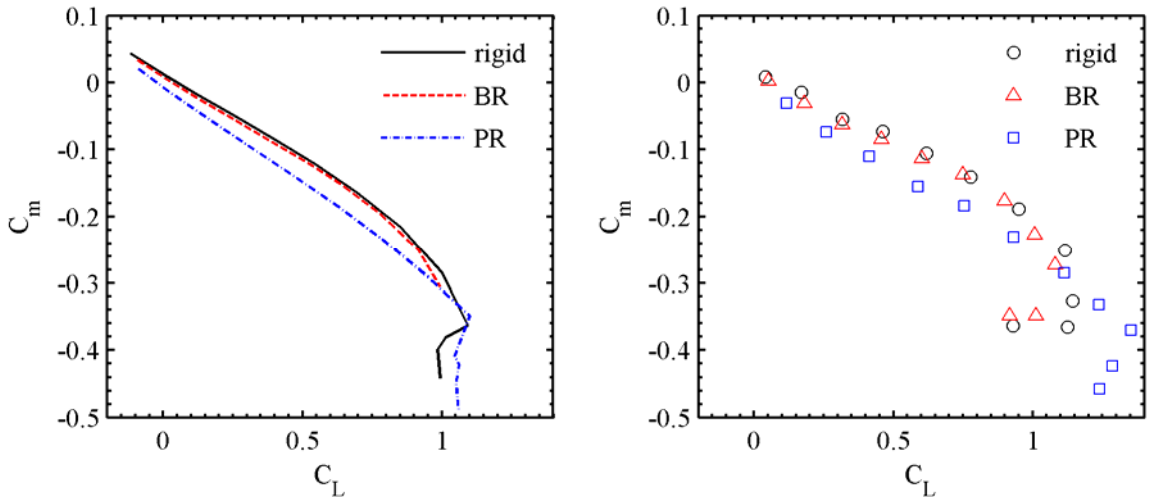

Figure 5-14. Baseline pitching moment coefficients: numerical (left), experimental (right).

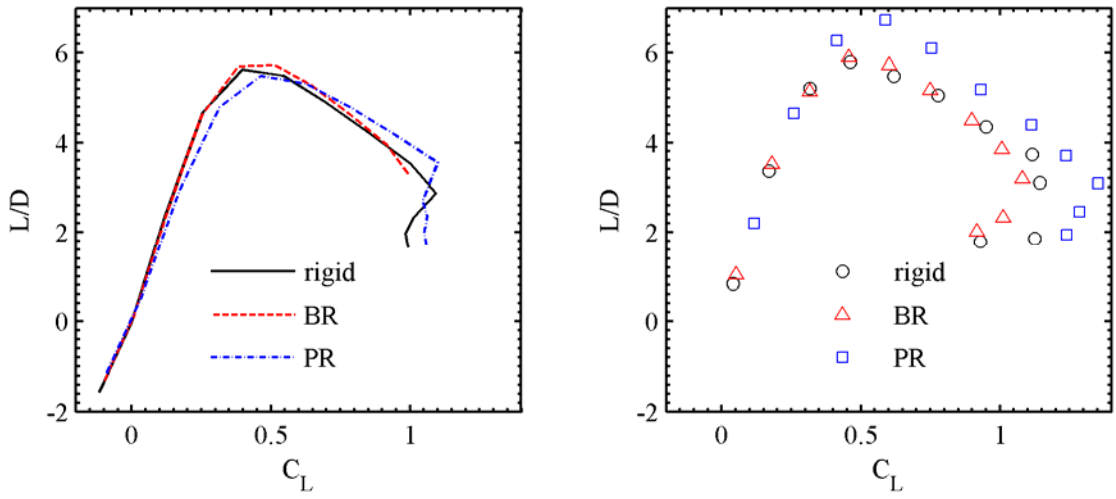

Figure 5-15. Baseline wing efficiency: numerical (left), experimental (right).

A quantitative summary of the last four figures is given in Table 5-1, for all three baseline wings at 6º angle of attack. Experimental error bounds are computed as described above. Aerodynamic sensitivities (as well as the pitching moment about the aerodynamic center) are found with a linear fit through the pre-stall angles of attack. Error bounds in these slopes are computed with Monte Carlo simulations. Computed lift, drag, and pitching moments consistently fall within the measured error bars (the latter of which are exceptionally large), though pitching moments are significantly under-predicted (10-30%). Sensitivities are also under-predicted, though still fall within the large error bars associated with pitching moment slopes. With the exception of L/D of a PR wing, trends between different wing structures are well-predicted by the aeroelastic model.

Table 5-1. Measured and computed aerodynamic characteristics, $\alpha = 6º$.

	C_L			C_D		
	num.	exp.	error (%)	num.	exp.	error (%)
rigid	0.396	0.384 ± 0.024	3.10	0.070	0.069 ± 0.007	1.15
BR	0.381	0.382 ± 0.024	-0.16	0.067	0.069 ± 0.007	-3.04
PR	0.465	0.495 ± 0.031	-5.98	0.085	0.076 ± 0.009	11.61
	C_m			L/D		
	num.	exp.	error (%)	num.	exp.	error (%)
rigid	-0.084	-0.063 ± 0.033	-32.81	5.64	5.49 ± 0.69	2.72
BR	-0.087	-0.073 ± 0.034	-19.39	5.70	5.49 ± 0.68	3.77
PR	-0.138	-0.131 ± 0.042	-5.64	5.49	6.49 ± 0.87	-15.36
	$C_{L\alpha}$			$C_{m,AC}$		
	num.	exp.	error (%)	num.	exp.	error (%)
rigid	0.049	0.051 ± 0.003	-5.26	0.013	0.016 ± 0.018	-
BR	0.044	0.048 ± 0.004	-9.35	0.006	-0.001 ± 0.020	-
PR	0.052	0.057 ± 0.004	-9.21	-0.008	-0.015 ± 0.026	-
	$C_{m\alpha}$			dC_m/dC_L		
	num.	exp.	error (%)	num.	exp.	error (%)
rigid	-0.012	-0.010 ± 0.004	-11.65	-0.246	-0.199 ± 0.086	-23.07
BR	-0.011	-0.009 ± 0.004	-17.97	-0.244	-0.185 ± 0.098	-31.88
PR	-0.014	-0.013 ± 0.006	6.01	-0.280	-0.229 ± 0.105	-22.17

Flow Structures

Having established sufficient confidence in the static aeroelastic membrane wing model,

attention is now turned to the computed flow structures. No experimental validation is available for this work, though whenever possible the results will be correlated to data in the previous two sections, or results in the literature. Experimental flow visualization work for low aspect ratios and low Reynolds number is given by Tang and Zhu [6] and Kaplan et al. [37]. Work done explicitly on MAV wings is given by Gursul et al. [40], Parks [91], Gamble and Reeder [92], and Systma [153].

The pressure distributions and flow structures are given in Figure 5-16 at 0° angle of attack for the upper/suction wing surface of all three baseline wing designs. The plotted streamlines reside close to the surface, typically within the boundary layer. For the rigid wing, a high pressure region is located close to the leading edge, corresponding to flow stagnation. This is followed by pressure recovery (minimum pressure), located approximately at the camber of each rigid wing section. Pressure recovery is followed by a mild adverse pressure gradient, which is not strong enough to cause the flow to separate. A further decrease in Reynolds number has been shown to cause mild flow separation over the top surface for 0° however [14], [153]. A small locus of downward forces are present over the negatively-cambered region (reflex) of the airfoil, helping to offset the nose-down pitching moment of the remainder of the rigid MAV wing, as discussed above. The reflex can also help improve the wing efficiency, compared to positively-cambered wings [55]. There is positive lift of this wing at 0° (Figure 5-12), resulting in a mild tip vortex swirling system. The low pressure cells at the wing tip are not yet evident.

Aeroelastic pressure redistributions of the upper surface of the BR wing are seen in the form of three high-pressure lobes at the carbon fiber/membrane boundary interface towards the leading edge. The membrane inflation in between each batten (Figure 5-1) results in a slight tangent discontinuity in the wing surface. This forces the flow to slow down and redirect itself

over the inflated shape: such a deceleration results in a pressure spike. Aft of these spikes, the pressure is slightly lower in the membrane skin than over each batten (due to the adaptive camber), driving the flow into the membrane patches. This is a very small effect (mildly visible in the streamlines) for the current case, but can be expected to play a large role with potential flow separation, where the chordwise velocities are very small [154].

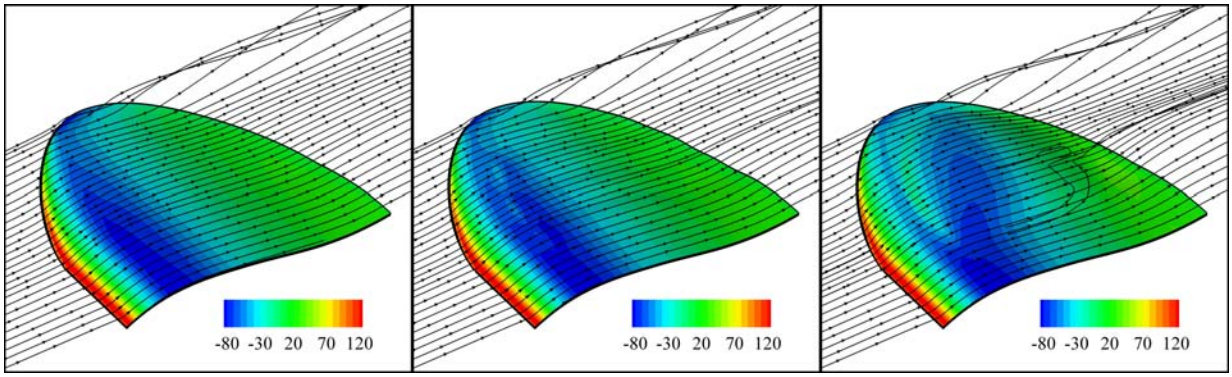

Figure 5-16. Pressure distributions (Pa) and streamlines on the upper surface of a rigid (left), BR (center), and PR wing (right), $\alpha = 0^{o}$.

For the PR wing (Figure 5-16), the pressure spike is stronger, and exists continuously along the membrane interface. A significant percentage of this spike is directed axially, increasing the drag (as seen in Figure 5-13). The adaptive inflation causes an aft-ward shift in the pressure recovery location of each flexible wing section. The longer moment arm increases the nose-down pitching moment about the leading edge (Figure 5-14), which is the working mechanism behind the benevolent longitudinal static stability properties of the PR wing. Furthermore, the aerodynamic twist increases the adverse pressure gradient over the membrane portion of the wing: some flow now separates as it travels down the inflated shape, further increasing the drag (as compared to the rigid wing).

Similar results are given for the lower/pressure side of the three wings at 0^{o} angle of attack in Figure 5-17. The flow beneath the rigid wing is dominated by an adverse pressure gradient towards the leading edge, causing a large separation bubble underneath the wing camber. This

separated flow is largely confined to the in-board portions of the wing. Flow reattaches slightly aft of the quarter-chord, after which the pressure gradient is favorable. The flow accelerates beneath the negatively-cambered portion of the rigid wing: this decreases the local pressures, further offsetting the nose-down pitching moment. The pressure distribution on the lower surface is not greatly affected by the tip vortices, previously noted by Lian et al. [28].

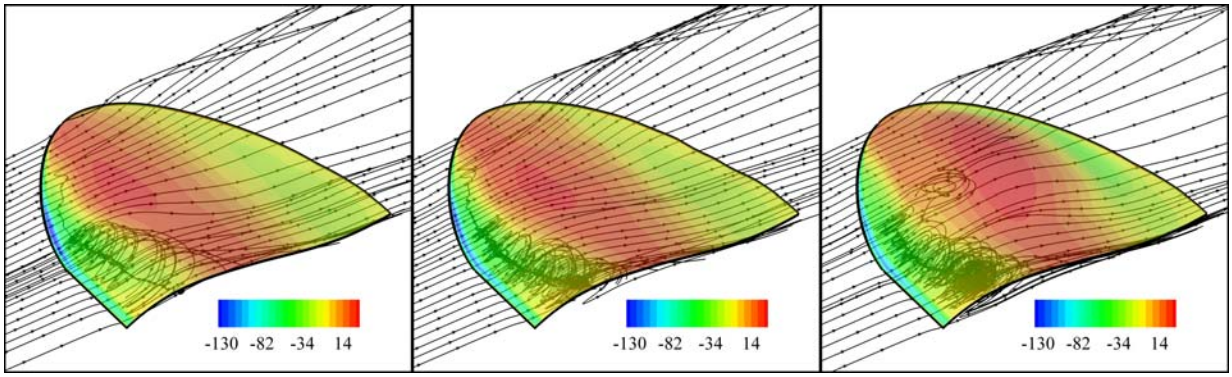

Figure 5-17. Pressure distributions (Pa) and streamlines on the lower surface of a rigid (left), BR (center), and PR wing (right), $\alpha = 0^{\circ}$.

For the BR wing (Figure 5-17), slight undulations in the pressure distribution are indicative of the membrane inflation in between the battens. This causes the opposite of what is seen on the upper wing: flow is slightly packed towards the battens [154], though the effect is minor, as before. The adaptive aerodynamic twist of the PR membrane wing pushes the bulk of the separated flow at the leading edge towards the root, and induces further separation beneath the inflated membrane shape, as the air flows into the cavity against an adverse pressure gradient. The location of maximum pressure is increased and pushed aft-ward to coincide with the apex of the inflated membrane, increasing both the lift and the stability.

Flow structures over the upper surface at 15º angle of attack are given in Figure 5-18. At this higher incidence, the adverse pressure gradient is too strong for the low Reynolds number flow, and a large separation bubble is present at the three-quarter chord mark of the rigid wing. Despite the nose-up geometric twist built into the wing (7º at the tip, Figure 5-9), flow separates

at the root first, and is confined (at this angle) to the in-board portion of the wing. This may be due to the steeper pressure gradients at the root, or an interaction with the tip vortex system [5].

The reattached flow aft of the bubble (and the resulting pressure distribution) must be viewed with a certain amount of suspicion. Such a reattachment is known to be turbulent process [25], and no such module is included in the CFD (or even, to the author's knowledge, exists for complex three-dimensional flows). Unsteady vortex shedding may accompany the bubble as well [8], though time-averaging of vortex shedding is known to compare well with steady measurements of a single stationary bubble [18]. The augmented incidence has considerably increased the strength of the wing-tip vortex swirling system over the rigid wing. The size of the vortex core is larger (indicative of the expected increase in induced drag [27]), and the low pressure cells at the wing tip are very evident [3].

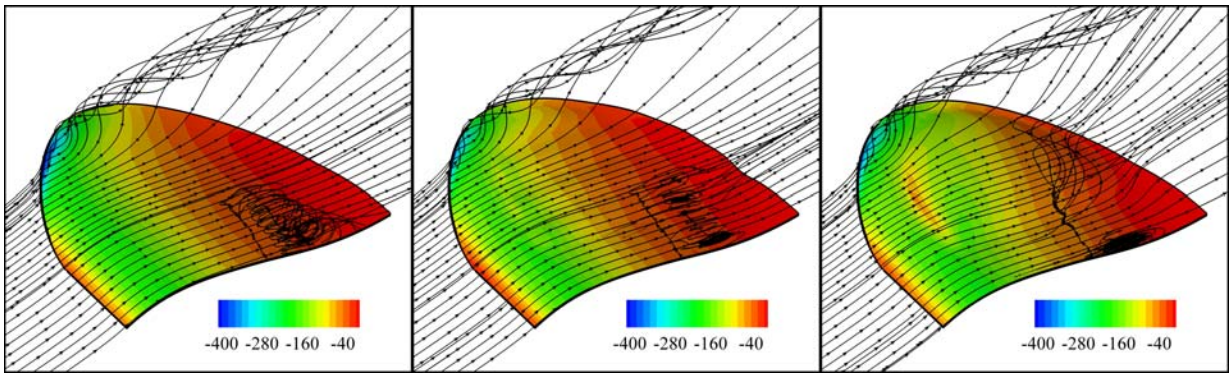

Figure 5-18. Pressure distributions (Pa) and streamlines on the upper surface of a rigid (left), BR (center), and PR wing (right), $\alpha = 15^{\circ}$.

As expected, the aeroelastic effects of the BR and PR wings are more predominate at 15º in Figure 5-18. For the BR wing, the three high-pressure lobes over the membrane/carbon fiber interface are larger. Significant pressure-redistribution over the membrane stretched between the outer batten and the wing tip can be seen as well. Adaptive washout slightly decreases the intensity of the separation bubble, but has no noticeable effect on the pressure distribution at the trailing edge of the upper BR wing surface. At 15º, the aerodynamic twist of the PR wing is

considerably larger than before, as is the resulting pressure spike at the membrane-carbon fiber interface. Despite the large adverse pressure gradient in this region, flow does not separate (though it has been noted in other studies [153]).

The inflated membrane shape of the PR wing pushes the bulk of the flow separation closer to the wing root. Some of this separated flow reattaches to the wing and travels into the wake, while the rest travels spanwise. This flow is attracted either by the low pressures associated with the adaptive cambering, or by the low pressures at the core of the tip vortex. Some of these separated streamlines are entrained into the swirling system, an interaction that has been shown to cause potential bilateral instabilities for high angles of attack [6]. This effect, not seen in the rigid or BR wings, obviously cannot be further studied in this work, due to both the symmetry and the steady assumptions made in the solver.

It can also be seen that the passive shape adaptation decreases the magnitude of the low pressure cells at the wing-tip, by 9% for the BR wing and 13% for the PR wing, compared to the rigid case. This indicates that the induced drag is decreased with flexibility, though this is only a re-distribution of the total drag. Two possible explanations exist for the decrease in tip vortex strength. The mechanical strain energy in the inflated membrane skin may be removing energy from the vortex swirling system [90]. For the PR wing, the inflated membrane shape may act as a barrier to the tip vortex formation, preventing the full swirling development at the wing-tip.

A similar effect is demonstrated in the work of Viieru et al. [38] by the use of endplates installed on a rigid MAV wing. Whereas the endplates are able to decrease induced drag only at moderate angles (afterwards the tip vortices increase in strength to overwhelm the geometrical presence of the endplates), the phenomena demonstrated in Figure 5-18 is effective at all angles: both the size of the membrane barrier and the strength of the vortex swirling grow in conjunction

with one another as the angle of attack increases. This decrease in tip vortex strength is also seen in Figure 5-14: the nonlinear aerodynamics (from the low pressure cells at the tip) is evident in the pitching moments of the rigid and BR wings, while the PR curve is very linear.

On the underside of the rigid wing at 15º angle of attack (Figure 5-19), the increased incidence provides for completely attached flow behavior. The pressure gradient is largely favorable, smoothly accelerating the flow from leading to trailing edge. From the previous four figures it can be seen that separated flow over the bottom surface gradually attaches for increasing angles of attack, while attached flow over the upper surface gradually separates (eventually leading to wing stall). As time-averaged flow separation is likely to be unsteady vortex shedding [18]: this explains the aforementioned membrane vibration amplitudes that decrease to a quasi-static behavior, then increase through the α-sweep [135].

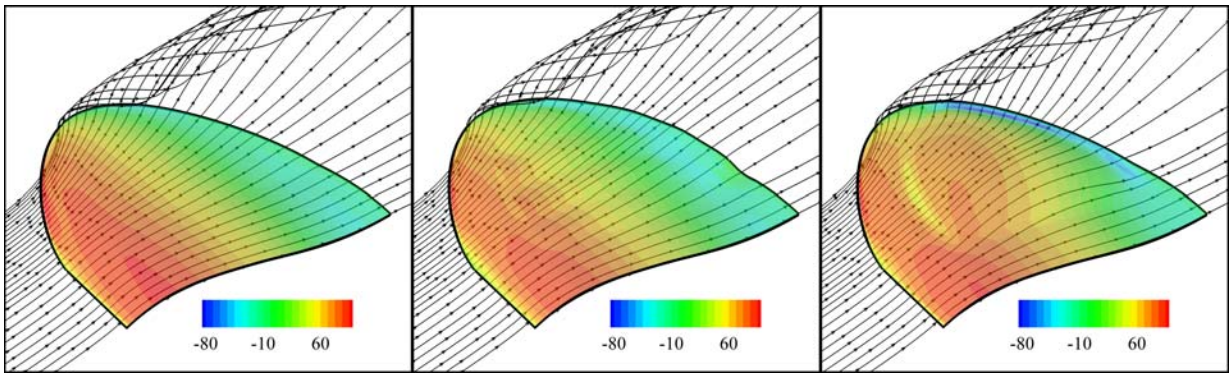

Figure 5-19. Pressure distributions (Pa) and streamlines on the lower surface of a rigid (left), BR (center), and PR wing (right), α = 15º.

Load alleviation on the lower surface of the BR wing is evidenced by a decrease in the high-pressure regions associated with camber, and a growth of the suction region at the trailing edge (the latter presumably due to a decrease in the local incidence). A high-pressure lobe also develops at the trailing edge of the membrane panel between the carbon fiber root and the inner batten. At higher angles, this region of the membrane does not locally inflate; it merely stretches between the two laminates, acting as a hinge. The adaptive inflation of the PR wing causes a

significant redirection of the flow vectors beneath the wing, but does not induce flow separation. Two sharp pressure drops are seen beneath the wing: one as the flow accelerates into the inflated membrane shape, and the second as the flow accelerates out of from the membrane and underneath the re-curved area of the wing.

Further delineation of the flow structures over the three baseline wings can be seen in Figure 5-20 ($\alpha = 0^{o}$) and Figure 5-21 ($\alpha = 15^{o}$), with the sectional normal force coefficient and the pressure coefficients over a flexible span station ($2y/b = 0.5$) of the wing. For the rigid wing at 0^{o}, the sectional normal force peaks at $2y/b = 0.9$ (due to the decreasing local chord length of the Zimmerman planform, but also the low pressure cells left by the tip vortices) and then experiences a sharp drop at the tip, as necessitated by the low thickness of the wing. Grid resolution and errors from interpolating the pressures from the cell centers to the nodes [150] prevent this curve from reaching the correct value of zero. No significant differences arise between the computed c_n of the BR and rigid wings at 0^{o}, as previously indicated by the similar aerodynamic loads (Figure 5-12). The adaptive inflation of the PR wing increases the normal force over most of the wing, including the stiff carbon fiber root.

Turning now to the pressure coefficients at 0^{o} (Figure 5-20), both the BR and the PR wings experience a pressure spike over the upper surface at $2y/b = 0.2$, corresponding to the membrane inflation. Outside of this location, pressure redistribution over the BR wing is negligible. The PR wing shows an aft-ward shift in the high-lift forces over both the upper and lower surfaces. Adaptive inflation is also seen to increase the severity of the adverse pressure gradient (leading to the flow separation seen in Figure 5-16), and exacerbate the pressure gradient reversal over the reflex portion of the wing.

At 15^{o} angle of attack (Figure 5-21), the BR wing is more effective, able to alleviate the

load over the majority of the wing. An evaluation of the pressure coefficients at this angle indicates that the majority of this reduction in lift occurs towards the trailing edge of the bottom surface, where the suction forces are increased. Both flexible wing pressure spikes over the upper surface are intensified at the higher angle, with the PR wing's approaching the strength of the leading edge stagnation pressure. Sharp pressure drops are also visible on the underside of the wing, as the flow accelerates into the membrane cavity. All three wings show a mild pressure plateau associated with separation [27]; the plateaus of the flexible wings are shifted towards the trailing edge.

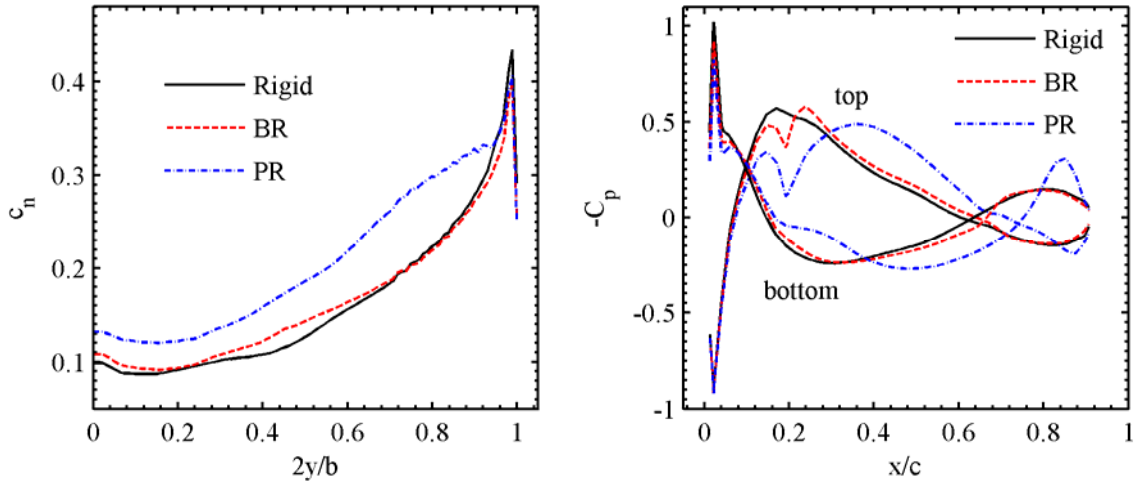

Figure 5-20. Section normal force coefficients, and pressure coefficients (2y/b =0.5), α = 0°.

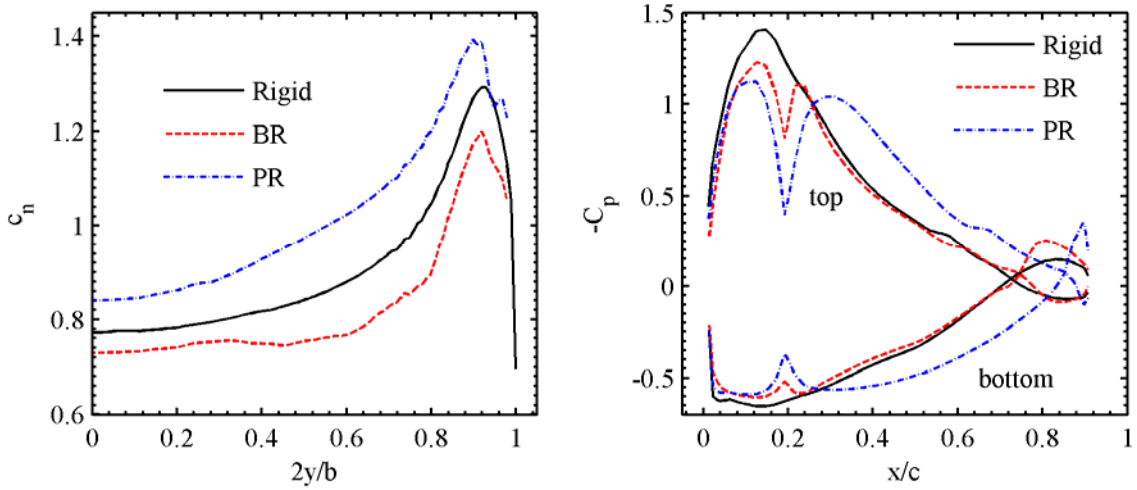

Figure 5-21. Section normal force coefficients, and pressure coefficients (2y/b =0.5), α = 15°.

CHAPTER 6
AEROELASTIC TAILORING

The static aeroelastic modeling algorithm detailed above (using the Navier-Stokes flow solver and the nonlinear membrane solver) can elucidate accurate quantitative dependencies of a variety of parameters (C_L, C_D, C_m, L/D, $C_{L\alpha}$, $C_{m\alpha}$, mass) upon the wing structure. Having first studied the general effect of wing topology (batten-reinforced and perimeter-reinforced membranes, as well as rigid wings), attention is now turned to structural sizing/strength variables within the BR and PR wings. Results from the previous section show that the membrane skin's inflation/stretching dominates the aeroelastic behavior, indicating the importance of the pre-tension in the membrane skin. Pre-stress resultants in the spanwise and chordwise directions are both considered as variables. With the exception of the free trailing edge correction of the BR wings detailed above, the pre-tension is constant throughout the wing. The laminate orientation and number of plies used to construct the plain weave carbon fiber areas of the wing can be varied as well. Finally, the number of layers in each batten of the BR wing can be altered, though the orientation will be fixed so that the fibers run parallel to the chord line.

The sizing/strength parameters listed above leads to an optimization framework with 9 variables, if the number of layers in each of the three battens are permitted to differ, and the wing type (BR, PR, rigid) is considered a variable as well. Some of the variables are discrete, others continuous. The variables are not entirely independent either: the fiber orientation of the second bi-directional plain weave ply is meaningless if only a single ply is used. Genetic algorithms are well-suited to problems with a mixed integer-continuous formulation, can handle laminate stacking sequence designs without a set number of layers (with the use of addition and deletion modules [155]), are a cost-effective method of solving multi-objective problems [156], and can navigate disjointed design spaces [52]. The computational cost of a genetic algorithm is

prohibitive however, typically requiring thousands of function evaluations for suitable convergence; a single simulation using the static aeroelastic model described above takes 2-3 hours of processor time on a Compaq Alpha workstation.

A viable alternative is a designed experiment: the computational cost is lower, and provides an effective investigation of the design space. For this work, one-factor-at-a-time (OFAT) numerical tests are run to establish the effect of various structural parameters upon the relevant aerodynamics. The three baseline wing designs used above will represent the nominal wing designs (2 layers of plain weave at 45º, one layer battens, slack membrane). Having identified the structural variables that display the greatest sensitivity within the system, a full-factorial designed experiment [157] will be run on a reduced set of variables. This data set can then be used to identify the optimal wing type and structural composition for a given objective function. Designs that strike a compromise between two objective functions are considered as well. The work concludes with experimental wind tunnel validation of the performance of selected optimal designs.

OFAT Simulations

The schedule of OFAT simulations is as follows: a 6-level full factorial design is conducted for the chordwise and spanwise pre-stress resultants, 6 simulations for the orientation of a single laminate of plain-weave, a 6-level full factorial design for the orientations of a two-layer laminate plain weave, and a 3-level full factorial design for the number of layers used in the three battens. Pre-stress resultants are bounded by 0 N/m (slack membrane) and 25 N/m (axial batten buckling can be computed for a distributed axial force equivalent to 31 N/m of pre-stress resultant in the membrane). The latter value corresponds to roughly 10% pre-strain. Plies of plain weave carbon fiber are limited to two layers, while battens are limited to three.

Membrane Pre-Tension

Computed aerodynamic derivatives ($C_{L\alpha}$ and $C_{m\alpha}$) and efficiency (L/D) are given as a function of the pre-stress resultants in the chordwise (N_x) and spanwise (N_y) directions for a BR wing in Figure 6-1. The corresponding normalized wing displacement is given in Figure 6-2 for a subset of the data matrix. All results are computed at 12º angle of attack, aerodynamic derivatives are computed with a finite difference between 11º and 12º. In a global sense, increasing the pre-tension in the BR wing increases $C_{L\alpha}$, decreases $C_{m\alpha}$, and decreases L/D. The increased membrane stiffness prevents effective adaptive washout (and the concomitant load alleviation), and the wing performance tends towards that of a rigid wing. At 12º for a rigid wing, $C_{L\alpha} = 0.0507$, $C_{m\alpha} = -.0143$, and L/D = 4.908. Overall sensitivity of the aerodynamics to the membrane pre-tension can be large for the derivatives (up to 20%), though less so for the wing efficiency (less than 5%, presumably due to the conflictive nature of the ratio).

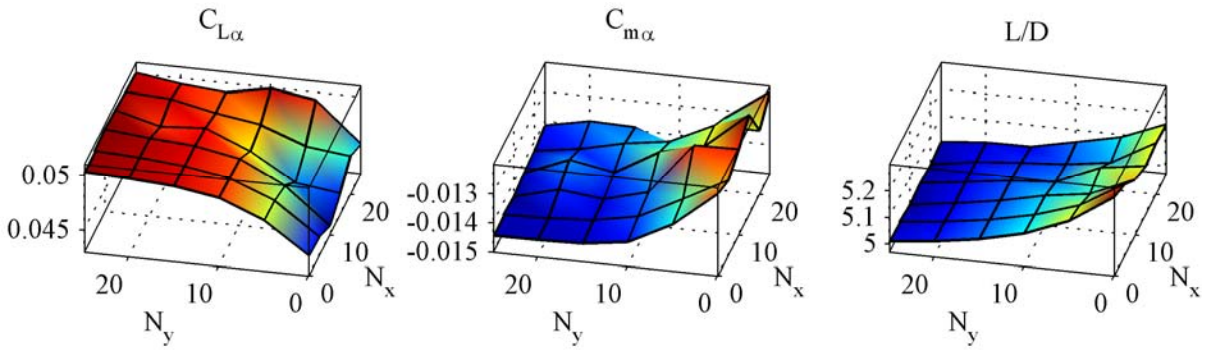

Figure 6-1. Computed tailoring of pre-stress resultants (N/m) in a BR wing, α = 12º.

The BR wing is very sensitive to the pre-stress in the spanwise direction, but less so to stiffness in the chordwise direction. This is seen in Figure 6-2: the slack membrane wing has a trailing edge deflection of 2.5% of the root chord. Maximizing the spanwise pre-tension (with the other direction slack) drops this value to 1%, while the opposite scenario drops the value to only 1.9%. This is due to the directional stiffness of the battens (which depend on compliance

normal to their axis for movement), but also the trailing edge stress correction detailed above.

Despite the global trend towards a rigid wing with increased pre-tension, the changes are not monotonic. A wing design with a minimum lift slope (for gust rejection, improved stall performance, etc.) is found, not with a completely slack wing, but a wing with a mild amount of stiffness (10 N/m) in the chord direction, and none in the span direction. Such a tactic removes the aforementioned conflicting sources of aeroelastic lift in a BR wing. The pre-stress correction eliminates most of the stiffness at the trailing edge (allowing for adaptive washout and load alleviation), but retains the chordwise stiffness towards the leading edge, as seen in Figure 4-8. The membrane inflation in this area is thus decreased, along with the corresponding increase in lift due to camber.

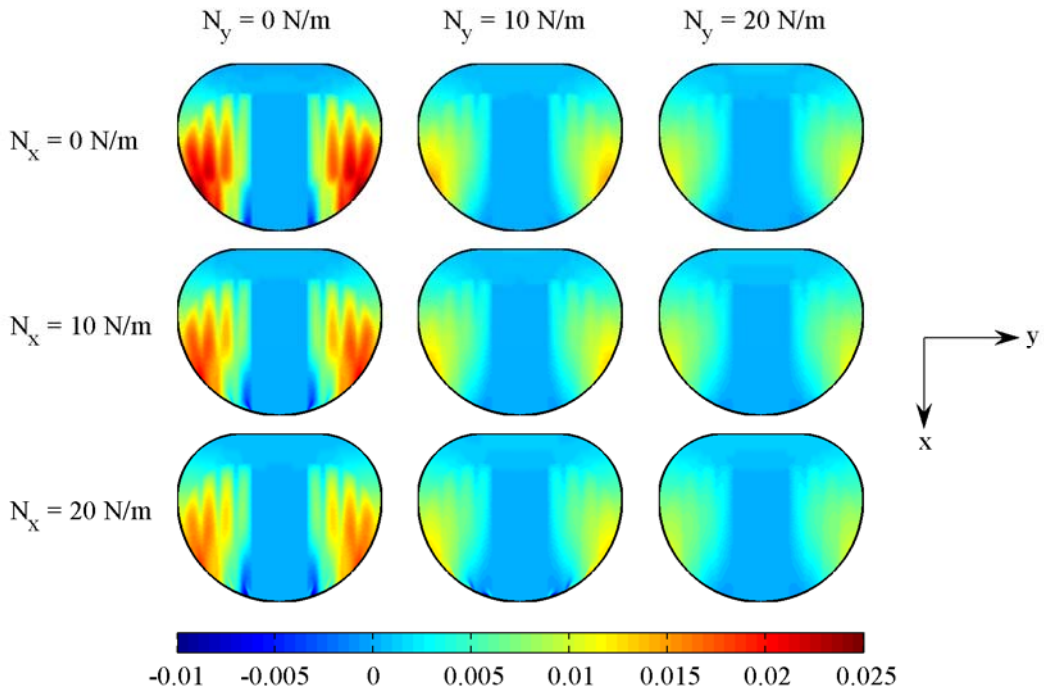

Figure 6-2. Computed BR wing deformation (w/c) with various pre-tensions, α = 12º.

Maximizing $C_{L\alpha}$ (for efficient pull-up maneuvers, for example), is found by maximizing N_y and setting N_x to zero; this eliminates the adaptive washout, but retains the inflation towards the leading edge. Conversely, maximizing $C_{L\alpha}$ with a constraint on the acceptable L/D might be

obtained by maximizing N_x and setting N_y to zero. Peak efficiency is found with a slack membrane: this corresponds to minimum drag, which is not shown. It should be mentioned however, that if a design goal is to maximize the lift slope (or minimize the pitching moment slope for stability), a BR wing is most likely a poor choice.

Opposite trends are found for the PR wing (Figure 6-3 and Figure 6-4): increasing the pre-tension decreases $C_{L\alpha}$, increases $C_{m\alpha}$, and increases L/D. Similar to before, added wing stiffness decreases the adaptive inflation of the wing skin, and results tend towards that of a rigid wing. Without the directional influence of the battens and the trailing edge stress correction needed for the BR wing, the PR wing surfaces in Figure 6-3 are very smooth, and converge monotonically for high pre-stress.

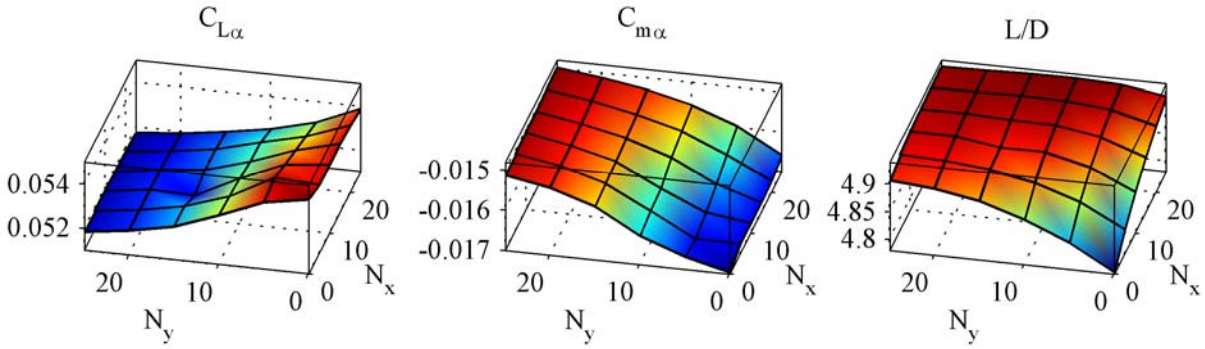

Figure 6-3. Computed tailoring of pre-stress resultants (N/m) in a PR wing, $\alpha = 12^{\circ}$.

As before, the PR wing is more sensitive to pre-tension in the spanwise direction than the chordwise direction. The slack membrane wing inflates to 5% of the chord: maximizing tension in the chord direction (with none in the span direction) drops this value to 3%, though the opposite case drops the value to 1.5%. This is probably due to the fact that the chord of the membrane skin is about twice as long as it's span. The sensitivity of a pressurized rectangular membrane to a directional pre-stress is inversely-proportional to its length in the same direction, as indicated by solutions to Eq. (4-4). Though the L/D of the PR wing is equally affected by pre-

stresses in both directions, the two aerodynamic derivatives in Figure 6-3 have a significantly muted response to N_x. Such a result has noteworthy ramifications upon a multi-objective optimization scenario. The longitudinal static stability is optimal for a slack membrane wing, but the wing efficiency at this data point is poor. Maximizing N_x and setting N_y to zero greatly improves the lift-to-drag ratio (only 0.2% less than the true optimum found on this surface), with a negligible loss in static stability.

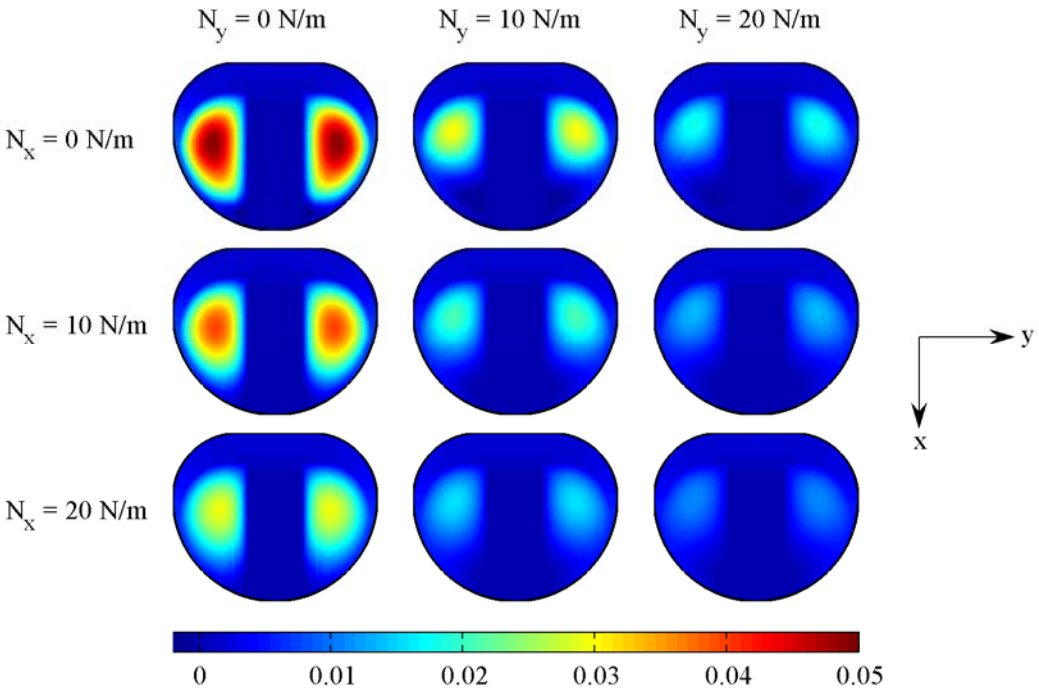

Figure 6-4. Computed PR wing deformation (w/c) with various pre-tensions, $\alpha = 12^{\circ}$.

Single Ply Laminates

The same aerodynamic metrics are given in Figure 6-5 as a function of the ply angle (with respect to the chord line) for a set of wings with a single layer of bi-directional carbon fiber at the wing root, leading edge, and perimeter (for the PR wing only). The membrane wing is slack. Due to the plain weave nature of the laminate, all trends are periodic every 90º. Only fiber orientations of 0º, 45º, and 90º automatically satisfy the balance constraint [155]. For the PR wing, changing the fiber angle has a minor effect on the aeroelastic response, and optima are

mostly located at either 45º (where spanwise bending is largest) or 90º (where it is smallest). This indicates that the PR wing, whose planform is dominated by membrane skin, can only take advantage of different laminates inasmuch as the spanwise bending can increase or decrease the aerodynamic membrane twist/cambering.

On the other hand, the BR wing relies mostly upon geometric twist (Figure 5-11), which can be provided from unbalanced laminates via bend-twist coupling; the concept behind traditional aeroelastic tailoring [11]. Of the 7 data points shown in Figure 6-5, orientations less than 45° cause the wing to wash-in, while angles greater than 45° cause washout, the latter of which minimizes $C_{L\alpha}$ of a BR wing, as expected. Using laminate wash-in to counter the load alleviation of the membrane washout (at 15°) optimizes the wing efficiency. Aerodynamic sensitivity of the BR wing to laminate orientation is also larger than that seen in the PR wing because the carbon fiber skeleton is less constrained. The wing tip of the BR wing (where the forces can be large, due to the tip vortices seen in Figure 5-18) is not connected to the trailing edge via a perimeter strip.

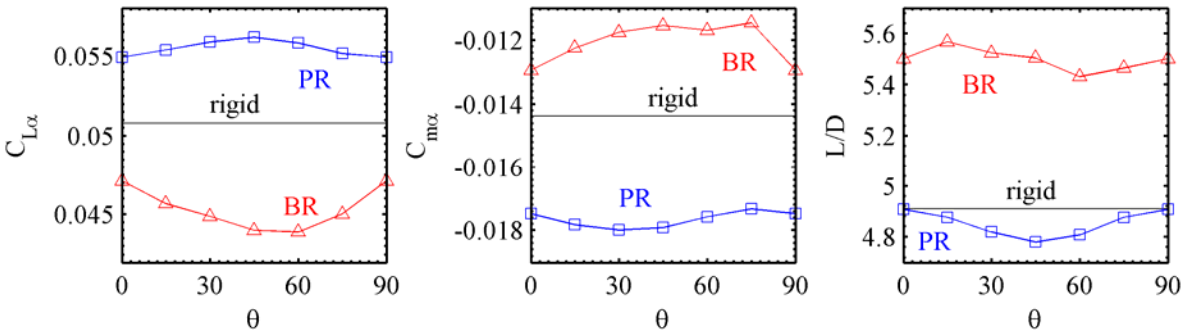

Figure 6-5. Computed tailoring of laminate orientation for single ply bi-directional carbon fiber, α = 12º.

Double Ply Laminates

Computed aerodynamic derivatives ($C_{L\alpha}$ and $C_{m\alpha}$) and efficiency (L/D) are given as a function of the ply orientations (θ_1 and θ_2) of the two layers of bi-directional plain weave in a BR

wing (Figure 6-6) and a PR wing (Figure 6-7) at 12° angle of attack. As before, the membrane skin is slack. Aeroelastic trends are expected to repeat every 90°, and will be symmetric about the line $\theta_1 = \theta_2$. This latter point is only true because bending-extension coupling in non-symmetric laminates is ignored, though the effect of its inclusion would be very small as the wing is subjected mostly to normal pressure forces.

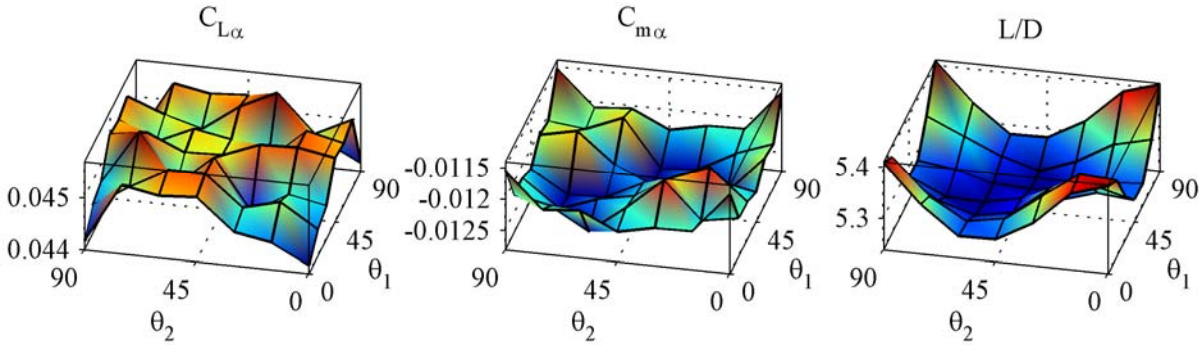

Figure 6-6. Computed tailoring of laminate orientations for two plies of bi-directional carbon fiber in a BR wing, $\alpha = 12°$.

For the BR wing, efficiency is maximized and the lift slope is minimized when the fibers make 45° angles with the chord and span directions. Static stability is improved when fibers align with the chord. The response surface of the two stability derivatives are very noisy, suggesting possible finite differencing errors, and all three surfaces in Figure 6-6 show little variation (only $C_{m\alpha}$ of the BR wing can be varied by more than 5%). Unlike any of the tailoring studies discussed above, the PR wing shows the same overall trends and optima as the BR wing. The surfaces for the PR wing, however, are much smoother but have less overall variation.

Of the sampled laminate designs, $[15°]_2$ and $[75°]_2$ will exhibit the greatest bend-twist coupling, yet neither are utilized by the membrane wings. This fact, along with the similarity between the PR and the BR surfaces, suggest that the orientation of a plain weave laminate with two layers is too stiff to have much impact on the aerodynamics, which is dominated by membrane inflation/stretching. The use of bi-directional plain weave is not the most effective

means of introducing bend-twist coupling in a laminate. The fact that the two fiber directions within the weave are perpendicular automatically satisfies the balance constraint at angles such as 45°. This would not be the case if plies of uni-directional carbon fiber are utilized, but this is prohibitive in MAV fabrication for the following reason. Curved, unbalanced, potentially non-symmetric thin uni-directional laminates can experience severe thermal warpage when removed from the tooling board, retaining little of the intended shape.

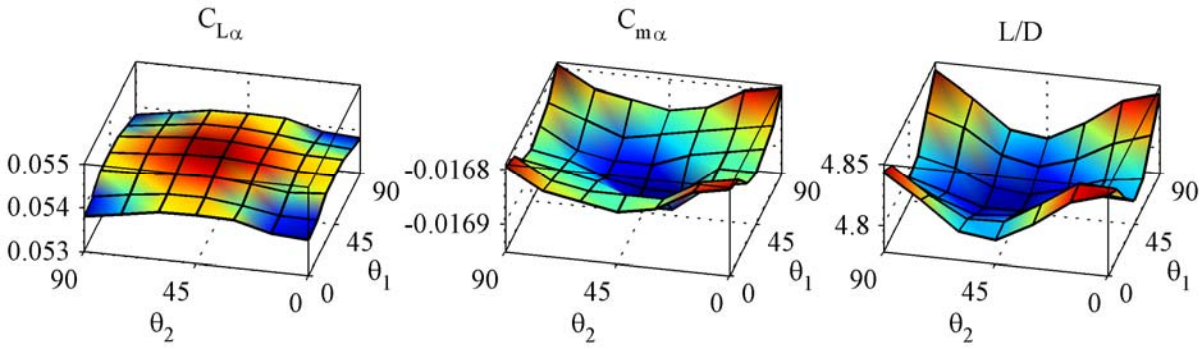

Figure 6-7. Computed tailoring of laminate orientations for two plies of bi-directional carbon fiber in a PR wing, $\alpha = 12^{\circ}$.

Batten Construction

Computed lift slope and efficiency of a BR wing at 12º angle of attack is given in Figure 6-8 as a function of the number of layers in each batten. The thickness of each batten can be varied independently, though the number of layers is limited to three, resulting in 27 possible designs. As before, the membrane skin is slack, and a two-layer plain weave at 45º makes up the remainder of the wing. The normalized out-of-plane displacement and differential pressure coefficients along the chord-station x/c = 0.5 for 4 selected designs is given in Figure 6-9.

As expected, the wing with three one-layer battens has the most adaptive washout, which provides the shallowest lift slope, but also the best lift-to-drag ratio. Additional plies, regardless of which batten they are added to, monotonically decreases the efficiency. The same technique can be used to increase $C_{L\alpha}$, except for combinations of stiff battens towards the wing root and a

thin outer batten at the wing tip (331 and 332, for example, where the battens are numbered from inner to outer and the integers indicate the number of layers), which can cause the lift slope to decrease from these peaks. Design 223 shows the steepest lift slope of the wings in Figure 6-8.

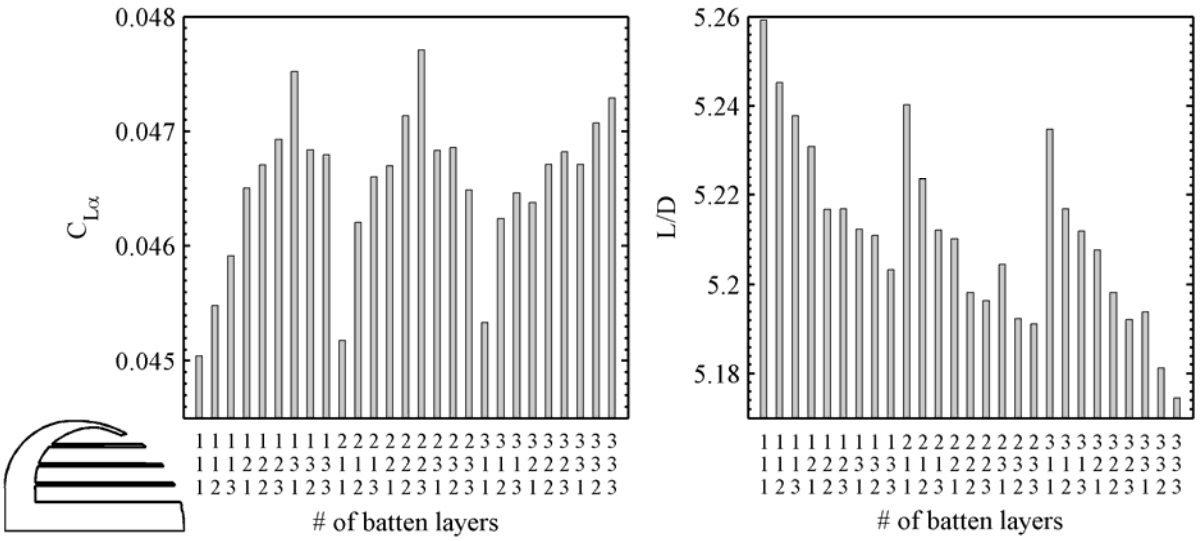

Figure 6-8. Computed tailoring of batten construction in a BR wing, α = 12º.

The undulations in the differential pressure due to local membrane inflation from in between the battens are clearly visible in Figure 6-9. Low pressure regions on the upper surface of the membrane skin and high pressure on the lower surface (which slightly re-directs the flow towards the battens [154]) results in the four high-lift lobes over the inflated membrane skin. This inflation can be controlled in obvious ways: wing displacement is larger for design 111 than design 333, throughout the entire length of the wing section in Figure 6-9. The wing deformation of design 123 is comparable to design 111 towards the root of the wing, but tapers off towards the wingtip, where it resembles design 333. In some cases, redistributing the batten sizes causes a trade-off between local inflation and spanwise bending. The displacement of design 123 is less than design 111 between 24% and 60% of the semispan, but the local inflation between the stiffer battens is higher, causing greater redistribution of the flow and high differential pressures. A similar comparison can be made between designs 321and 111 towards

the wingtip. Overall changes in the aerodynamics due to batten tailoring are relatively small however, with 5% possible variability in $C_{L\alpha}$ and 1.5% in L/D. Though not shown, the static stability of the BR wing can be varied by 10% with batten tailoring.

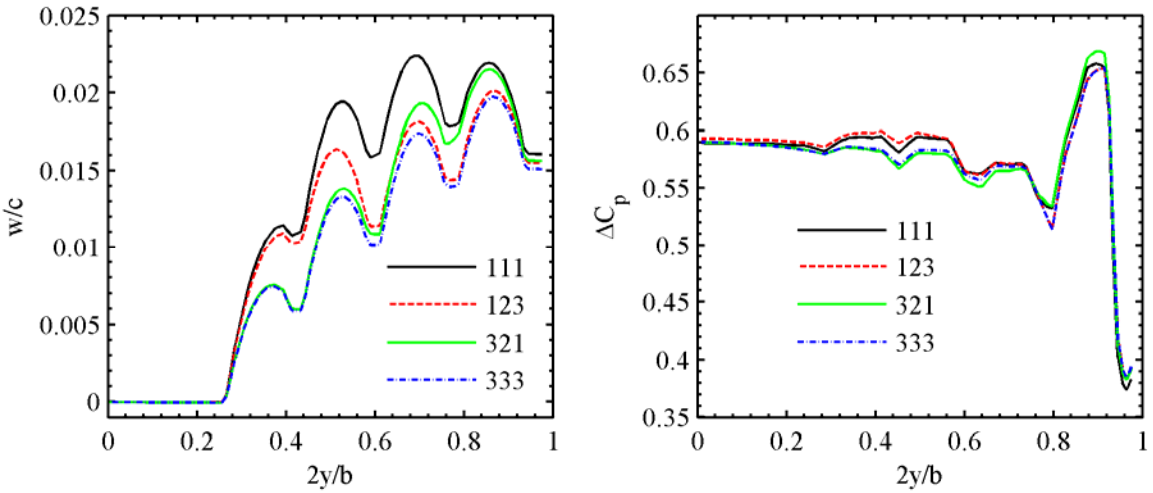

Figure 6-9. Computed normalized out-of-plane displacement (left) and differential pressure (right) at x/c = 0.5, for various BR designs, α = 12º.

Full Factorial Designed Experiment

Of the structural sizing/strength parameters discussed above, spanwise membrane pre-tension, chordwise pre-tension, the number of layers of bi-directional plain weave carbon fiber, and the wing type (BR, PR, rigid) are considered in a designed experiment. As stated above, the aeroelasticity of the MAV wing is dominated by the membrane inflation, and the laminate stacking is a secondary effect (though $C_{m\alpha}$ of a BR wing is moderately sensitive to fiber orientation and batten thickness). The number of layers of plain weave carbon fiber, though not explicitly discussed above, is included due to interesting discrepancies between laminate tailoring with one layer (Figure 6-5) and tailoring with two layers (Figure 6-6 and Figure 6-7). For this study, the number of layers in each batten is fixed at one, and all plain weaves are oriented at 45º to the chordline.

A three-level, three-variable full factorial designed experiment is implemented for each

membrane wing. Only 1, 2, or 3 layers of carbon fiber are permitted, while pre-tension resultant (chordwise or spanwise) is restricted to 0, 10 or 20 N/m. More than 3 layers is excessively stiff and heavy; 1 layer may not be able to withstand flight loads or survive a crash. The upper cap on pre-tension is, as discussed above, meant to prevent batten buckling. Each full factorial design array requires 27 simulations for each membrane wing, a number which must be doubled to obtain finite difference approximations of the lift and moment derivatives in angle of attack. Including the two data points needed for the rigid wing, 110 computationally expensive simulations are required. While a full factorial matrix is not the most economical choice for a designed experiment (a central-composite design is an adequate fraction of the full factorial, for example [157]), the uniform sampling will provide the best qualitative insight into the membrane wing tailoring.

All 27 data points for the BR wing are given in Figure 6-10, in terms of $C_{L\alpha}$, $C_{m\alpha}$, and L/D. The data points for a two-layer laminate are identical to those seen in Figure 6-1. The computed normalized out-of-plane displacement of the BR wing with a slack membrane can be seen in Figure 6-11, with one, two, and three layers of plain weave carbon fiber. These designs are the three found on the z-axis of Figure 6-10. The variability in the aerodynamics with the three design variables is substantial: 22% in the lift slope, 54% in the pitching moment slope, and 16% in efficiency. As above, increasing the pre-tension in the BR wing increases $C_{L\alpha}$, decreases $C_{m\alpha}$, and decreases L/D, though the trend is not monotonic. No prevalent trend exists for the number of plain weave layers, demonstrating strong interactions with the membrane pre-tension.

For a slack BR membrane wing ($N_x = N_y = 0$), increasing the number of plain weave layers significantly decreases the deformation of the wing tip and the adaptive washout at the trailing edge. As seen in Figure 6-11, a three-layer BR wing is mostly characterized my local membrane

inflation among the battens. This demonstrates the degree to which the adaptive washout at the trailing edge depends on the bending/twisting of the leading edge laminate (where the forces are very high, seen in Figure 5-18), and also explains why tailoring the thickness of the battens, discussed above, has only a minor effect upon the aerodynamics.

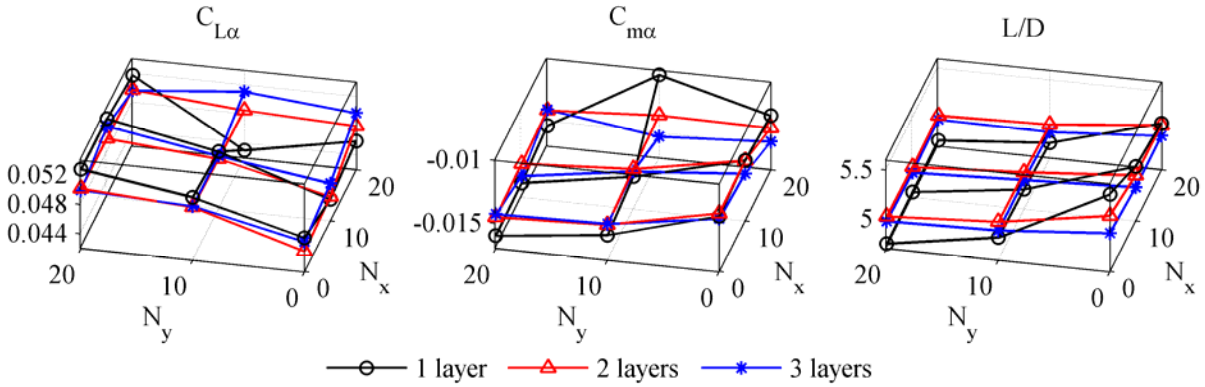

Figure 6-10. Computed full factorial design of a BR wing, α = 12º.

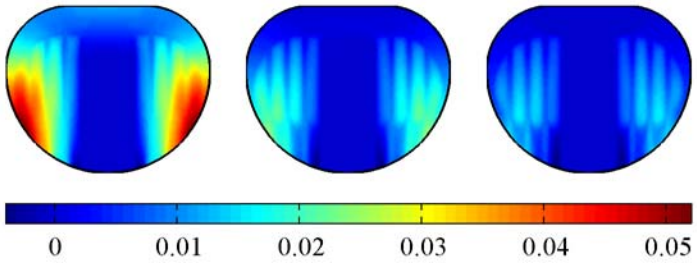

Figure 6-11. Computed BR wing deformation (w/c) with one layer of plain weave (left), two layers (center), and three layers (right), α = 12º.

This inability of the slack membrane wing to alleviate the flight loads decreases the efficiency, but surprisingly, has little effect on the stability derivatives. One possible reason for this is the negative deformations at the trailing edge of the three-layer MAV wing. The stiffer wing adheres closely to the original, rigid wing shape, which contains reflex (negative camber) at the trailing edge. The negative forces in this area push the membrane downward, increasing the wing camber. Increasing the stiffness of the plain weave laminate may convert the BR wing from a structure with adaptive washout to one with progressive de-cambering, leaving the

longitudinal stability derivatives relatively unchanged.

Greater variation with laminate thickness is seen for non-zero pre-tensions, particularly when N_x = 20 N/m and N_y = 10 N/m. If a single layer of carbon fiber is used, this data point represents the minimum lift slope. Like the double-layered laminates studied above, the BR wing removes the camber due to membrane inflation (and thus the lift) at the leading edge with high chordwise stiffness, and allows for adaptive washout with low spanwise stiffness perpendicular to the battens. Such a design has biological inspiration: the bone-reinforced membrane skins of pterosaurs [101] and bats [102] both have larger chordwise stiffness. For low levels of pre-tension, decreasing the number of plain weave layers increases the efficiency; if the membrane is highly-tensioned, the opposite is true. The L/D objective function is optimized with a one-layer slack membrane BR wing. It can also be seen in Figure 6-10 that for high levels of membrane pre-tension, there is little computed difference between 2 and 3 layer laminates.

Similar data is given in Figure 6-12 and Figure 6-13, for a PR wing. The single-layer PR wing exhibits a substantial amount of adaptive washout, owning to deflection of the weak carbon fiber perimeter. Two and three-layer laminates remove this feature completely, forcing the wing into a pure aerodynamic twist. Regardless of the load alleviation along the trailing edge, the steepest lift and moment curves are found with single-layer laminates, as the weak carbon fiber reinforcement intensifies the cambering of the membrane wing. The two-dimensional equivalent to this case is a sailwing with the trailing edge attached to a flexible support. Well-known solutions to this problem indicate that increasing the flexibility of the support improves the static stability [67], a trend re-iterated in Figure 6-12.

None of the PR aerodynamic metrics or the displacement contours show a substantial difference between two and three layer laminates. For the thicker laminates, increasing the

spanwise pre-tension provides steeper lift and pitching moment curves; the system has a low sensitivity to chordwise pre-tension. This may be due to the membrane skin's shape: its chord is much greater than its span, as discussed above.

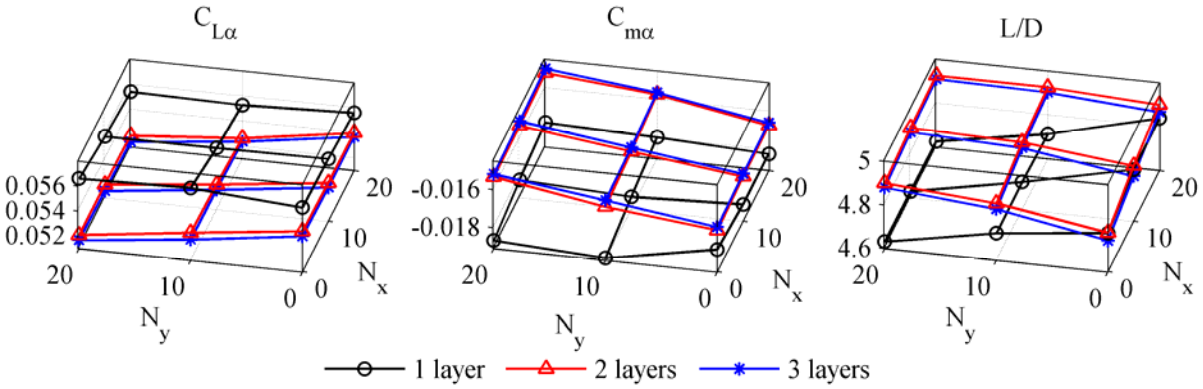

Figure 6-12. Computed full factorial design of a PR wing, α = 12º.

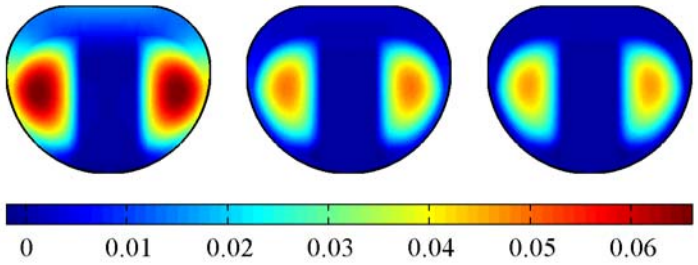

Figure 6-13. Computed PR wing deformation (w/c) with one layer of plain weave (left), two layers (center), and three layers (right), α = 12º.

For one-layer laminates, no clear trend between $C_{L\alpha}$, $C_{m\alpha}$, and pre-tension (chordwise or spanwise) emerges. Whereas the thicker laminates prefer a slack membrane wing to optimize longitudinal static stability, the one-layer wing optimizes this metric when 10 N/m is applied in the span direction. The reflex in the airfoil shape may again be the reason for this. The mild amount of spanwise pre-tension enforces the intended reflex in the membrane skin, and the downward forces depress the membrane skin (seen in Figure 6-4). Slight increases in angle of attack increases the inflation camber towards the leading edge, but decreases the reflex at the trailing edge, resulting in a significant restoring moment. The efficiency of thick-laminate PR

wings is equally degraded by chordwise and spanwise pre-tensions. The opposite is true for single-layers, where L/D can actually be improved with less tension.

The above data is recompiled in Figure 6-14, which plots the performance of the 27 BR designs, the 27 PR designs, and the rigid wing, in terms of the lift slope and pitching moment slope as a function of L/D. As seen many times in the above plots, the various objective functions conflict: tailoring a wing structure for longitudinal static stability may induce a severe drag penalty, for example. No wing design exists (typically) that will optimize all of the relevant performance metrics, and compromise designs must be considered. The set of compromise solutions fall on the design space's Pareto optimal front [156]. A Pareto optimal solution is non-dominated: no solution exists within the data set that out performs the Pareto optimal solution in all of the performance metrics.

Three Pareto fronts are given in Figure 6-14. The first details the tradeoff between maximizing L/D while minimizing $C_{L\alpha}$. The second gives the tradeoff between maximizing L/D while maximizing $C_{L\alpha}$, and the final front is a tradeoff between maximizing L/D while minimizing $C_{m\alpha}$. It may be beneficial for a MAV wing to have a very steep lift slope (for efficient pull-up maneuvers, for example) or very shallow (for gust rejection), so both are included. All three of these objective functions could be used to compute a common Pareto front, but visualization of the resulting hypersurface would be difficult. Furthermore, maximizing $C_{L\alpha}$ and minimizing $C_{m\alpha}$ evolve from similar mechanisms, and seldom conflict.

The overlap between BR wings and PR wings in Figure 6-14 is minimal, with the latter design typically having higher efficiency and shallow lift and moment slopes. The rigid wing lies close to the interface between the two membrane wing types, but is not Pareto optimal. The basic performance tradeoffs are readily visible: peak L/D is 5.49 (a single-layer BR wing with a

slack membrane), a design whose lift slope is 8% higher than the minimum possible lift slope, 18% lower than the maximum possible lift slope, and whose pitching moment slope is 34% higher than the minimum possible moment slope.

Most of the dominated solutions do not lie far from the Pareto front, indicative of the fact that all of the objective functions are obtained by integrating the pressure and shear distributions over the wing. Substantial variations in the CFD state variables can be obtained on a local level through the use of wing flexibility (Figure 5-21, for example), but integration averages out these deviations. It can also be seen that two of the three Pareto fronts in Figure 6-14 are non-convex. As such, techniques which successively optimize a weighted sum of the two objective functions (convex combination) to fill in the Pareto front will not work; more advanced schemes, such as elitist-based evolutionary algorithms [156], must be used.

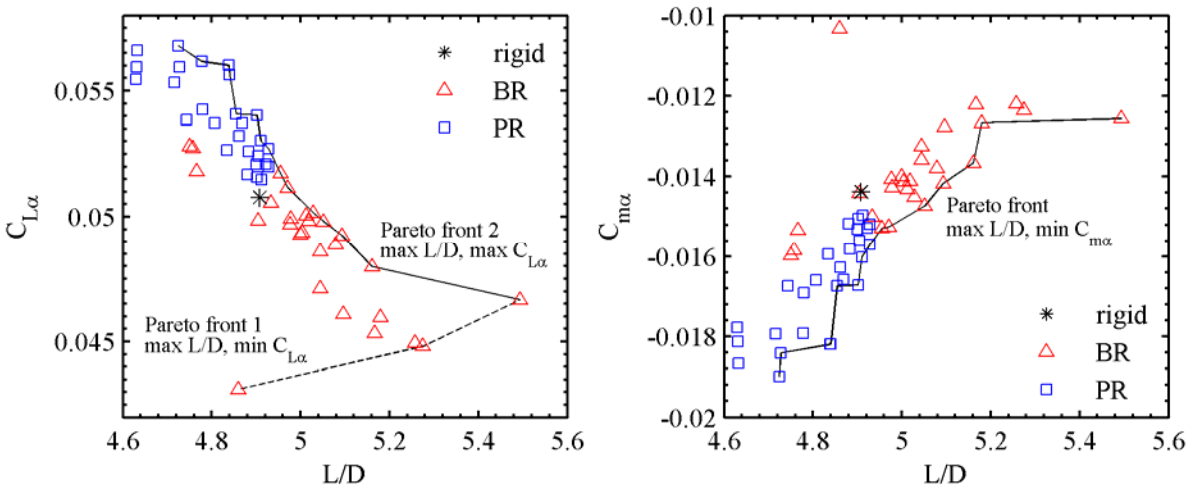

Figure 6-14. Computed design performance and Pareto optimality, $\alpha = 12°$.

Having successfully implemented the designed experiment, the typical next step is to fit the data with a response surface, a technique used by Sloan et al. [53] and Levin and Shyy [104] for MAV work. Having verified the validity of the surrogate, it can then be used as a relatively inexpensive objective function for optimization. Such a method is not used here for several

reasons. First, half of the design variables (wing type and laminate thickness) are discrete, which as discussed by Torres [3], can cause convergence problems in conventional optimization algorithms. Second, nonlinear curve fitting is likely required (membrane wing performance asymptotically approaches that of a rigid wing for increased pre-tension), and the moderate number of data points (only 9 for each wing type and laminate thickness) won't provide enough information for an adequate fit. Finally, such a method may result in an optimal pre-stress resultant of 5.23 N/m, for example. As discussed above, the actual application of pre-tension to a membrane MAV wing is an inexact science, and such resolution could never be produced in the laboratory (or more importantly, the field) with any measure of repeatability or accuracy.

A more practical approach is to simply treat the pre-tension as a discrete variable: taut (~20 N/m), moderate (~10 N/m), and slack (0 N/m). Figure 6-10 and Figure 6-12 now represent an enumeration-type optimization, wherein every possible design is tested. Optimal wing designs in terms of 7 objective functions (maximum L/D, minimum mass, maximum lift, minimum drag, minimum pitching moment slope, maximum lift slope and minimum lift slope) are located among the 55 available data points, and given along the diagonal of the design array in Table 6-1. Results from the OFAT tests above are not included.

Satisfactory compromise designs are found by first normalizing design performance between 0 and 1, and then locating a utopia point. This utopia point is a (typically) fictional design point which would simultaneously optimize both objective functions. In the design trade-of between L/D and $C_{m\alpha}$ in Figure 6-14, the utopia point is (5.49, -0.0189). An adequate compromise is the Pareto optimal design which lies closest to the utopia point; these are listed in the off-diagonal cells in Table 6-1. This method is found to give a better compromise than optimizing a convex combination of the two objective functions, presumably due to the non-

convexity of the Pareto fronts. Only compromises between 2 objective functions are considered in this work. The corresponding performance of each design is given in Table 6-2. The value in each cell is predicated upon the label at the top of each column; the performance of the second objective function (row-labeled) is found in the cell appropriately located across the diagonal.

Table 6-1. Optimal MAV design array with compromise designs on the off-diagonal, $\alpha = 12^{o}$: design description is (wing type, N_x, N_y, number of plain weave layers).

	max L/D	min mass	max C_L	min C_D	min $C_{m\alpha}$	max $C_{L\alpha}$	min $C_{L\alpha}$
max L/D	**BR,0,0,1L**	BR,0,0,1L	PR,10,0,1L	BR,0,0,1L	BR,20,0,3L	PR,20,0,2L	BR,0,0,1L
min mass	BR,0,0,1L	**PR,20,20,1L**	PR,0,0,1L	BR,0,0,1L	PR,0,10,1L	PR,0,10,1L	BR,20,10,1L
max C_L	PR,10,0,1L	PR,0,0,1L	**PR,0,0,1L**	BR,0,10,1L	PR,0,0,1L	PR,0,0,1L	BR,20,10,1L
min C_D	BR,0,0,1L	BR,0,0,1L	BR,0,10,1L	**BR,0,0,1L**	BR,20,0,3L	BR,10,20,3L	BR,10,0,1L
min $C_{m\alpha}$	BR,20,0,3L	PR,0,10,1L	PR,0,0,1L	BR,20,0,3L	**PR,0,10,1L**	PR,0,10,1L	BR,20,0,3L
max $C_{L\alpha}$	PR,20,0,2L	PR,0,10,1L	PR,0,0,1L	BR,10,20,3L	PR,0,10,1L	**PR,0,10,1L**	BR,0,20,3L
min $C_{L\alpha}$	BR,0,0,1L	BR,20,10,1L	BR,20,10,1L	BR,10,0,1L	BR,20,0,3L	BR,0,20,3L	**BR, 20,10,1L**

Table 6-2. Optimal MAV design performance array, $\alpha = 12^{o}$: off-diagonal compromise design performance is predicated by column metrics, not rows.

	max L/D	min mass (g)	max C_L	min C_D	min $C_{m\alpha}$	max $C_{L\alpha}$	min $C_{L\alpha}$
max L/D	**5.49**	4.36	0.780	0.112	-0.015	0.054	0.047
min mass	5.49	**4.10**	0.817	0.112	-0.019	0.057	0.043
max C_L	4.84	4.18	**0.817**	0.145	-0.018	0.056	0.043
min C_D	5.49	4.36	0.716	**0.112**	-0.014	0.052	0.045
min $C_{m\alpha}$	5.05	4.16	0.817	0.134	**-0.019**	0.057	0.049
max $C_{L\alpha}$	4.90	4.16	0.817	0.141	-0.019	**0.057**	0.050
min $C_{L\alpha}$	5.49	4.31	0.673	0.119	-0.015	0.049	**0.043**

For reference purposes, the design performance of the rigid wing (at 12° angle of attack) is: L/D = 4.908, mass = 6.36 grams, $C_L = 0.6947$, $C_D = 0.1415$, $C_{m\alpha} = -0.0147$, and $C_{L\alpha} = 0.0507$. As above, at no point does the rigid wing represent an optimum design (compromise or otherwise). The compromise between minimizing the lift slope, and maximizing the lift slope is identified by located the design closest to the normalized $C_{L\alpha}$ of 0.5. This is found by a BR wing design with peak pre-tension normal to the battens to limit adaptive washout, but no pre-tension in the chordwise direction to allow for camber and lift via inflation. Both BR and PR wings are equally-represented throughout the design array, with the exception of designs requiring load alleviation: all compromises involving drag or lift slope minimization utilize a BR wing. The

majority of the optimal designs use a single layer of plain weave carbon fiber to take the most advantage of wing flexibility. A single layer slack BR wing can minimize drag through streamlining [63], for example, as a significant portion of the wing is deformed (Figure 6-11). A few designs use 3 layers; only one design uses 2 layers.

A few compromise wing designs coincide with the utopia point: a one-layer BR wing with a slack membrane maximizes L/D and minimizes the drag. A one-layer PR wing with no pre-tension in the chordwise direction and 10 N/m in the spanwise direction provides the steepest lift slope and pitching moment slope. Most compromise designs improve both objective functions, compared to the rigid wing, but the system particularly struggles to maximize both L/D and lift (above results indicate that efficiency improvements are driven by drag reduction), and to maximize lift and minimize the lift slope.

The conflictive nature of the objective functions means that looking at designs that strike a reasonable compromise between three or more aerodynamic metrics is of minor usefulness. It should be noted however, that the design that lies closest to the utopia point of all 7 objectives shown in Table 6-1 is a 2-layer BR wing with a slack membrane in the chordwise direction, and 10 N/m of pre-tension spanwise, similar to the design that lies closest to the normalized $C_{L\alpha}$ of 0.5, as discussed above. Finally, mass minimization is obviously afforded with a single layer of plain weave carbon fiber: membrane pre-tension then provides moderate and insignificant deviations from this value, by changing the amount of latex used over the MAV wing.

Experimental Validation of Optimal Design Performance

The design results from the single-objective optimization studies (the diagonal of Table 6-1, with the exception of the minimum mass design) are fabricated and tested in the wind tunnel. Only loads are measured through the α-sweep, for comparison with the experimental data from the three baseline wings designs in Chapter 5. As discussed above, each of these wing designs

utilize a single layer of plain weave carbon fiber. Two layers are typically used for MAVs of this scale. Despite the extremely compliant nature of the wings (which is precisely why they were located as optimal), all designs are able to withstand flight loads in the wind tunnel without buckling. Whether they can withstand maneuver loads or strong gusts is still unknown however, as is their ability to endure a flight crash without breaking.

Some wing designs display substantial leading edge vibration at very low and negative angles of attack (presumably due to the vortex shedding from the separation bubble seen in Figure 5-17), though deformation is observed to be quasi-static above 3º and prior to stall. The required pre-stress resultants are converted into pre-strains using Hooke's law, and applied to a square of latex rubber by uniformly stretching each side. VIC is used to confirm the pre-strain levels, with spatial coefficients of variation between 10 and 20%, similar to data given in Figure 4-6 and by Stanford et al. [43].

Results for lift-related optima are given in Figure 6-15. The design that maximizes C_L (PR,0,0,1L) produces more lift than the baseline PR wing up to 10º angle of attack, though within the error bars (not shown, but on the order of 5%). Above this angle the wing shows a premature stall: $C_{L,\,max}$ is much lower than measured from the baseline PR wing, bearing closer similarities to the rigid wing. The vibration and buffeting typically seen over MAV wings towards stall is obviously magnified for these compliant designs; the coupling between the shedding and the wing vibration may contribute to the loss of lift, as demonstrated in the work of Lian and Shyy [8]. The upward deformation of the single layer trailing edge perimeter is substantial (as seen in Figure 6-13), and the resulting adaptive washout may also play a role. Similar results are seen for the wing design that maximizes $C_{L\alpha}$ (PR,0,10,1L), though in this case the lift slope is nearly identical to that measured from the baseline PR wing up to 10º, after which

premature stall occurs. This benign stall behavior is not necessarily detrimental [49], though unintended by the numerical model, caused by optimizing at a single angle of attack with a steady aeroelastic solver.

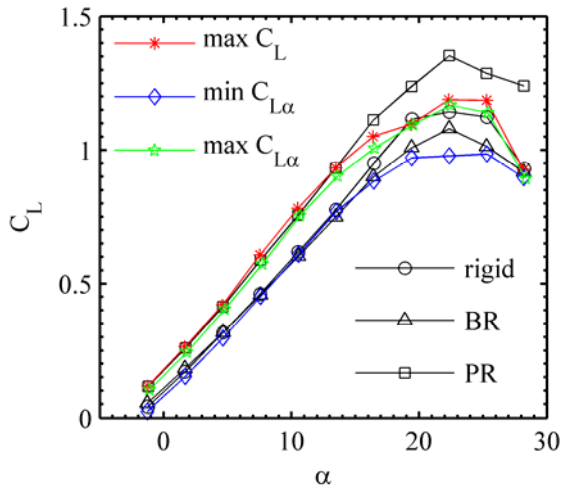

Figure 6-15. Experimentally measured design optimality over baseline lift.

The optimizer is considerably more successful when minimizing $C_{L\alpha}$ with design (BR,20,10,1L), as seen in Figure 6-15. The BR wings used in these tests are qualitatively observed to have smaller vibration amplitudes, compared to the PR wings, at very low and very high angles of attack. At low angles of attack, the lift of the optimal design is smaller than both the baseline rigid and BR wings, though the lift slope is comparable. For moderate angles, no significant differences are evident. After 10º however, the optimal design shows a clear drop in lift slope, a very flat stalling region, and stalling angle delayed by 3º over the baseline designs. $C_{L,\,max}$ is measured to be 9% less than that measured for the baseline BR wing.

Experimental validation results for the wing design minimizing the pitching moment slope (PR,0,10,1L) is given in Figure 6-16. As before, performance of the baseline PR wing and the optimal design are comparable up to 13º. Above this angle, and through the stalling region, the optimal design has a steeper slope than the baseline PR wing. At these angles, the nose-down pitching moment is stronger than that seen in the baseline BR and rigid wings, but the slope is

similar. This is largely due to the linear pitching moment behavior previously noted on the PR wings, possibly due to membrane inflation interference with the tip vortices [14]. Despite the measured improvements over the baseline PR wing, the data indicates that longitudinal control beyond stall (~ 28º) may not be possible [27]. Interestingly, the same wing design theoretically minimizes the moment slope and maximizes the lift slope, but only the former metric is considerably improved over the baseline.

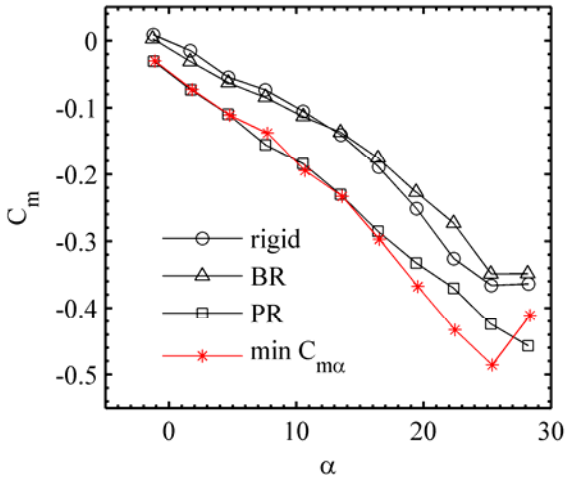

Figure 6-16. Experimentally measured design optimality over baseline pitching moments.

Similar validation results are given in Figure 6-17 and Figure 6-18, for the minimization of drag and maximization of L/D. Both metrics are optimized by wing design (BR,0,0,1L). The drag is consistently lower than the three baseline designs up to 20º. Accurate drag data for micro air vehicles at low speeds is very difficult to measure, largely due to resolution issues in the sting balance [34]. Questionable data typically manifests itself through atypically low drag. Regardless, the veracity of the data from the optimal wing in Figure 6-17 may be confirmed by the identical results at the bottom of the drag bucket with the rigid wing, where deformation is very small. The data also compares very well with computed results. Unlike the baseline BR wing, the optimal design has less drag at a given angle of attack and at a given value of lift (the latter of which is visible in the drag polar, which is not shown). Past 20º, the optimal design

shows more of a drag penalty than the baseline BR wing, which may also be attributed to larger vibration amplitudes in the single-layer wing.

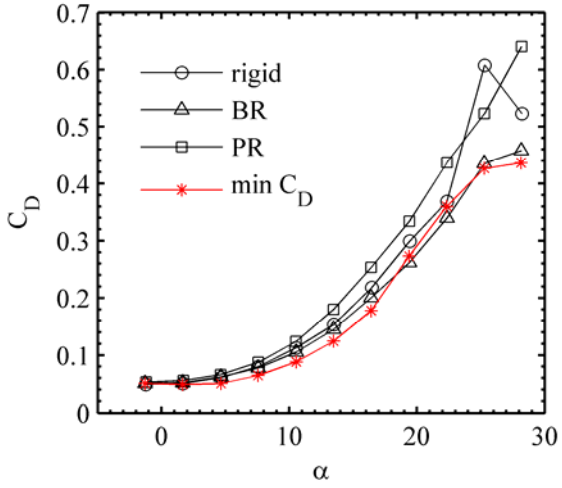

Figure 6-17. Experimentally measured design optimality over baseline drag.

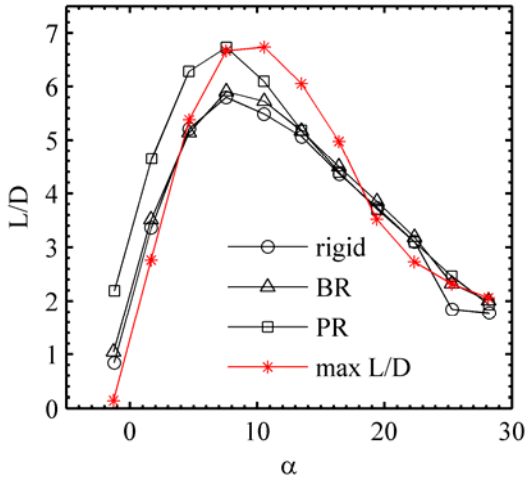

Figure 6-18. Experimentally measured design optimality over baseline efficiency.

The results for optimal efficiency (Figure 6-18) show substantial improvements over the three baseline designs for a range of moderate angles: 8º - 18º. The optimization is only conducted at 12º angle of attack; whereas the previously considered optimal designs can be reasonably considered ideal throughout most of the α-sweep (up to stall), the conflictive nature of the lift-to-drag ratio is more complex. This can be seen in the numerical data of Figure 5-15, where the baseline BR, PR, and rigid wings all have the highest L/D for different lift values. It is

expected that optimizing at different angles of attack will produce radically different optimal L/D designs, but similar results may be retained for the remaining objectives.

Of the six aerodynamic objectives considered in this section, wind tunnel testing indicates that two are unmistakably superior to the baselines over a large range of angles of attack (minimum drag and maximum efficiency), and two have similar responses to one or more of the baseline designs for small and moderate angles but are clearly superior for higher angles of attack (minimum lift and pitching moment slopes). One objective (maximum lift) is slightly better at moderate angles (though not beyond the measured uncertainty), but decidedly inferior during stall, while another objective (maximum lift slope) is identical to the baseline for moderate angles, and again inferior during stall.

With the exception of these latter two studies, this wind tunnel validation confirms the use of numerical aeroelastic tailoring for realizable improvements to actual MAV wings. This is not to indicate that the latter two studies have failed: the computed performance of the tailored wings is not always significantly better than the baseline, and may be blurred by experimental errors. The experimental data of these two designs is not significantly better than the baseline designs, but not measurably worse either (for moderate angles).

CHAPTER 7
AEROELASTIC TOPOLOGY OPTIMIZATION

The conceptual design of a wing skeleton essentially represents an aeroelastic topology optimization problem. Conventional topology optimization is typically concerned with locating the holes within a loaded homogenous structure, by minimizing the compliance [16]. This work details the location of holes within a carbon fiber wing shell, holes which will then be covered with a thin, taut, rubber membrane skin. In other words, the wing will be discretized into a series of panels, wherein each panel can be a carbon fiber laminated shell or an extensible latex rubber skin. Rather than compliance, a series of aerodynamic objective functions can be considered, including L/D, C_L, C_D, $C_{L\alpha}$, $C_{m\alpha}$, etc.

While the two wing topologies discussed in the preceding section (batten- and perimeter-reinforced wings) have been shown to be effective at load alleviation via streamlining and load augmentation via cambering, respectively, both designs have deficiencies. The BR wing experiences membrane inflation from in-between the battens towards the leading edge (Figure 5-1), cambering the wing and contradicting the load alleviating effects of the adaptive washout at the trailing edge. Furthermore, the unconstrained trailing edge is only moderately effective at adaptive geometric twist, as the forces in this region are very small (Figure 5-20). If re-curve is built into the wing section, the forces in this area may push the trailing edge downward, actually increasing the incidence, and thus the loads.

The PR wing, being a simpler design, is more effective in its intended purpose (adaptive cambering for increased lift and static stability), but the drastic changes in wing geometry at the carbon fiber/membrane interfaces towards the leading and trailing edges of the membrane skin are aerodynamically inefficient. Large membrane inflations are also seen to lead to potentially unacceptable drag penalties as well. All of these deficiencies can be remedied via the tailoring

studies considered above, but the greater generality of an aeroelastic topology scheme (due to the larger number of variables) would suggest better potential improvements in aerodynamic performance. Furthermore, such an undertaking can potentially be followed by an aeroelastic tailoring study of the optimal topology for further improvements, as discussed by Krog et al. [115]: topology optimization to locate a good design, followed by sizing and shape optimization.

A flexible MAV wing topological optimization procedure has some precedence in early micro air vehicle work by Ifju et al. [10], with an array of successfully flight tested designs shown in Figure 7-1. Each of these designs consists of a laminated leading edge, wing tip, and wing root; a series of thin strips of carbon fiber are imbedded within the concomitant membrane skin. Both the BR and PR wings are present, along with slight variations upon those themes. Ifju et al. [10] qualitatively ranks these wing structures based upon observations in the field and pilot-reported handling qualities: a crude trial and error process led to the batten-reinforced design as a viable candidate for MAV flight.

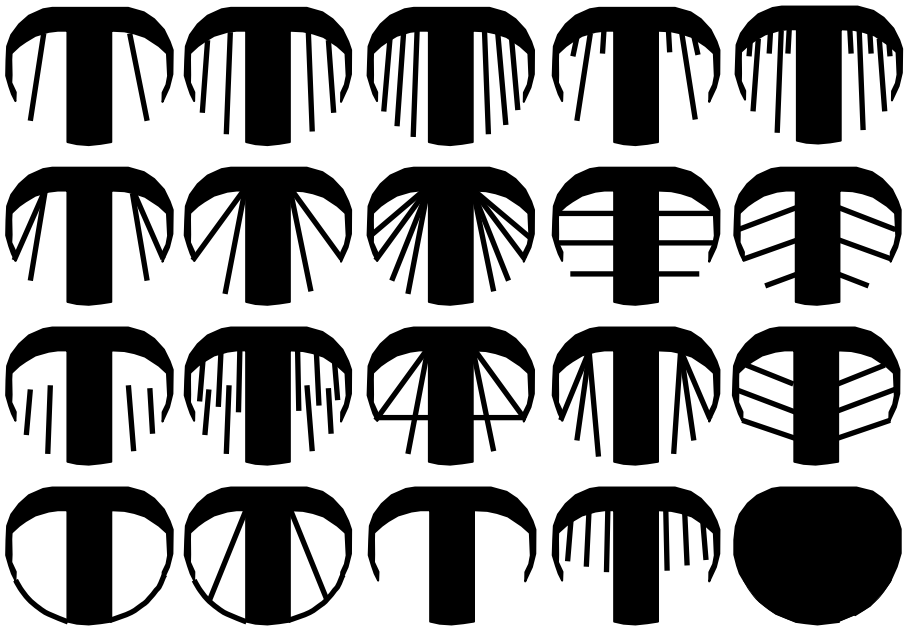

Figure 7-1. Wing topologies flight tested by Ifju et al. [10].

Several challenges are associated with the optimization procedure considered here. First, a

fairly fine structural grid is needed to resolve topologies on the order of those seen in Figure 7-1. The fine grid will, of course, increase the computational cost associated with solving the set of FEA equations, as the number of variables in the optimization algorithm is proportional to the number of finite elements. The wing is discretized into a set of quadrilaterals, which represent the density variables: 0 or 1. These quadrilaterals are used as panels for the aerodynamic solver, and broken into two triangles for the finite element solver, as shown in Figure 7-2. As in Figure 7-1, the wing topology at the root, leading edge, and wing tip is fixed as carbon fiber, to maintain some semblance of an aerodynamic shape capable of sustaining lift. The wing topology in the figure is randomly distributed.

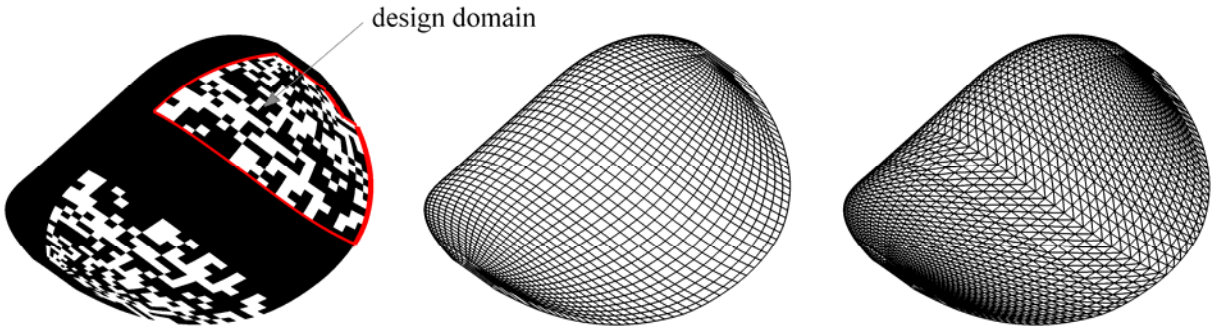

Figure 7-2. Sample wing topology (left), aerodynamic mesh (center), and structural mesh (right).

Further complications are associated with the fact that these variables are binary integers: 1 if the element is a carbon fiber ply, 0 if the element is latex membrane. Several binary optimization techniques (genetic algorithms [109], for example) are impractical for the current problem, due to the large number of variables, but also due to the extremely large computational cost associated with each aeroelastic function evaluation. A fairly standard technique for topology optimization problems classifies the density of each element as continuous, rather than binary [16]. Intermediate densities can then be penalized (implicitly or otherwise) to push the design towards a pure carbon fiber/membrane distribution, with no “porous” material.

The sensitivity of each element's density variable upon the wing's aerodynamic performance is required for this gradient-based optimization scheme. As before, the large number of variables and the expensive function evaluations preclude the use of simple finite difference schemes for computation of gradients. An adjoint sensitivity analysis of the coupled aeroelastic system is thus required, as the number of design variables is much larger than the number of objectives/constraints [110]. Further complications arise from the fact that second derivatives are also required: important MAV aerodynamic performance metrics such as the slope of the lift curve, for example, are sensitivity derivatives that depend upon the characteristics of the aeroelastic system as well.

This chapter provides a computational framework for computing the adjoint aeroelastic sensitivities of a coupled aeroelastic system, as well as interpolation schemes between carbon fiber and membrane finite elements and methods for penalizing intermediate densities. The dependency of the computed optimal topology upon mesh density, angle of attack, initial topology, and objective function are given, as well as the resulting deformation and pressure distributions. The wing designs created via aeroelastic topology optimization demonstrate a clear superiority over the baseline BR and PR designs discussed above in terms of load alleviation (former) and augmentation (latter), advantages which are further expounded through wind tunnel testing. Multi-objective topology optimization is discussed as well, with the evolution of the optimal wing topology as one travels along the Pareto optimal front.

Computational Framework

Material Interpolation

Topology optimization often minimizes the compliance of a structure under static loads, with an equality constraint upon the volume. If the density of each element is allowed to vary continuously, an implicit penalty upon intermediate densities (to push the final structure to a 0-1

material distribution) can be achieved through a nonlinear power law interpolation. This technique is known as the solid isotropic material with penalization method, or SIMP [105].

For the two-material wing considered above (membrane or carbon fiber), the stiffness matrix $\mathbf{K}_e$ of each finite element in Figure 7-2 can be computed as:

$$\mathbf{K}_e = \left(\mathbf{K}_p \cdot (1-\beta) - \mathbf{K}_m\right) \cdot X_e^p + \mathbf{K}_m + \beta \cdot \mathbf{K}_p \tag{7-1}$$

where $\mathbf{K}_p$ and $\mathbf{K}_m$ are the plate and membrane elements, respectively (the latter with zeros placed within rows and columns corresponding to bending degrees of freedom). β is a small number used to prevent singularity in the pure membrane element (due to the bending degrees of freedom), and X_e is the density of the element, varying from 0 (membrane) to 1 (carbon fiber). p is the nonlinear penalization power (typically greater than 3).

A common criticism of this power law approach is that intermediate densities do not actually exist. This is a particular problem for the current application, where each element is either carbon fiber or membrane rubber. The physics of these two elements is completely different, as the carbon fiber is inextensible yet has resistance to bending and twisting, while the opposite is true for the latex. An equal combination of these two (equivalent to stating that the density within an element is 0.5), while computationally conceivable, is not physically possible. The wing topology will not represent a real structure until the density of each element is pushed to 1 (carbon fiber) or 0 (membrane).

The power law's effectiveness as an implicit penalty is predicated upon a volume constraint: intermediate densities are unfavorable, as their stiffness is small compared to their volume [16]. No such volume constraint is utilized here, due to an uncertainty upon what this value should be. Furthermore, for aeronautical applications it is typically desired to minimize the mass of the wing itself, as discussed by Maute et al. [118]. Regardless, the nonlinear power

law of SIMP is still useful for the current application, as demonstrated in Figure 7-3. Both linear and nonlinear material interpolations are given for the lift computation, and the wing topology is altered uniformly.

For the linear interpolation (i.e., without SIMP), the aeroelastic response is a weak function of the density until X becomes very small (~0.001), when the system experiences a very sharp change as X is further decreased to 0. This is a result of the large stiffness imbalance between the carbon fiber laminates and the membrane skin, and the fact that lift is a direct function of the wing's compliance (the inverse of the weighted sum of the two disparate stiffness matrices in Eq. (7-1)). The inclusion of a nonlinear penalization power (p = 5), spreads the response evenly between 0 and 1. Aeroelastic topology optimization with linear material interpolation experiences convergence difficulties, as the gradient-based technique struggles with the nearly-disjointed design space; a penalization power of 5 is utilized for the remainder of this work.

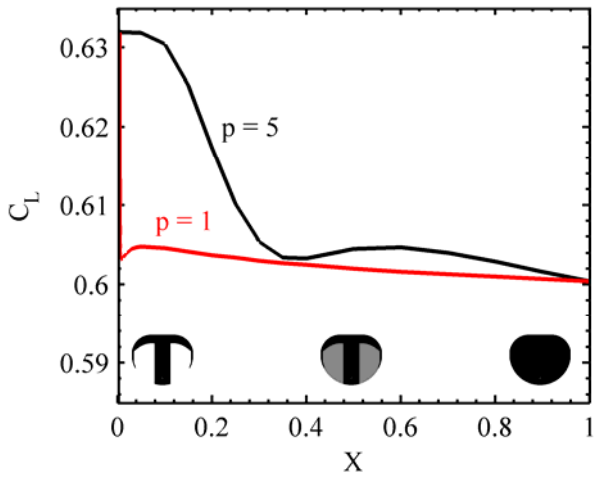

Figure 7-3. Effect of linear and nonlinear material interpolation upon lift.

The results from Figure 7-3 suggest a number of other potential difficulties with an aeroelastic topology optimization scheme. First, the sensitivity of the aeroelastic response to element density is zero for a pure membrane wing (X = 0), as can be inferred from Eq. (7-1). As such, using a pure membrane wing as an initial guess for optimization will not work, as the

design won't change. Secondly, two local optima exist in the design space of Figure 7-3, which may prevent the gradient-based optimizer from converging to a 0-1 material distribution. To counteract this problem, an explicit penalty on intermediate densities is added to the objective function, as discussed by Chen and Wu [158]:

$$R \cdot \sum_{i=1}^{N_X} \sin\left(X_i \cdot \pi\right) \tag{7-2}$$

where R is a penalty parameter appropriately sized so as not to overwhelm the aerodynamic performance of the wing topology. This penalty is only added when and if the aeroelastic optimizer has converged upon a design with intermediate densities, as will be discussed below.

Aeroelastic Solver

Due to the large number of expected function evaluations (~ 200) needed to converge upon an optimal wing topology, and the required aeroelastic sensitivities (computed with an adjoint method), a lower-fidelity aeroelastic model (compared to that utilized in Chapters 5 and 6) must be used for the current application. An inviscid vortex lattice method (Eq. (4-11)) is coupled to a linear orthotropic plate model and a linear stress stiffening membrane model (Eq. (4-4)). The latter module is perfectly valid in predicting membrane inflation as long as the state of pre-stress is sufficiently large, as seen in Figure 4-5. Furthermore, in-plane stretching of the laminate is ignored; only out-of-plane displacements (as well as in-plane rotations in the laminate) are computed over the entire wing.

The vortex lattice method is reasonably accurate as well, despite the overwhelming presence of viscous effects within the flow. As seen in Figure 4-11, the lift slope is consistently under-predicted due to an inability to model the large tip vortices [3], and the drag is under-predicted at low and high angles of attack due to separation of the laminar boundary layer [4].

Aeroelastic coupling is facilitated by considering the system as defined by a three field

response vector **r**:

$$\mathbf{r} = \left\{ \mathbf{u}^T \quad \mathbf{z}^T \quad \boldsymbol{\Gamma}^T \right\}^T \tag{7-3}$$

where **u** is the solution to the system of finite element equations (composed of both displacements and rotations) at each free node, **z** is the shape of the flexible wing, and **Γ** is the vector of unknown horseshoe vortex circulations. The coupled system of equations **G**(r) is then:

$$\mathbf{G}(\mathbf{r}) = \begin{Bmatrix} \mathbf{K}\cdot\mathbf{u} - \mathbf{Q}\cdot\boldsymbol{\Gamma} \\ \mathbf{z} - \mathbf{z}_o - \mathbf{P}\cdot\mathbf{u} \\ \mathbf{C}\cdot\boldsymbol{\Gamma} - \mathbf{L} \end{Bmatrix} = \mathbf{0} \tag{7-4}$$

The first row of **G** is the finite element analysis: **K** is the stiffness matrix assembled from the elemental matrices in Eq. (7-1), and appropriately reduced based upon fixed boundary conditions along the wing root. **Q** is an interpolation matrix that converts the circulation of each horseshoe vortex into a pressure, and subsequently into the transverse force at each free node. The second row of **G** is a simple grid regeneration analysis: $\mathbf{z}_o$ is the original (rigid) wing shape, and **P** is a second interpolation matrix that converts the finite element state vector into displacements at each free and fixed node along the wing. The third row of **G** is the vortex lattice method. **C** is an influence matrix depending solely on the wing geometry (computed through the combination of Eqs. (4-11) and (4-12)), and **L** is a source vector depending on the wing's outward normal vectors, the angle of attack, and the free stream velocity. Convergence of this system can typically be obtained within 25 iterations, and is defined when the logarithmic error in the wing's lift coefficient is less than -5.

One potential shortcoming of this aeroelastic model can be seen in Figure 7-3, where the computed lift of a wing with no carbon fiber in the design domain (X = 0) is larger than the lift generated by the rigid wing (X = 1). This is due to a combination of membrane cambering towards the leading edge, and a depression of the trailing edge reflex region. In reality, however,

the combination of a poorly-constrained trailing edge and unsteady vortex shedding will lead to a large-amplitude flapping vibration, similar to that discussed by Argentina and Mahadevan [62]. Wind tunnel testing of this wing is given in Figure 7-4 at 13 m/s; the critical speed of flapping vibration is approximately 3 m/s.

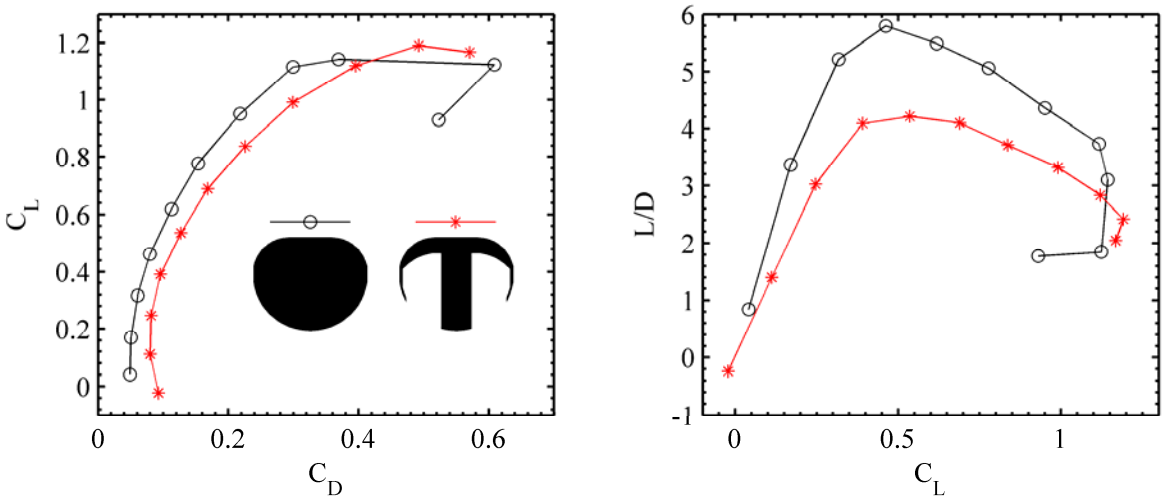

Figure 7-4. Measured loads of an inadequately reinforced membrane wing, U_∞ = 13 m/s.

As expected, the measured lift of the membrane wing is significantly less than that measured from the rigid wing in the wind tunnel: the poorly-supported wing cannot sustain the flight loads, while the large amplitude vibrations levy a substantial drag penalty. Even a mild amount of trailing edge reinforcement (such as that seen in the upper left of Figure 7-1) will prevent this behavior, but formulating a constraint that will push the aeroelastic topology optimizer away from wing designs with a poorly-reinforced trailing edge is difficult, and is not included. This section only serves to highlight one significant shortcoming of the aeroelastic model used here, and to diminish the perceived optimality of certain wing topologies.

Adjoint Sensitivity Analysis

As the number of variables in the aeroelastic system (essentially the density of each element) will always outnumber the number of constraints and objective functions, a sensitivity

analysis can be most effectively carried out with an adjoint analysis. The sought-after total derivative of the objective function with respect to each density variable is given through the chain rule:

$$\frac{\mathrm{dg}}{\mathrm{d}\mathbf{X}} = \frac{\partial \mathrm{g}}{\partial \mathbf{X}} + \frac{\partial \mathrm{g}}{\partial \mathbf{r}}^{\mathrm{T}} \cdot \frac{\mathrm{d}\mathbf{r}}{\mathrm{d}\mathbf{X}} \tag{7-5}$$

where g is the objective function (a scalar for the single-objective optimization scheme considered here; multi-objective optimization will be discussed below) and **r** is the aeroelastic state vector discussed above. The term $\partial g/\partial \mathbf{X}$ is the explicit portion of the derivative, while the latter term is the implicit portion through dependence on the aeroelastic system [159]. Only aerodynamic objective functions are considered in this work: the explicit portion is then zero, unless the intermediate density penalty of Eq. (7-2) is included.

The derivative of the aeroelastic state vector with respect to the element densities is found by differentiating the coupled system of Eq. (7-4):

$$\frac{\mathrm{d}\mathbf{G}(\mathbf{X},\mathbf{r})}{\mathrm{d}\mathbf{X}} = \mathbf{0} \quad \Rightarrow \quad \frac{\partial \mathbf{G}}{\partial \mathbf{X}} + \mathbf{A} \cdot \frac{\mathrm{d}\mathbf{r}}{\mathrm{d}\mathbf{X}} = \mathbf{0} \tag{7-6}$$

where **A** is the Jacobian of the aeroelastic system, defined by:

$$\mathbf{A} = \frac{\partial \mathbf{G}}{\partial \mathbf{r}} \tag{7-7}$$

Combining Eqs. 7-5 and 7-6 leaves:

$$\frac{\mathrm{dg}}{\mathrm{d}\mathbf{X}} = \frac{\partial \mathrm{g}}{\partial \mathbf{X}} - \frac{\partial \mathrm{g}}{\partial \mathbf{r}}^{\mathrm{T}} \cdot \mathbf{A}^{-1} \cdot \frac{\partial \mathbf{G}}{\partial \mathbf{X}} \tag{7-8}$$

Using the adjoint, rather than the direct method to solve Eq. (7-8), the adjoint vector is:

$$\mathbf{a} = \mathbf{A}^{-\mathrm{T}} \cdot \frac{\partial \mathrm{g}}{\partial \mathbf{r}} \tag{7-9}$$

The system of equations for the adjoint vector does not contain the density of each element

(X), and only needs to be solved once. For the aeroelastic system considered above, the terms that make up the adjoint vector are:

$$\mathbf{A} = \begin{bmatrix} \mathbf{K} & \mathbf{0} & \mathbf{-Q} \\ \mathbf{-P} & \mathbf{I} & \mathbf{0} \\ \mathbf{0} & \mathrm{d}\mathbf{C}/\mathrm{d}\mathbf{z}\cdot\boldsymbol{\Gamma} - \partial\mathbf{L}/\partial\mathbf{z} & \mathbf{C} \end{bmatrix} \tag{7-10}$$

$$\frac{\partial \mathrm{g}}{\partial \mathbf{r}} = \left\{ \mathbf{0} \quad \mathbf{0} \quad \mathbf{S}^{\mathrm{T}} \right\}^{\mathrm{T}} \tag{7-11}$$

where **S** is the derivative of the aerodynamic objective function with respect to the vector of horseshoe vortex circulations. For metrics such as lift and pitching moment, $\mathrm{g} = \mathbf{S}^{\mathrm{T}}\cdot\boldsymbol{\Gamma}$, though more complex expressions exist for drag. The sensitivities can then be computed as:

$$\frac{\mathrm{dg}}{\mathrm{d}\mathbf{X}} = \frac{\partial \mathrm{g}}{\partial \mathbf{X}} - \mathbf{a}^{\mathrm{T}} \cdot \frac{\mathrm{d}\mathbf{G}}{\mathrm{d}\mathbf{X}} \tag{7-12}$$

Only the finite element analysis of the aeroelastic system contains the element densities, and so this final term can be computed as:

$$\frac{\mathrm{d}\mathbf{G}}{\mathrm{d}\mathbf{X}} = \begin{bmatrix} \dfrac{\partial \mathbf{K}}{\partial \mathbf{X}} \cdot \mathbf{u} \\ \mathbf{0} \\ \mathbf{0} \end{bmatrix} \tag{7-13}$$

Of all of the terms needed to undertake the adjoint sensitivity analysis, only the derivative of the vortex lattice influence matrix **C** with respect to the wing shape **z** (a three-dimensional tensor) is computationally intensive, and represents the majority of the cost associated with the gradient calculations at each iteration. In order to solve the linear system of Eq. (7-9), a staggered approach is adapted, rather than solving the entire system of (un-symmetric sparse) equations as a whole, as discussed by Maute et al. [110]. Each sub-problem is solved with the same algorithm used in the aeroelastic solver (direct sparse solver for the finite element

equations, and an iterative Gauss-Seidel solver for the vortex lattice equations), and as such, the computational cost and number of iterations needed for convergence is approximately equal between the aeroelastic solver (Eq. (7-4)) and the adjoint vector solver (Eq. (7-9)).

The second derivative of the objective function is required if aerodynamic derivative metrics such as $C_{L\alpha}$ and $C_{m\alpha}$ are of interest. Two options are available for this computation. The first involves a similar analytical approach to the one described above. This would eventually necessitate the extremely difficult computation of $\partial\mathbf{A}/\partial\mathbf{r}$, which is seldom done in practice [160]. Finite differences are used here:

$$\frac{\partial g^2}{\partial \mathbf{X}\partial\alpha} \approx \frac{1}{\Delta\alpha}\cdot\left(\frac{\partial g}{\partial \mathbf{X}}(\alpha+\Delta\alpha)-\frac{\partial g}{\partial \mathbf{X}}(\alpha)\right) \tag{7-14}$$

The term $\partial g/\partial\alpha$ can be computed using another finite difference, or with the adjoint method described above, substituting the angle of attack for the element densities X.

Optimization Procedure

In order to ensure the existence of the optimal wing topologies, a mesh-independent filter is employed along with the nonlinear power penalization. Such a filter acts as a moving average of the gradients throughout the membrane wing, and limits the minimum size of the imbedded carbon fiber structures. Such a tactic should also limit checkerboard patterns (carbon fiber elements connected just at a corner node). The moving average filter modifies the element sensitivity of node i based on the surrounding sensitivities within a circular region of radius r_{min}, as discussed by Bendsøe and Sigmund [16]:

$$\frac{dg}{dX_{i\ new}} = \frac{1}{X_i\cdot\sum_{j=1}^{N_X} H_{i,j}}\cdot\sum_{j=1}^{N_X}\left(H_{i,j}\cdot X_j\cdot\frac{dg}{dX_j}\right) \qquad H_{i,j}=\begin{cases} r_{min}-dist(i,j) & \text{if } dist(i,j)<r_{min} \\ 0 & \text{otherwise}\end{cases} \tag{7-15}$$

As no constraints are included in the optimization (preferring instead the multi-objective

approach described below), an unconstrained Fletcher-Reeves conjugate gradient algorithm [159] is employed. Step size is kept constant, at a reasonably small value to preserve the fidelity of the sensitivity analysis. The upper and lower bounds of each design variable (1 and 0) are preserved by restricting the step size such that no density variable can leave the design space, forced to lie on the border instead. In order to increase the chances of locating a global optimum (rather than a local optimum), each optimization is run with three distinct initial designs: $X_o = 1$ (carbon fiber wing), $X_o = 0.5$, and $X_o = 0.1$. A pure membrane wing ($X_o = 0$) cannot be considered for the reasons discussed above.

Six objective functions are considered: maximum lift, minimum drag, maximum L/D, maximum $C_{L\alpha}$, minimum $C_{L\alpha}$, and minimum $C_{m\alpha}$. Flight speed is kept constant at 13 m/s, but both 3º and 12º angles of attack are considered, with a $\Delta\alpha$ of 1º for finite differences. Both the reflex airfoil seen in Figure 5-16 and a singly-curved airfoil are used, though aspect ratio, planform, and peak camber are unchanged. The stiffness of the carbon fiber laminates is as computed by Figure 4-3, and the pre-stress of the membrane is fixed in both the chordwise and spanwise directions at 7 N/m. No correction is applied to the free trailing edge, as such a computation would render the pre-stress in this location very small, leading to unbounded behavior of the linear membrane model. The circular radius r_{min} for the mesh-independent filter is fixed at 4% of the chord.

Single-Objective Optimization

A typical convergence history of the aeroelastic topology optimizer can be seen in Figure 7-5, for a reflex wing at 3º angle of attack, with a maximum L/D objective function. The initial guess is an intermediate density of 0.5. Within 4 iterations, the optimizer has removed all of the carbon fiber adjacent to the root of the wing, with the exception of the region located at three-quarters of the chord, which corresponds to the inflection point of the reflex airfoil. The material

towards the leading edge and at the wing tip is also removed. Further iterations see topological changes characterized by intersecting threads of membrane material that grow across the surface, leaving behind "islands" of carbon fiber. These structures aren't connected to the laminate wing, but are imbedded within the membrane skin.

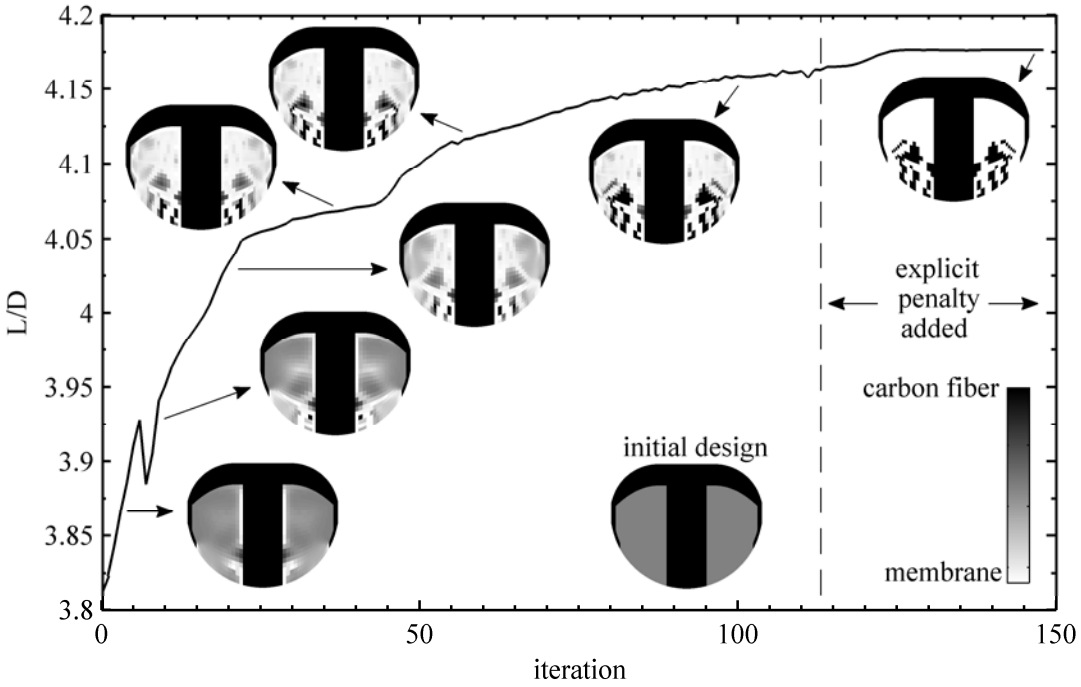

Figure 7-5. Convergence history for maximizing L/D, $\alpha = 3°$, reflex wing.

These results indicate two fundamental differences between the designs in Figure 7-1 and those computed via aeroelastic topology optimization. The first is the presence of "islands"; these designs can be built, but the process is significantly more complicated than with a monolithic wing skeleton. Such structures could be avoided with a manufacturability constraint/objective function (such as discussed by Lyu and Saitu [161]), but the logistics of such a metric (as above, with the trailing edge reinforcement constraint) are difficult to formulate. Furthermore, the aeroelastic advantages of free-floating laminate structures are significant, as will be discussed below. A second difference is the fact that the designs of Figure 7-1 are composed entirely from thin strips of carbon fiber embedded within the membrane, while the

topology optimization is apt to utilize two-dimensional laminate structures.

After 112 iterations in Figure 7-5, the optimization has largely converged (with only minimal further improvements in L/D), but some material with intermediate densities remains towards the leading edge of the wing. Many techniques exist for effectively interpreting gray level topologies [162]; the explicit penalty of Eq. (7-2) is used here. Surprisingly, the L/D sees a further increase with the addition of this penalty, contrary to the conflict between performance and 0-1 convergence reported by Chen and Wu [158]. The explicit penalty does not significantly alter the topology, but merely forces all of the design variables to their limits, as intended.

The final wing skeleton has three trailing edge battens (one of which is connected to a triangular structure towards the center of the membrane skin), and a fourth batten oriented at 45º to the flow direction. The structure shows some similarities to a wing design in Figure 7-1 (third row, first column), and appears to be a topological combination of a BR and a PR wing, with both battens and membrane inflation towards the leading edge. The optimized topology increases the L/D by 9.5% over the initial design, and (perhaps more relevant, as the initial intermediate density design does not technically exist) by 10.2% over the rigid wing.

The affect of mesh density is given in Figure 7-6, for a reflex wing at 12º angle of attack, with L/D maximization as the objective function. The 30x30 grid, for example, indicates that 900 vortex panels (and 1800 finite elements) cover each semi-wing. As the leading edge, root, and wing tip of each wing are fixed as carbon fiber, 480 density design variables are left for the topology optimization. One obvious sign of adequate convergence is the efficiency of the rigid wing, with only a 0.44% difference between that computed on the two finer grids. The three optimal wing topologies are similar, with three distinct carbon fiber structures imbedded within the membrane skin: two extend to the trailing edge and the third resides towards the leading

edge. While the 20x20 grid is certainly too coarse to adequately resolve the geometries of interest, the topology computed on the 30x30 grid is very similar to that computed on the 40x40 grid. The computational cost of each optimization iteration upon the coarser grid is 5 times less than that seen for a 40x40 grid, and will be used for the remainder of this work.

20x20, L/D = 4.61
L/D_{rigid} = 4.54

30x30, L/D = 4.58
L/D_{rigid} = 4.49

40x40, L/D = 4.55
L/D_{rigid} = 4.47

Figure 7-6. Affect of mesh density upon optimal L/D topology, $\alpha = 12^{o}$, reflex wing.

The affect of the initial starting design is given in Figure 7-7, for a reflex wing at 12º angle of attack, with drag minimization as the objective function. As mentioned above, $X_o = 1$ (carbon fiber wing), $X_o = 0.5$, and $X_o = 0.1$ are all considered. The three final optimal topologies are very different, indicating a large dependency upon the initial guess and no guarantee that a global optimum has been located. Nevertheless, the indicated improvements in drag are promising, with a potential 6.7% decrease from the rigid wing. As expected, the denser the initial topology, the denser the final optimized topology.

All three wing topologies utilize some form of adaptive washout for load and drag alleviation. The structures must be flexible enough to generate sufficient nose-down rotation of each wing section, but not so flexible that the membrane areas of the wing will inflate and camber, increasing the forces. The wing structure in the center of Figure 7-7 (with $X_o = 0.5$) strikes the best compromise between the two deformations, and provides the lowest drag. When $X_o = 1$, the structure is too stiff, relying upon a membrane hinge between the carbon fiber wing

and root. When $X_o = 0.1$, the optimizer is unable to fill in enough space with laminates to prevent membrane inflation. Of the three designs, this is the least tractable from a manufacturing point of view as well.

$X_o = 1$, $C_D = 0.131$ $X_o = 0.5$, $C_D = 0.125$ $X_o = 0.1$, $C_D = 0.128$

$C_{D,rigid} = 0.134$

Figure 7-7. Affect of initial design upon the optimal C_D topology, $\alpha = 12^o$, reflex wing.

The dependency of the optimal topology (maximum lift) upon both angle of attack and airfoil shape are given in Figure 7-8, for both a reflex (left two plots) and a cambered wing (right two plots). For the wing with trailing edge reflex, the optimal lift design looks similar to that found in Figure 7-5: trailing edge battens that extend no farther up the wing than the half-chord, a spanwise member that coincides with the inflection point of the airfoil, and unconstrained membrane skin towards the leading edge, where the forces are largest. The optimizer has realized that it can maximize lift by both cambering the wing through inflation at the leading edge, and forcing the trailing edge battens downward for wash-in.

This latter deformation is only possible due to the reflex (negative camber) in this area, included to offset the nose-down pitching moment of the remainder of the "flying wing", and thus allow for removal of a horizontal stabilizer due to size restrictions. Increasing the angle of attack from 3º to 12º shows no significant difference in the wing topology, slightly increasing the length of the largest batten. At the lower angle of attack, up to 22% increase in lift is indicated through topology optimization.

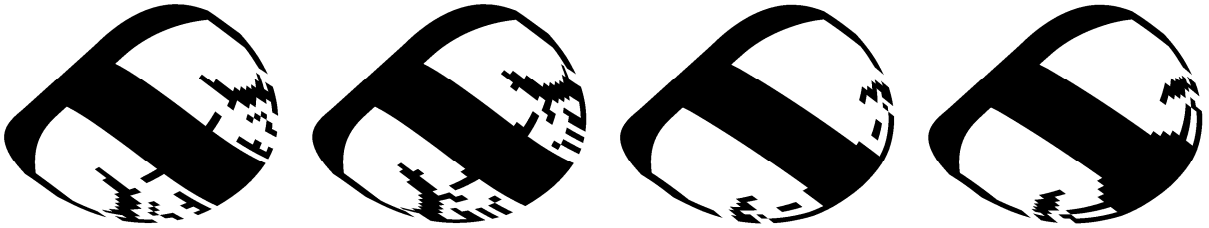

$\alpha = 3°$, $C_L = 0.312$ | $\alpha = 12°$, $C_L = 0.675$ | $\alpha = 3°$, $C_L = 0.561$ | $\alpha = 12°$, $C_L = 0.947$

$C_{L,rigid} = 0.254$ | $C_{L,rigid} = 0.604$ | $C_{L,rigid} = 0.487$ | $C_{L,rigid} = 0.842$

Figure 7-8. Affect of angle of attack and airfoil upon the optimal C_L topology.

For the cambered wing (singly-curved airfoil, right two plots of Figure 7-8), the lift over the rigid wing is, as expected, much larger than found in the reflex wings, but adequate stability becomes critical. With the removal of the negatively-cambered portion of the airfoil, most of the forces generated over this wing will be positive, and the topology optimizer can no longer gain additional lift via wash-in. Imbedding batten structures in the trailing edge will now result in washout, surely decreasing the lift. As such, the optimizer produces a trailing edge member that outlines the planform and connects to the root (similar to the perimeter-reinforced wing designs), restraining the motion of the trailing edge and inducing an aerodynamic twist.

Unlike the PR wing, this trailing edge reinforcement does not extend continuously from the root to the tip, instead ending at 65% of the semi-span. This is then followed by a trailing edge batten that extends into the membrane skin, similar to the designs seen for the reflex wing in Figure 7-8. Why such a configuration should be preferred over the PR wing design for lift enhancement will be discussed below. As before, increasing the angle of attack has little bearing on the optimal topology, again increasing the size of the trailing edge batten. A potential increase in lift by 15% over the rigid wing is indicated at the lower angle of attack.

Similar results are given in Figure 7-9, with L/D maximization as the topology design metric. Presumably due to the conflictive nature of the ratio, the wing topology that maximizes L/D is a strong function of angle of attack. For the reflex wing at lower angles, the optimal

design resembles topologies used above for lift enhancement (Figure 7-8), while at 12º the design is closer in topology to one with minimum drag (Figure 7-7). Increasing lift is more important to L/D at lower angles, while decreasing drag becomes key at larger angles. The drag is very small at low angles of attack (technically zero for this inviscid formulation, if not for the inclusion of a constant $C_{Do)}$, and insensitive to changes via aeroelasticity.

This concept is less true for the cambered wing (right two plots of Figure 7-9), where designs at both 3º and 12º angle of attack utilize a structure with trailing edge adaptive washout. At the lower angle, the topology optimizer leaves a large triangular structure at the trailing edge (connected to neither the root nor the wing tip), and the leading edge is filled in with carbon fiber. At the higher angle of attack, four batten-like structures are placed within the membrane skin, oriented parallel to the flow, one of which connects to the wing tip. Potential improvements are generally smaller than those seen above, though a 10% increase in L/D is available for the cambered wing at 12º.

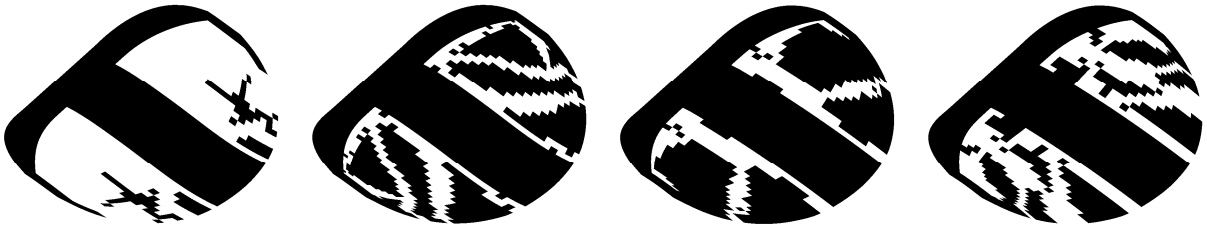

$\alpha = 3°$, L/D = 4.18
$L/D_{rigid} = 3.78$

$\alpha = 12°$, L/D = 4.58
$L/D_{rigid} = 4.49$

$\alpha = 3°$, L/D = 4.78
$L/D_{rigid} = 4.70$

$\alpha = 12°$, L/D = 4.41
$L/D_{rigid} = 4.01$

Figure 7-9. Affect of angle of attack and airfoil upon the optimal L/D topology.

Wing displacements and pressure distributions are given for select wing designs in Figure 7-10, for a reflex wing at 12º angle of attack. Corresponding data along the spanwise section 2y/b = 0.58 is given in Figure 7-11. As the wing is modeled with no thickness in the vortex lattice method, distinct upper and lower pressure distributions are not available, only differential terms. Five topologies are discussed, beginning with a pure carbon fiber wing. Lift-

augmentation designs are represented by a baseline PR wing and the topology optimized for maximum lift. Lift-alleviation designs are represented by a baseline BR wing and the topology optimized for minimum lift slope.

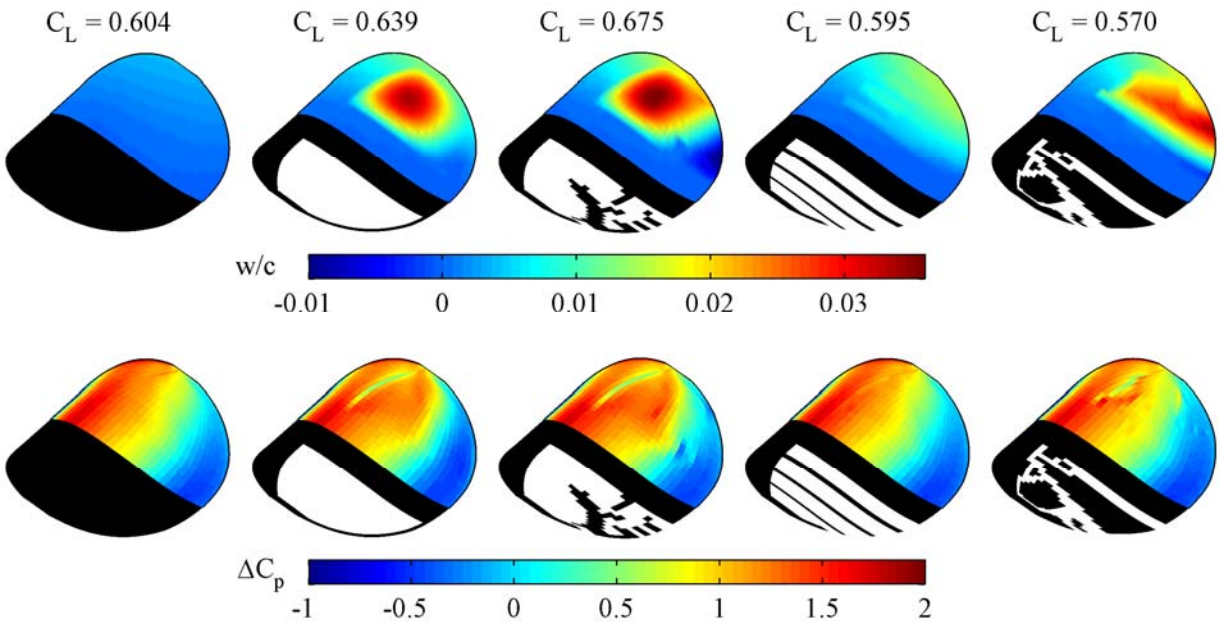

Figure 7-10. Normalized out-of-plane displacements (top) and differential pressure coefficients (bottom) for baseline and optimal topology designs, $\alpha = 12^o$, reflex wing.

The differential pressure distribution over the rigid wing is largely similar to that computed with the Navier-Stokes solver in Figure 5-18 and Figure 5-19: leading edge suction due to flow stagnation, pressure recovery (and peak lift) over the camber, and negative forces over the reflex portion of the wing. As expected, the inviscid solver misses the low-pressure cells at the wingtip (from the vortex swirling system [3]), and the plateau in the pressure distribution, indicative of a separation bubble [27]. This aerodynamic loading causes a moderate wash-in of the carbon fiber wing (0.1º), resulting in a computed lift coefficient of 0.604.

Computed deformation of the PR wing is likewise similar to that found above (Figure 5-5), though the deformations are smaller, within the range of validity of the linear finite element solver. The sudden changes in wing geometry at the membrane/carbon fiber interfaces lead to

sharp downward forces at the leading and trailing edges, the latter of which exacerbates the effect of the airfoil reflex. Despite this, the membrane inflation increases the camber of the wing and thus the lift, by 6.5% over the rigid wing.

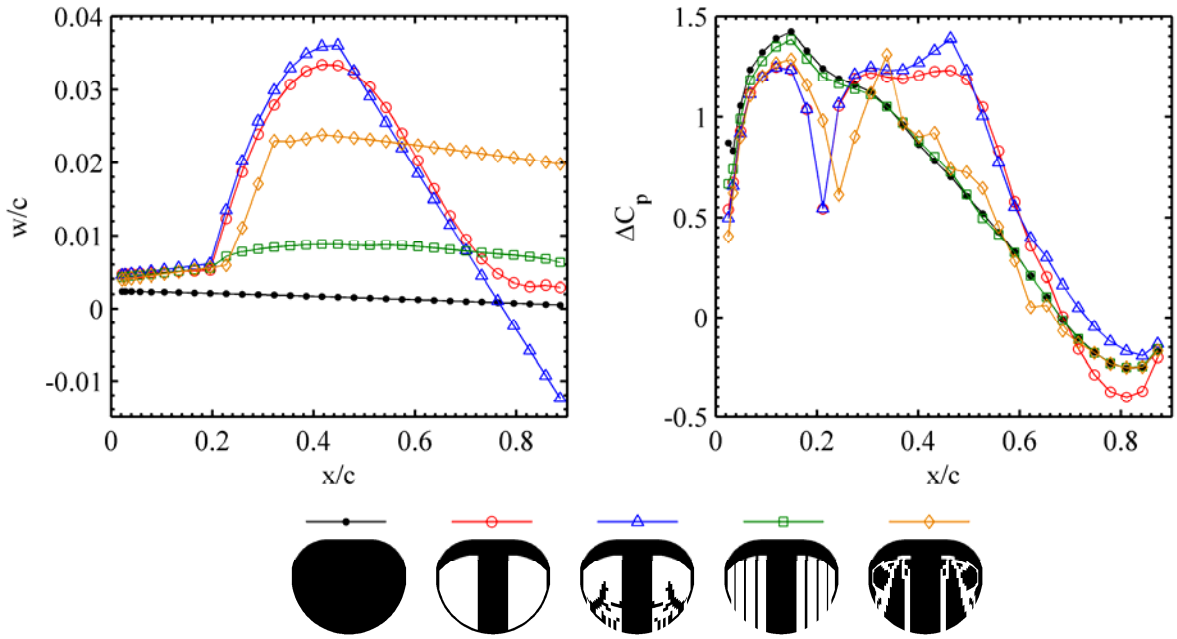

Figure 7-11. Deformations and pressures along 2y/b = 0.58 for baseline and optimal topology designs, α = 12º, reflex wing.

As discussed above, several disparate deformation mechanisms contribute to the high lift of the MAV design located by the aeroelastic topology optimizer (middle column, Figure 7-10). First, the membrane inflation towards the leading edge increases lift via cambering, similar to the PR wing (the pressure distributions over the two wing structures are identical through x/c = 0.25). The main trailing edge batten structure is then depressed downward along the trailing edge (due to the reflex) for wash-in, while the forward portion of this structure is pushed upwards. This structure essentially swivels about the inflection point of the wing's airfoil, a deformation which is able to further increase the size of the membrane cambering, and is only possible because the laminate is free-floating within the membrane skin. It can also be seen (from the left side of Figure 7-11 in particular) that the local bending/twisting of this batten

structure is minimal: the deformation along this structure is largely linear down the wing. The intersection of this linear trend with the curved inflated membrane shape produces a cusp in the airfoil. The small radius of curvature forces very large velocities, resulting in the lift spike at 46% of the chord.

This combination of wash-in and cambering leads to a design which out-performs the lift of the PR wing by 5.6%, but the former effect is troubling. The wash-in essentially removes the reflex from the airfoil (as does the aerodynamic twist of the PR wing), an attribute originally added to mitigate the nose-down pitching moment. This fact leads to two important ideas. First, thorough optimization of a single design metric is ill-advised for micro air vehicle design, as other aspects of the flight performance will surely degrade. Its inclusion here is only meant to emphasize the relationship between aeroelastic deformation and flight performance, and show the capabilities of the topology optimization. A better approach is the multi-objective scheme discussed below.

Secondly, if the design goal is a single-minded maximization of lift, a reflex airfoil is a poor choice compared to a singly-curved airfoil, a shape which the topology optimizer strives to emulate through aeroelastic deformations. Furthermore, if the design metric is an aerodynamic force or moment, passive shape adaptations need not be used at all: simply compute the optimal wing shape from the bottom row of Figure 7-10, and build a similar rigid wing. Mass restrictions prevents such a strategy in traditional aircraft design (though a similar idea can be seen in the jig-shape approach [163], where wing shape is optimized, followed by identification of the internal structure which allows for deformation into this shape), but two layers of carbon fiber can adequately hold the intended shape without a stringent weight penalty. However, if the design metric is an aerodynamic derivative (gust rejection or longitudinal static stability, for

example), membrane structures must be used, as these metrics depend on passive shape adaptation with sudden changes in freestream, angle of attack, or control surface deflection.

Referring now to the load-alleviating MAV wing structures of Figure 7-10 and Figure 7-11, the deformation of the BR wing is relatively small, allowing for just 0.1° of adaptive washout. As discussed above, the BR wing is very sensitive to pre-tensions in the span direction (Figure 6-1); the structure is too stiff. Less than a 2% drop in lift from the rigid wing is obtained, and the pressure distributions of the two wings in Figure 7-11 are very similar. What load alleviation the BR wing does provide seems to be due to the membrane inflation from between the leading edge of the battens, and the concomitant flow deceleration over the tangent discontinuity, rather than the adaptive washout at the trailing edge.

The load alleviating design located by the topology optimizer (right column, Figure 7-10) is significantly more successful. By filling the design space with patches of disconnected carbon fiber structures (dominated by a long batten which extends the length of the membrane skin, but is not connected to the wing's laminate leading edge), the MAV wing is very flexible, but none of the membrane portions of the wing are large enough to camber the wing via inflation. Wing deformation is the same magnitude as that seen in the PR-type wings, but the motion is located at the trailing edge for adaptive washout, and lift is decreased by 5%. The local deformation within the membrane between the leading edge and the long batten structure is substantial, and the flow deceleration over this point sees a further loss in lift, as with the BR wing.

Similar results are given in Figure 7-12 and Figure 7-13, for a cambered wing at 12º angle of attack. The three baseline wings are again shown (carbon fiber wing, PR, and BR), as well as the designs located by the topology optimization to maximize lift and minimize lift slope. As the forces are generally larger for the cambered airfoil, the deformations have increased to 5% of the

root chord. The negative forces at the trailing edge of the airfoil are likewise absent. As before, the PR membrane wing effectively increases the lift over its carbon fiber counterpart through adaptive cambering, along with aerodynamic penalties from the shape discontinuities at the leading and trailing edge of the membrane skin.

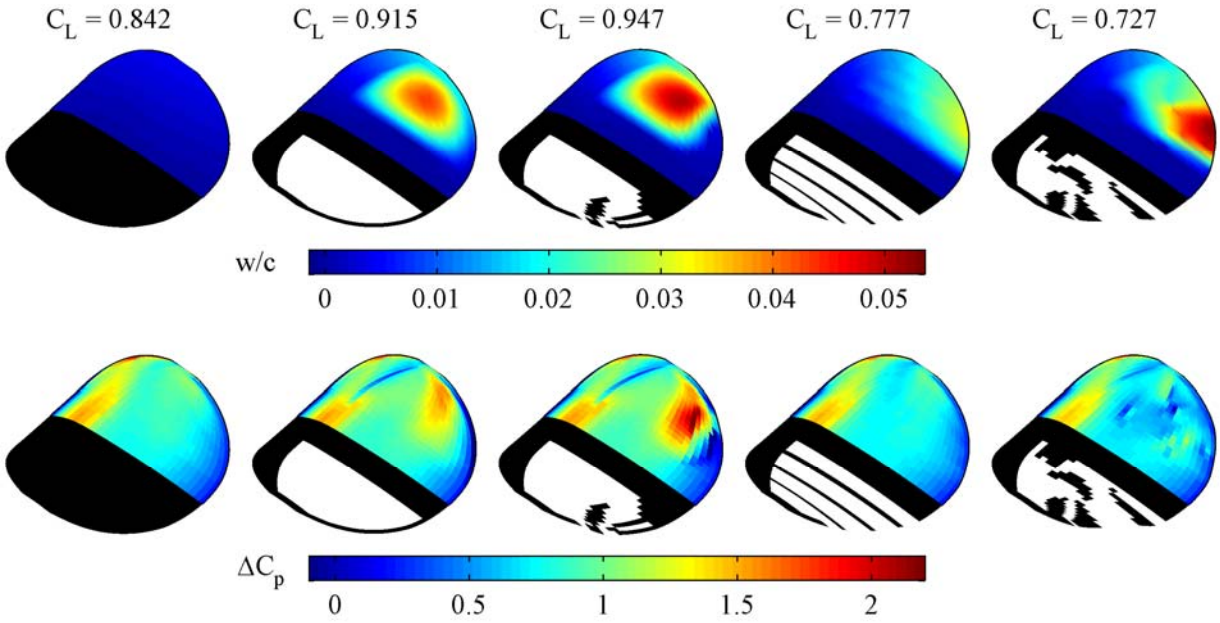

Figure 7-12. Normalized out-of-plane displacements (top) and differential pressure coefficients (bottom) for baseline and optimal topology designs, $\alpha = 12^o$, cambered wing.

There is an appreciable amount of upward deformation of the PR wing's trailing edge carbon fiber strip, leading to washout of each flexible wing section, degrading the lift. As such, the aeroelastic topology optimizer can maximize lift (Figure 7-12, middle column) by adding more material to this strip and negating the motion of the trailing edge. As discussed above, this strip does not continue unbroken to the wing tip, but ends at 65% of the semispan. The remaining membrane trailing edge is filled with a free-floating carbon fiber batten. Such a configuration can (theoretically) improve the lift in several ways, similar to the trailing edge structure used for lift optimization in Figure 7-10.

Placing a flexible membrane skin between two rigid supports produces a trade-off: the

cambering via inflation increases lift, but this metric is degraded by the sharp discontinuities in the airfoil shape. Towards the inner portion of the MAV wing, this trade-off is favorable for lift. Towards the wingtip however (either due to the changes in chord or in pressure) this is no longer true, and the topology optimizer has realized that overall lift can be increased by allowing this portion of the trailing edge to washout, thereby avoiding the negative pressures seen elsewhere along the trailing edge.

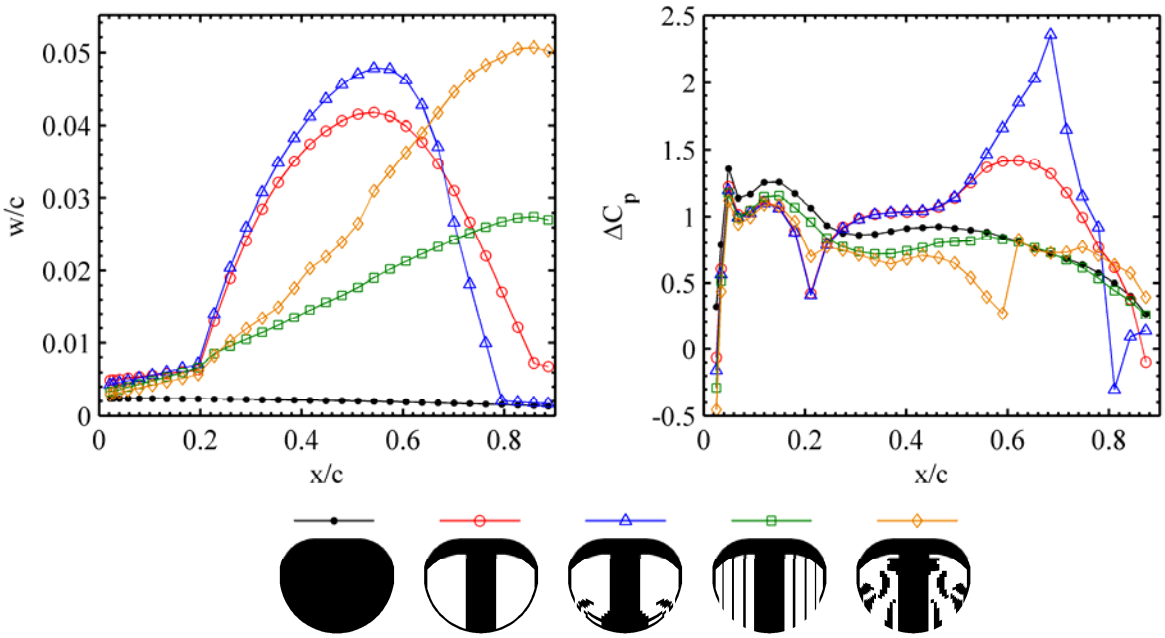

Figure 7-13. Deformations and pressures along 2y/b = 0.58 for baseline and optimal topology designs, α = 12º, cambered wing.

The forward portion of this batten structure also produces a cusp in the wing geometry, forcing a very strong low pressure spike over the upper portion of the airfoil, further increasing the lift, as before. Due to the inviscid formulation, further grid resolution around this cusp will cause the spike to grow larger, as the velocity around the small radius approaches infinity. The presence of viscosity will attenuate the speed of the flow, and thus both the magnitude of the low pressure spike and its beneficial effect upon lift. The aeroelastic topology optimizer predicts a 3.5% increase in lift over the PR wing, and 12.5% increase over the rigid wing, though the

veracity of the former beneficial comparison requires a viscous flow solver to ascertain the actual height of the low-pressure spike at x/c = 0.68.

The batten-reinforced design of Figure 7-12 is substantially more effective with the cambered wing, than with the reflex wing. As discussed above, reflex in the wing pushes the trailing edge down, limiting the ability of the battens to washout for load reduction. This can also be seen by comparing the airfoil shapes between Figure 7-13 and Figure 7-11: the cambered wing shows a continuous increase in the deformation from leading to trailing edge, while most of the deformation in the reflex wing is at the flexible membrane/carbon fiber interface. Aft of this point, deformation is relatively constant to the trailing edge.

The 1.6º of washout in the cambered BR wing decreases the load throughout most of the wing and decreases the lift by 8.5% (compared to the rigid wing), but, as before, the load-alleviating design located by the topology optimizer (right column, Figure 7-12) is superior. Similar to above, the design utilizes a series of disconnected carbon fiber structures, oriented parallel to the flow, and extending to the trailing edge. The structures are spaced far enough apart to allow for some local membrane inflation, but this cambering only increases the loads towards the trailing edge. The discontinuous wing surface forces a number of high-pressure spikes on the upper surface, notably at x/c = 0.2 and 0.6. This, in combination with the substantial adaptive washout at the trailing edge, decreases the lift by 13.6% over the rigid wing and by 5.6% over the BR wing.

Three of the wing topologies discussed above (minimum $C_{L\alpha}$, minimum drag, and minimum pitching moment slope, all optimized for a reflex wing at 3º angle of attack) are built and tested in the closed loop wing tunnel, as seen in Figure 7-14. Though the aeroelastic model relies on a sizable state of pre-stress in the membrane skin to remain bounded, all three of the

wings are constructed with a slack membrane. This is to ensure similarity between the three wings (pre-stress is very difficult to control), and also to compare the force and moment data to the baseline membrane data acquired above (Figure 5-12 - Figure 5-15).

Figure 7-14. Wing topology optimized for minimum $C_{L\alpha}$ built and tested in the wind tunnel.

Results are given in Figure 7-15, for a longitudinal α-sweep between 0º and 30º. All three structures located by the topology optimizer show marked improvements over the baseline experimental data, validating the use of a low fidelity aeroelastic model (vortex lattice model coupled to a linear membrane solver) as a surrogate for computationally-intensive nonlinear models. With the exception of very low (where deformations are small) and very high angles of attack (where the wing has stalled), the optimized designs consistently out-perform the baselines. As discussed above, this is not expected to be true for L/D, where design strategies vary strongly with incidence (Figure 7-9).

It should also be noted that the three optimized designs in Figure 7-15 provide shallower lift slopes, less drag, and steeper pitching moment slopes, respectively, than the experimental data gathered from the designs utilizing aeroelastic tailoring (Figure 6-15 - Figure 6-18). This confirms the idea that topology optimization can out-perform tailoring of the baseline MAV wings, as the former has a larger number of variables to work with. The two techniques need not be mutually exclusive: having located suitable wing topologies, the designs can be subjected to a

tailoring study for further benefit to the flight performance.

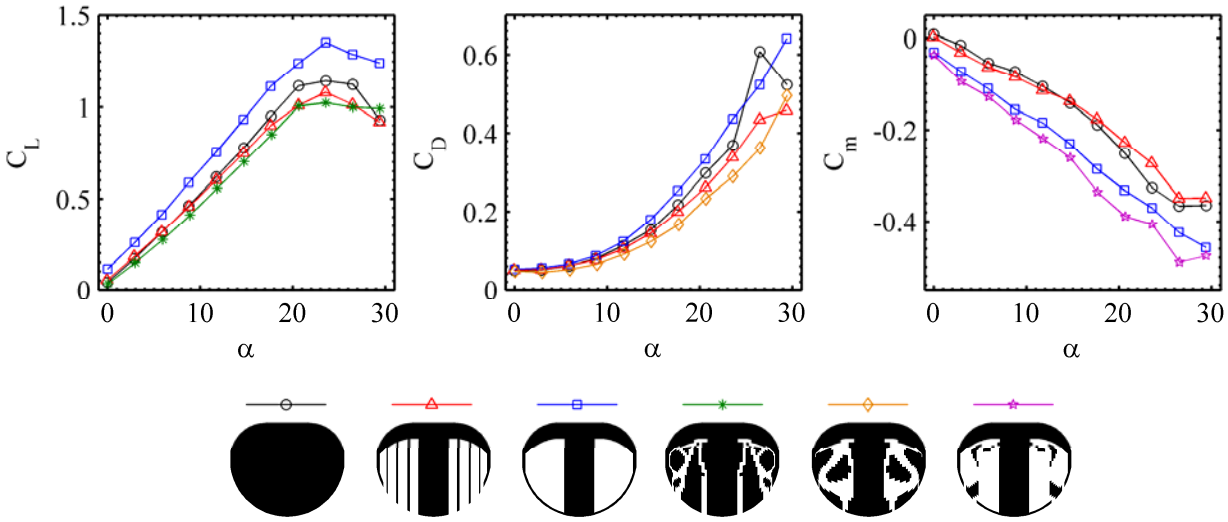

Figure 7-15. Experimentally measured forces and moments for baseline and optimal topology designs, reflex wing.

Multi-Objective Optimization

The need to simultaneously consider more than one design metric for aeroelastic topology optimization of MAV wings is demonstrated above: optimizing for lift prompts the algorithm to remove the reflex, by depressing the flexible trailing edge. The downward forces provided by the reflex offset the nose-down pitching moment of the remainder of wing, and are therefore essential for stability. Design and optimization with multiple performance criteria can be done my optimizing one variable with constraints upon the others (as discussed by Maute et al. [118] for aeroelastic topology optimization). For MAV design however, the formulation and bounds of these constraints are uncertain, and the method does not provide a clear picture of the inherent trade-off between variables.

The current work minimizes a convex combination of two objective functions (as discussed by Chen and Wu [158] for topology optimization). Successive optimizations with different relative weighting between the two metrics can fill out the Pareto optimal front. The

computational cost of such an undertaking is large, and adequate location of the front is not ensured for non-convex problems (such as seen in Figure 6-14). The objective function is now:

$$g = (1-\delta)\cdot\left(\frac{f_1 - f_{1,\min}}{f_{1,\max} - f_{1,\min}}\right) + \delta\cdot\left(\frac{f_2 - f_{2,\min}}{f_{2,\max} - f_{2,\min}}\right) \tag{7-16}$$

where δ is a weighting parameter that varies between 0 and 1, and f_1 and f_2 are the two objective functions of interest. These functions are properly normalized, with the minimum and maximum bounds computed from the single-objective optimizations (optimizing with δ set as 0 or 1). Eq. (7-16) is cast as a minimization problem, and the sign of f_1 and f_2 is set accordingly. As before, the objective function can be augmented with the explicit penalty of Eq. (7-2) as needed.

Typical convergence history results are given in Figure 7-16, for simultaneous maximization of L/D and minimization of the lift slope. The weighting parameter δ is set to 0.5, for an equal convex combination of the two variables. The values given for $C_{L\alpha}$ (~ 0.4) are smaller than experimentally measured trends (~ 0.5, from Table 5-1), as the inviscid solver is unable to predict the vortex lift from the tip vortex swirling system [27]. Beginning with an intermediate density ($X_o = 0.5$), the optimizer is able to decrease the convex combination (g) from 0.7 to 0.3, using similar techniques seen above. All of the carbon fiber material adjacent to the root, leading edge, and wingtip is removed. Intersecting streams of membrane material grow across the wing, leaving behind disconnected carbon fiber structures.

The lift-to-drag ratio monotonically converges after 25 iterations, while the lift slope requires 70 iterations to converge to a minimum value. An explicit penalty on intermediate densities is employed at the 80 iteration mark, providing a moderate decrease in the combination objective function. The lift-to-drag ratio is improved as well through the penalty, though the lift slope suffers. As before, the penalty only serves to force the density variables to 0 or 1, and does not significantly alter the wing topology.

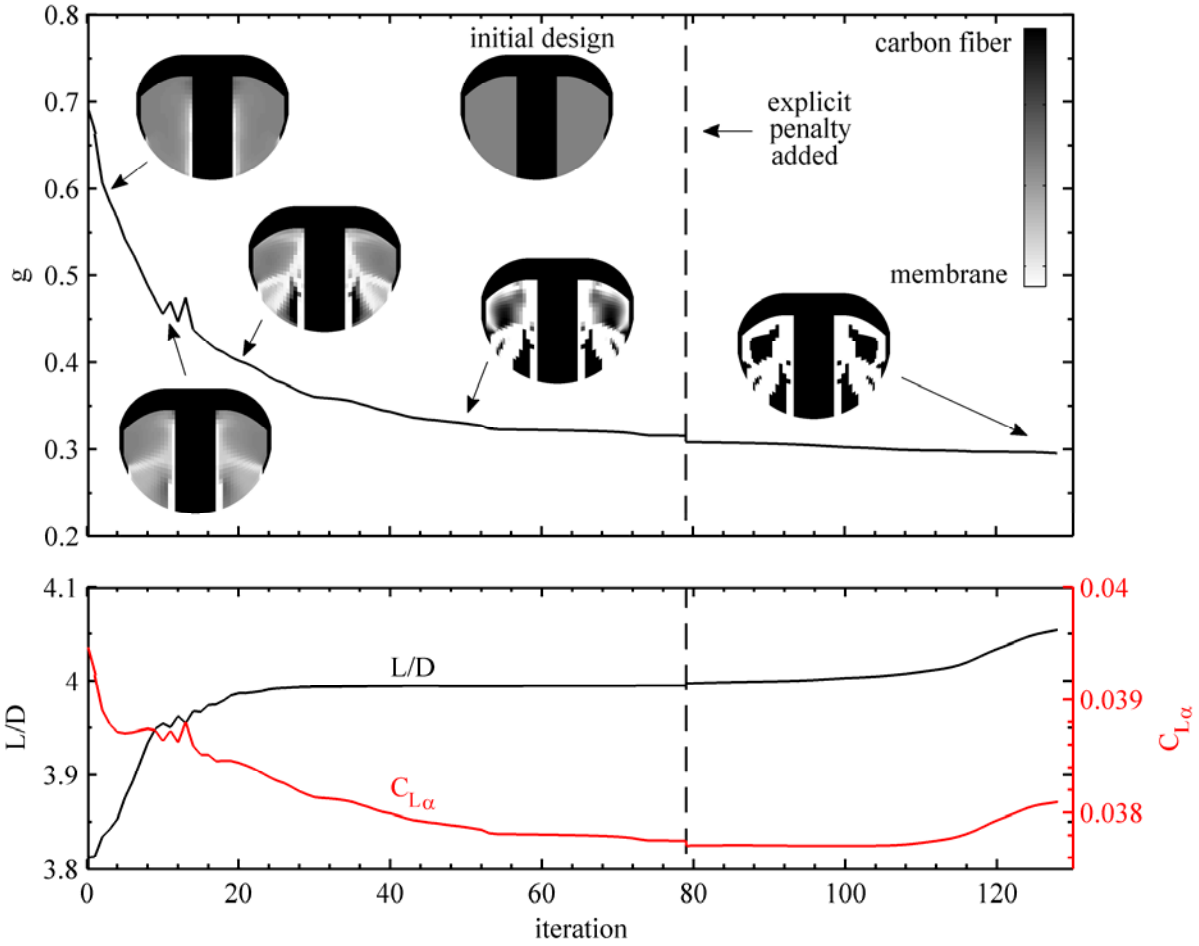

Figure 7-16. Convergence history for maximizing L/D and minimizing $C_{L\alpha}$, $\delta = 0.5$, $\alpha = 3°$, reflex wing.

The multi-objective results of Figure 7-16 can be directly compared to the single-objective results of Figure 7-5, where only L/D must be improved. For the latter, L/D can be increased to 4.17, with the inclusion of trailing edge battens for adaptive wash-in, and an unconstrained membrane skin towards the leading edge for cambering via inflation. This is a load-augmenting design, and as such the lift slope is very high: 0.040. In order to strike an adequate compromise between the two designs, the multi-objective optimizer leaves the trailing edge battens, but fills the membrane skin at the leading edge with a disconnected carbon fiber structure. The L/D of this design obviously degrades (4.05), but the lift slope is much shallower (0.038), as desired.

The Pareto front for this same trade-off (maximum L/D and minimum $C_{L\alpha}$) is given in

Figure 7-17, along with the performance of the 20 baseline MAV wing designs (Figure 7-1), and the design located by the single-objective topology optimizer to maximize $C_{L\alpha}$. All results are for a reflex wing at 3º angle of attack. Focusing first on the baseline wings, the BR and PR wings represent the extremes of the group in terms of lift slope, as expected. The homogenous carbon fiber wing has the lowest L/D (implying that for a reflex wing at this flight condition, any aeroelastic deformation will improve efficiency, regardless of the type), while a MAV design with 2 trailing edge battens as the largest L/D.

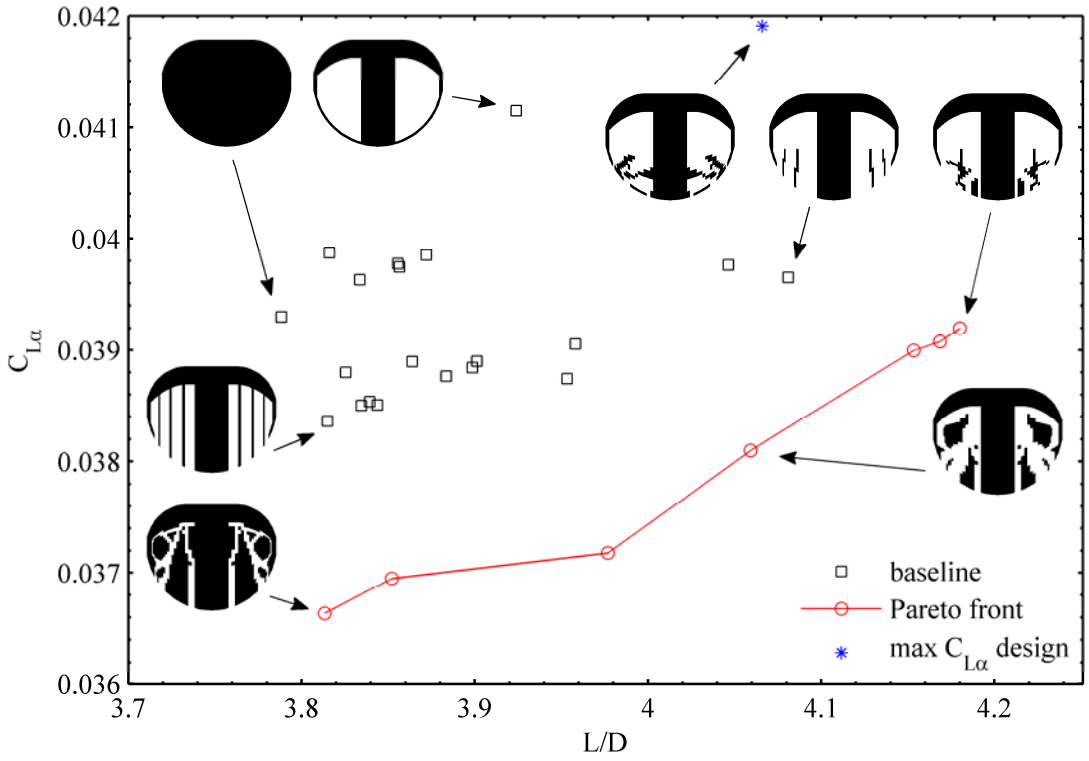

Figure 7-17. Trade-off between efficiency and lift slope, $\alpha = 3º$, reflex wing.

The aeroelastic topology optimization produces a set of designs that significantly out-perform the baselines, in terms of individually-considered metrics (maximum and minimum lift slope, maximum L/D), and multiple objectives: all of the baselines are removed from the computed Pareto front. The optimized designs lay consistency closer to the fictional utopia point as well , which for Figure 7-17 is at (4.18, 0.0366). The entirety of the Pareto front is not

convex, but the topology optimizer is still able to adequately compute it. The data points are not evenly spaced either, with $\delta = 0.4$ and 0.2 both very close to the solution with optimal L/D ($\delta = 0$). This would suggest that despite the normalizing efforts, maximizing L/D carries greater weight than minimizing the lift slope, an imbalance which may be remedied through nonlinear weighting [111]. The results of Figure 7-16 also indicate that using an explicit penalty to force the design to a 0-1 density distribution favors L/D, but not $C_{L\alpha}$.

In terms of the two metrics in Figure 7-17, none of the designs along the Pareto optimal front are technically superior: they are non-dominated, in that no other design exists within the data set that out-performs another design in both metrics. Other performance indices, not included in the optimization, can then be used to select an adequate design. For micro air vehicle applications, payload, flight duration, or agility/control metrics can be used, as discussed by Torres [3]. Realistic knowledge of the low-fidelity aeroelastic model's limitations (the perceived superiority of an unconstrained membrane wing in Figure 7-3 is destroyed by large nonlinear flapping vibrations [62], for example), or manufacturability [161] may also be used to select a design. It should also be noted that at higher angles of attack, the trade-off between high efficiency and low lift slopes does not exist. As discussed (Figure 7-9), increasing the incidence promotes an aeroelastic structure with streamlining to improve L/D, a deformation that will also decrease the lift slope.

Wing displacements and pressure distributions for selected wings along the Pareto front of Figure 7-17 are given in Figure 7-18, for a reflex wing at 3º angle of attack. Corresponding data along the spanwise section $2y/b = 0.58$ is given in Figure 7-19. When $\delta = 1$ (single-objective optimization to minimize the lift slope), the aeroelastic topology optimizer locates a design with several disconnected structures imbedded within the membrane, including a long batten that

extends the length of the membrane skin. The wing is flexible enough to adaptively washout, but the remaining patches of membrane skin are not large enough to inflate and camber.

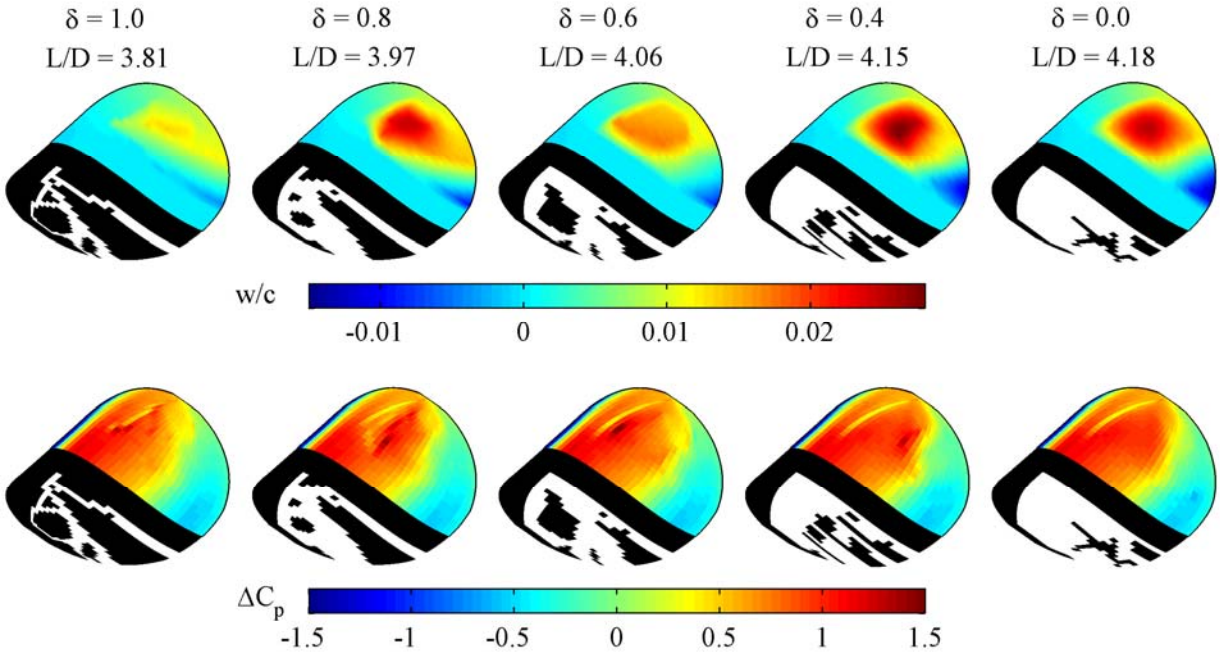

Figure 7-18. Normalized out-of-plane displacements (top) and differential pressure coefficients (bottom) for designs that trade-off between L/D and $C_{L\alpha}$, $\alpha = 3^{\circ}$, reflex wing.

Gradually adding weight to the L/D design metric removes the structures from the leading edge of the membrane skin, leaving batten-like structures at the trailing edge of the wing. The former transition allows the membrane to inflate and camber the wing, while the latter provides wash-in through depression of the trailing edge. The cambering membrane inflation does not grow monotonically with decreasing δ, but the trailing edge deformation does: from 0.25º of washout to 0.75º of wash-in. The size of the depressed trailing edge portion also grows in size. Decreasing δ shifts the lift penalty (pressure spike on the upper surface) forward towards the membrane/carbon fiber interface, and the lift spike (due to the surface geometry cusp at the leading edge of the batten structures) aft-ward. However, the design that maximizes L/D (δ = 0) has no spike, with a smooth pressure and displacement profile aft of the lift penalty towards the leading edge. This may be indicative of the detrimental effect the airfoil cusp has on drag.

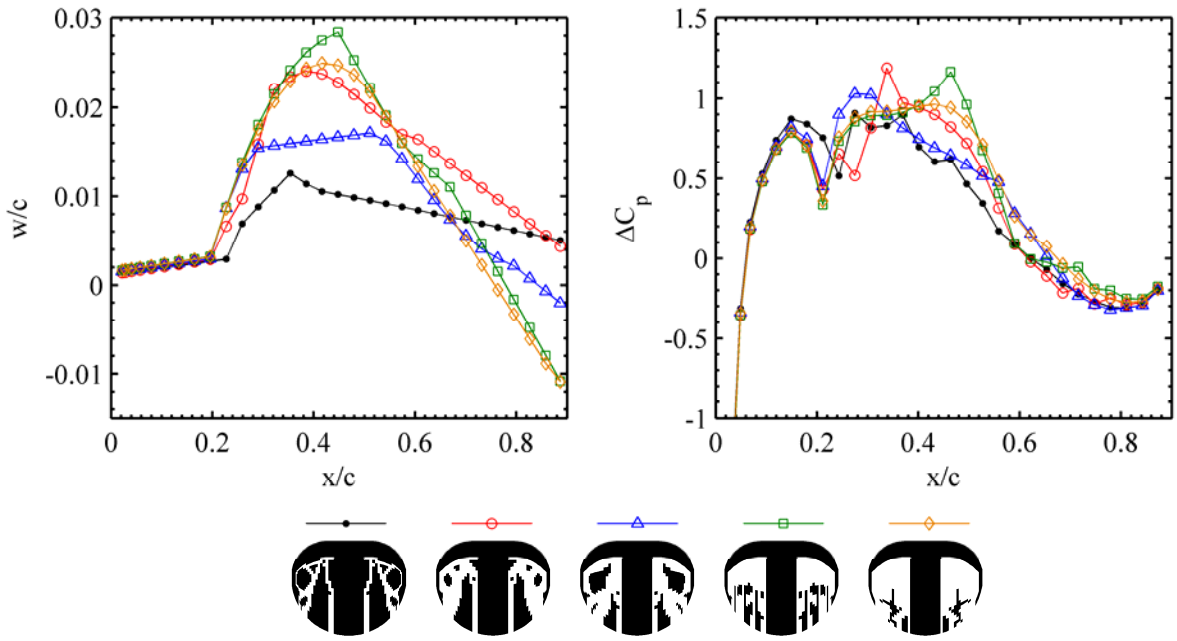

Figure 7-19. Deformations and pressures along 2y/b = 0.58 for designs that trade-off between L/D and $C_{L\alpha}$, $\alpha = 3^{\circ}$, reflex wing.

The trade-off between the drag and longitudinal static stability of a membrane MAV wing is very important: the latter is typically improved through large membrane inflations. The resulting tangent discontinuities in the wing surface produce pressure spikes oriented axially, and the exaggerated shape prompts the flow to separate above and below the membrane [14]. The trade-off is given in Figure 7-20 for a reflex wing at 12º, for both the 20 baseline designs and the Pareto front located with topology optimization. Compared with the data seen in Figure 7-17, the baseline designs at this higher angle of attack fail to adequately fill the design space; their performance generally falls within a band. The streamlining of the BR wing provides the lowest drag (of the baselines), but doesn't significantly out-perform the homogenous carbon fiber wing.

As expected, the PR wing has the largest static stability margin of the baselines, but the drag penalty is large (and probably under-predicted by the inviscid flow solver). The topology optimizer is able to locate a design with the same drag penalty, but a steeper pitching moment slope: by 5.6% over the PR wing. The baselines designs, in general, lie closer to the Pareto front

than seen in Figure 7-17, but the optimized designs are still superior in terms of Pareto optimality and individual metrics. The optimal drag design (3.8% less than the BR wing) begins with two carbon fiber structures imbedded within the membrane skin, one of which is a long batten that extends the length of the design domain.

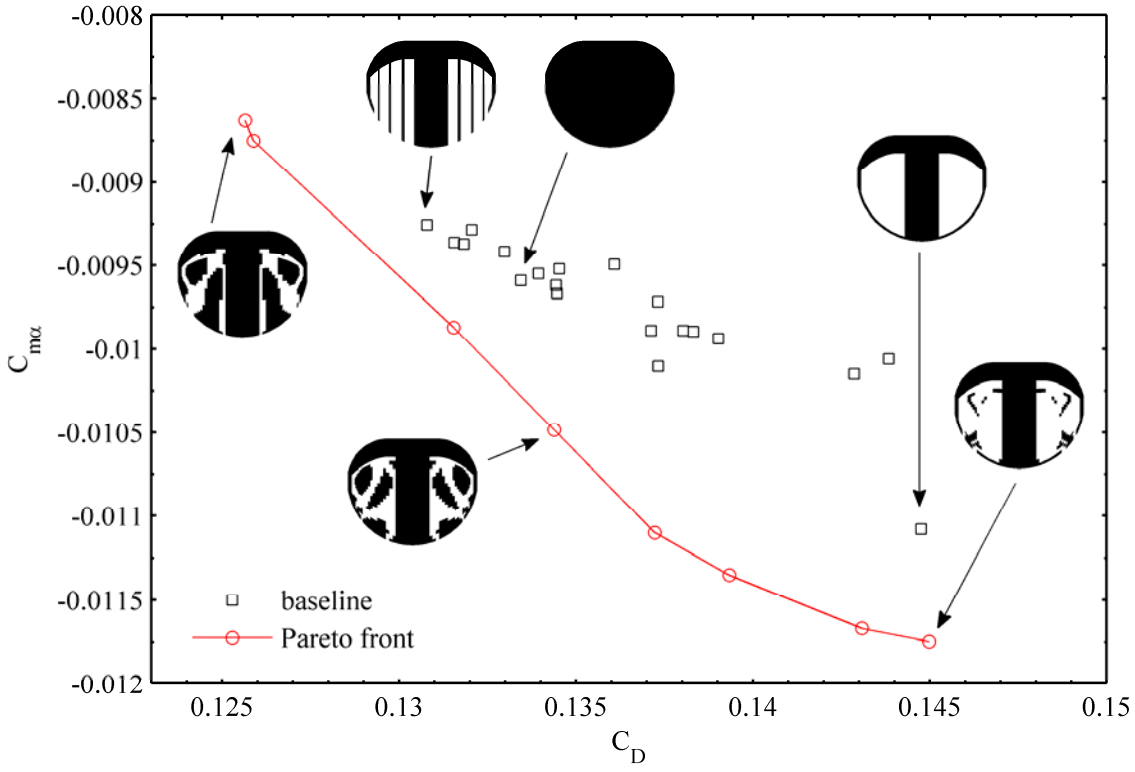

Figure 7-20. Trade-off between drag and pitching moment slope, $\alpha = 12^{o}$, reflex wing.

By adding weight to the static stability metric ($C_{m\alpha}$), this long batten breaks in two pieces; the foreword section shrinks into a slender batten imbedded in the leading edge of the membrane skin. The aft-ward section gradually accumulates along the trailing edge, merges with the root, and forms the trailing edge support. As discussed above, this reinforcement does not connect monolithically to the wingtip; this space is filled with a trailing edge batten. The superiority of this design is confirmed by the wind tunnel data of Figure 7-15. The Pareto optimal front of Figure 7-20 shows a more pronounced convexity than seen in Figure 7-17, though the data points are still not evenly spaced with δ.

Similar data is given in Figure 7-21, for the trade-off between maximum lift and minimum lift slope, for a cambered wing (no reflex) at 12° angle of attack. Such a trade-off is of interest because minimizing the lift slope of a membrane MAV wing, while an effective method for delaying the onset of stall or rejecting a sudden wind gust, typically decreases the pre-stall lift in steady flight as well; a potentially unacceptable consequence. Certain aeroelastic deformations, such as a passive wing de-cambering, would provide a wing with higher lift (than the baseline carbon fiber wing, for example), but a shallower lift slope.

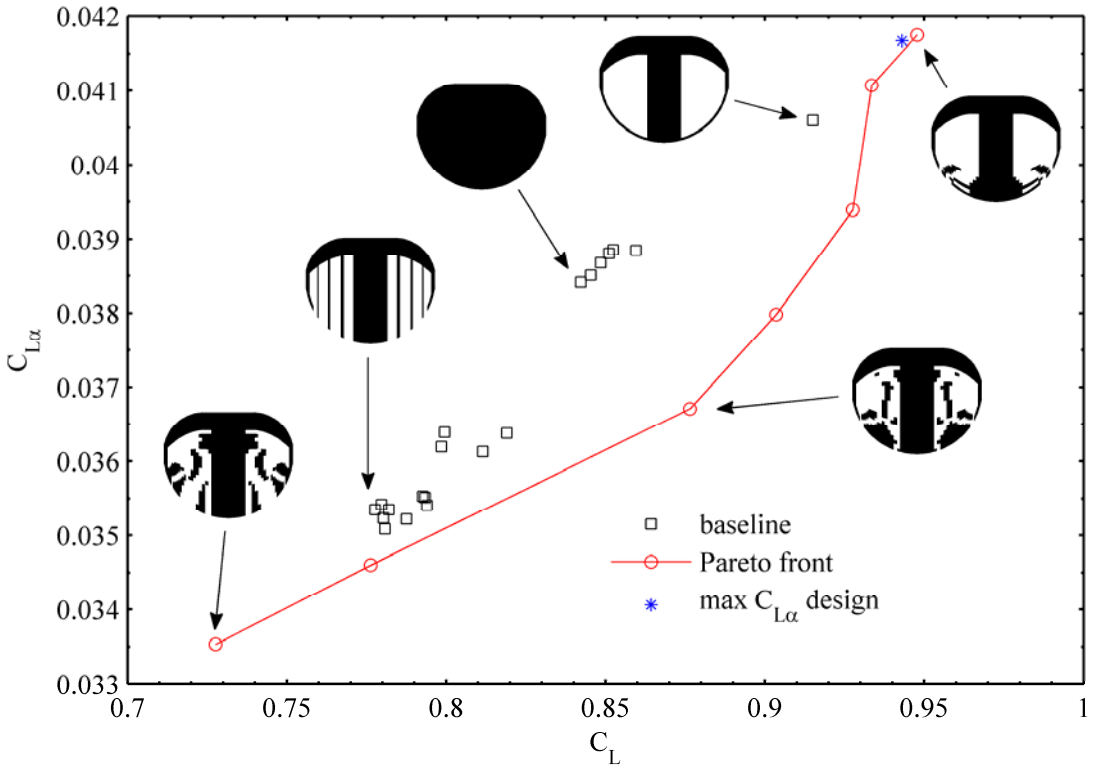

Figure 7-21. Trade-off between lift and lift slope, $\alpha = 12^o$, cambered wing.

Such a motion is unusual for low aspect ratio membrane structures however: none of the baseline designs have both larger lift and a smaller lift slope than the carbon fiber wing. The correlation between C_L and $C_{L\alpha}$ within the set of baseline designs is very strong, and all the designs fall very close to a single line, clustered in three groups. Any baseline design with adaptive washout (free trailing edge) has lift slopes between 0.035 and 0.037, any overly-stiff

design with battens oriented perpendicular to the flow (or the carbon fiber wing) has a slope between 0.038 and 0.039, and the PR wing has a lift slope of 0.041.

The strong data correlation is in sharp contrast to the results of Figure 7-17 for the reflex wing, where the baseline structures are well-distributed through the design space. This emphasizes the large role that the doubly-curved airfoil can play in producing many different types of aeroelastic deformation, providing greater freedom to the designer and better compromise designs. Despite this, the magnitude of the variability is higher for the cambered wing, as the forces are generally larger: $C_{L\alpha}$ can be varied by 14.5% for the reflex wing in Figure 7-17, but by 26.4% for the cambered wing in Figure 7-21. These numbers can be increased further with the use of nonlinear membrane structures, but deformations must be kept at a moderate level to preserve the fidelity of the linear finite element model in the current work.

As wing structures with high lift and shallow lift slopes are rare, the set of baseline designs lies close to the Pareto front in Figure 7-21. None are superior however, in terms of individual metrics or Pareto optimality. The designs located by the topology optimizer to maximize lift and maximize lift slope are almost identical, though disparate designs can be obtained with a reflex wing, as noted above. The PR wing is very effective for cambered wings at higher angles of attack, and lies close to these two optimums. The slight convexity in the Pareto front produces two designs with the sought-after higher lift and lower lift slope than the homogenous carbon fiber wing. The topology highlighted in Figure 7-21 increases the lift coefficient from 0.842 to 0.876 and decreases the lift slope from 0.038 to 0.036, and is found from an equal weighting of the two metrics ($\delta = 0.5$).

Wing displacements and pressure distributions for selected wings along the Pareto front of Figure 7-21 are given in Figure 7-22, for a cambered wing at 12º angle of attack. Corresponding

data along the spanwise section 2y/b = 0.58 is given in Figure 7-23. Shallow lift slopes are provided with a series of disconnected batten structures oriented parallel to the flow. As a weight for high lift is added to the objective function, a large carbon fiber region grows at the trailing edge, but is connected to either the root or the wing tip. This allows for both washout and membrane cambering, and produces the MAV design with higher lift and shallower lift slopes than the carbon fiber wing ($\delta = 0.5$). Further decrease in δ flattens the chord of the trailing edge structure and removes the disjointed battens at the leading edge, to maximize lift.

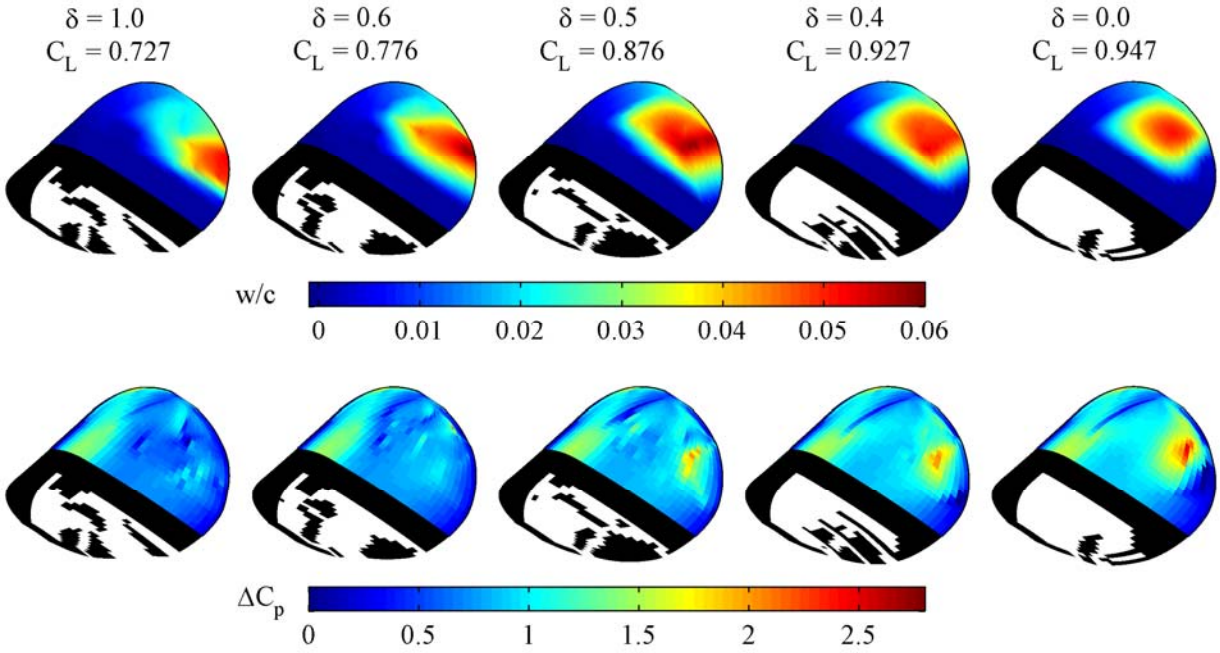

Figure 7-22. Normalized out-of-plane displacements (top) and differential pressure coefficients (bottom) for designs that trade-off between C_L and $C_{L\alpha}$, $\alpha = 12°$, cambered wing.

The locus of aeroelastic deformation clearly shifts from the trailing edge to the mid-chord of the wing as the structures produce higher lift. Washout monotonically decreases with δ (from 3° to 0.1° of wash-in). Membrane deformations are largest when $\delta = 0.5$, though the design that maximizes lift shows the largest change in camber, owing to the significant adaptive washout of the former, as discussed. Similarly, the aerodynamic penalty at the leading edge of the

membrane/carbon fiber interface is largest with the compromise design. The severity of the surface cusp (and the concomitant lift spike) increases with decreasing δ, emphasizing its usefulness as a lift-augmentation device. As discussed above, the severity of this spike is certainly over-predicted by the inviscid flow solver, though similar trends are seen using Navier-Stokes solvers for wings with tangent discontinuities Figure 5-21.

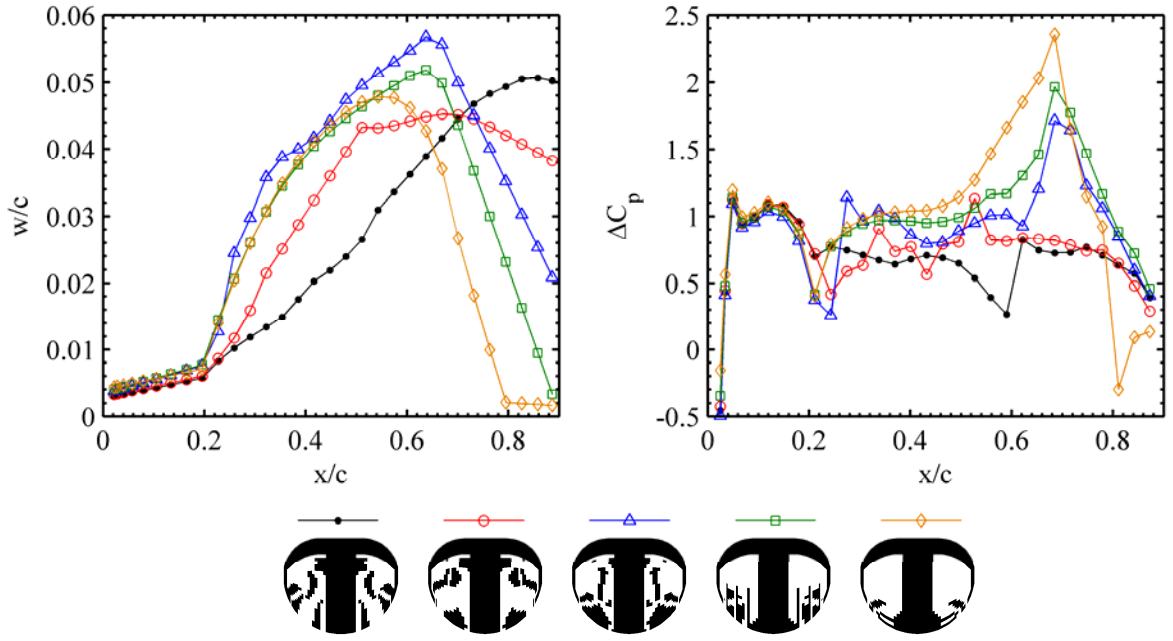

Figure 7-23. Deformations and pressures along 2y/b = 0.58 for designs that trade-off between C_L and $C_{L\alpha}$, α = 12º, cambered wing.

CHAPTER 8
CONCLUSIONS AND FUTURE WORK

The results given in this work detail a comprehensive research effort to understand and exploit the static aeroelasticity of membrane micro air vehicle wings. The flow structures of such wings are exceedingly complex, characterized by low Reynolds numbers (flow separation, laminar-turbulent transition, reattachment, vortex shedding, vortex pairing), low aspect ratios (strong tip vortex swirling, low pressure wing tip cells), and unstable interactions between the two (vortex destabilization for bilateral asymmetry). The wing's structural mechanics are also difficult to predict: a topologically-complex orthotropic wing shell is covered with a thin extensible latex skin, a membrane with an inherently nonlinear response.

Aeroelastic fixed membrane wing topologies can be broadly divided into two categories: load-alleviating, and load-augmenting. The former can use streamlining to reduce the drag, or adaptive washout for gust rejection, delayed stall, or attenuated maneuver loads. The latter increases the loads via adaptive cambering or wash-in, for improved lift and static stability; the wing may also be more response to pull-up maneuvers, etc. Wing topology is given by a distinct combination of stiff laminate composite members and a thin extensible rubber membrane sheet, similar to the skeletal structure of a bird wing, or the venation patterns of insect wings.

This work discusses aeroelastic analysis and optimization in three phases. First, given a set of wing topologies (a batten-reinforced design for adaptive geometric twist, a perimeter-reinforced design for adaptive aerodynamic twist, and a homogenous laminate wing), how does the membrane inflation affect the complex flow structures over the wing? Secondly, how can the various sizing and strength variables incorporated within the wing structures be tuned to improve flight performance, in terms of both individual metrics and compromise functions? Third, can these baseline wing topologies be improved upon? How does the distribution of laminate shells

throughout a membrane skin affect the aeroelastic response?

No model currently exists that can accurately predict such aeroelasticity (the three-dimensional transition is the biggest numerical hurdle), and so the current work utilizes a series of low-fidelity aeroelastic models for efficient movement through the design space: vortex lattice methods and laminar Navier-Stokes solvers are coupled to linear and nonlinear structural solvers, respectively (detailed in Chapter 4). Due to the lower-fidelity nature of the models (despite which, the computational cost of this coupled aeroelastic simulation is very large), experimental model validation is required. Such characterization is conducted in a low speed closed loop wind tunnel. Aerodynamic forces and moments are measured using a strain gage sting balance with an estimated resolution of 0.01 N. Structural displacement and strain measurements are made with a visual image correlation system; a calibrated camera system is mounted over the test section, as discussed in Chapter 3.

Chapter 5 provides a detailed analysis of the flow structures, wing deformation, and aerodynamic loads of a series of baseline membrane MAV wings. At small angles of attack, the low Reynolds number flow beneath a MAV wing separates across the leading edge camber, the flow over the upper surface is largely attached, and the tip-vortex swirling system is weak. The opposite is true has the incidence is increased: the bubble on the upper surface grows, eventually leading to stall. The lift curves of the low aspect ratio wings are typically shallow, with a large stalling angle. Low pressure cells deposited on the upper surface of the wing tip by the vortex swirling grow with angle of attack, adding nonlinearities to the lift and moment trends.

The structural deformation of a batten-reinforced wing has two main trends: the forces towards the leading edge are very large, and induce membrane inflation in-between the battens. This increases the camber over the wing, and thus the lift. A second trend comes from the free

trailing edge of the BR wing, which deflects upward for a nose-down twist, decreasing the wing lift. These two effects tend to offset for lower angles of attack, and the aerodynamics follow the rigid wing's very closely. At higher angles the adaptive washout dominates, decreasing the incidence of a wing section by as much as 5º and decreasing the slope of the wing's lift curve. Outside of the promise such a wing shows for gust rejection and benevolent stall, the data also indicates that the streamlining decreases drag.

The deformation of a perimeter-reinforced wing is characterized by adaptive aerodynamic twist: the membrane skin inflates, constrained at the leading and trailing edges by the stiff carbon fiber perimeter. Lift, drag, and pitching moments are consistently stronger than measured from the rigid and BR wings, as a result of the cambering motion. The slope of the pitching moment curve is considerably steeper, providing much-needed longitudinal static stability to a wing with severe space and weight constraints. The large drag penalty of the wing is partly due to a pressure spike at the tangent discontinuity between the inflated membrane and the carbon fiber, and partly due to the greater amount of separated flow over the PR wing. Interactions between the separated longitudinal flow and the wing tip vortices are clearly visible in the PR wing, possibly indicating a greater propensity for rolling instabilities. The stretching of the membrane skin in the PR wing is more two-dimensional without the restrictive presence of battens.

It is shown in Chapter 6, both numerically and experimentally, that unconventional aeroelastic tailoring can be used to improve MAV wing performance. The chordwise and spanwise membrane pre-tension, number of plain weave carbon fiber layers, laminate orientation, and batten thickness are all considered, with the first three variables identified as critical through a series of one-factor-at-a-time tests. Increasing stiffness is seen to tend aerodynamic behavior towards a rigid wing, thought many local optima exist and can be

exploited. A comprehensive numerical review of the design space is provided with a full factorial designed experiment of the three aforementioned variables. This data is then used to optimize six aerodynamic variables, as well as compromises between each. The six designs resulting from the single-objective optimizations are built and tested in the wind tunnel: five show improvements over the baseline designs, one has a similar response.

While the flexible wing structures have been shown to effectively alter the flow fields over a MAV wing, aeroelastic topology optimization (Chapter 7) can be used to improve on the shortcomings of the previously-considered baseline designs. Results are superior to those computed via tailoring, as the number of variables is much larger: the wing is discretized into a series of panels, each of which can be membrane or carbon fiber laminate. The computational cost is severe: hundreds of iterations are expected for convergence, and a sensitivity analysis of the coupled aeroelastic system must be conducted.

The optimization is able to identify a series of interesting designs, emphasizing the relationships between flight condition, airfoil, design metric, and wing topology. For load alleviation, the algorithm fills the membrane skin with a number of disconnected laminate structures. The structure is flexible enough to washout at the trailing edge, but the patches of exposed membrane skin are not large enough to inflate and camber the wing. Such a design has less drag and a shallower lift curve than the batten-reinforced wing. For load augmentation, the topology optimizer utilizes a combination of cambering, wash-in, and wing surface geometry cusps to increase the lift over the perimeter-reinforced wing. As a wing design optimized for a single metric is of minor usefulness, the topology optimizer is expanded to minimize a convex combination of two metrics for computation of the Pareto front. Three such designs are built and tested in the wind tunnel, confirming the computed superiority over the baseline wings.

Several future aeroelastic optimization studies are of interest. First, it is desired to upgrade the model fidelity used in the topology optimization described above. In order to limit computational cost, the work uses several linear modules: a vortex lattice solver and a linear stress-stiffening membrane solver, computed on a relatively coarse topology grid. Such a model is unable to capture several important nonlinearities, including flow separation and tip vortex formation. This can be remedied by using an unsteady Navier-Stokes solver coupled to a nonlinear membrane structural dynamics solver, increasing the computational cost by several orders of magnitude. The large number of variables (~1000) requires the use of a gradient-based optimizer; the higher-fidelity models will increase the complexities involved in the sensitivity analysis of the coupled aeroelastic system as well.

Of particular interest is gust response: how the membrane wing responds to a sinusoidal wind cycle, where it is desired to minimize the overall response for smoother flight. Objective functions may be the change in lift, integrated over the gust cycle. A second interest is the wing topology that delays the stall of the fixed wing. Conventional optimization formulations for this problem are difficult, as the stall angle is not a direct output from the aeroelastic system, but the angle at which the slope of the lift curve becomes negative. The optimizer will have to compute the lift at a set number of (large) angles of attack, and interpolate between the data points to estimate the stalling angle.

Secondly, these aeroelastic topology optimization techniques will be extended to flapping micro air vehicle wings. The structure of these wings is very similar to the fixed wings discussed above (thin membrane skins reinforced with laminate plies), and so the two-material model is appropriate. As with the gust cycle, lift and thrust will have to be computed over an entire flapping cycle, and then integrated to produce a scalar objective function. Furthermore, lift and

thrust will conflict: thrust relies on wing twist via deformation for thrust generation, while lift is dependent upon the leading edge vortex, which can be disrupted by excessive deformations.

This requires successive optimizations of a convex combination of the two weighted metrics to fill out the trade-off curve (assuming that this Pareto front is convex). The optimal design can then be selected from this front based upon metrics not considered in the formal optimization: trim requirements, manufacturability, etc. The flow structures that develop over flapping wing systems are very complicated, unsteady vortex driven flows. Navier-Stokes solvers can adequately handle these phenomena, but the computational cost may be prohibitive. Topology optimization of flapping wings may require lower-fidelity aerodynamic methods for effective navigation through the design space.

Finally, the aeroelastic topology optimization of both the fixed and flapping wings can be followed by a tailoring study for additional improvements to the flight performance. This is a standard optimization process: topology optimization, interpretation of the results to form an engineering design, followed by sizing and shape optimization (or in this case, tailoring). Both laminate thickness/orientation and membrane pre-tension can be used, as above. Membrane pre-tension is difficult to control however, and will relax at the un-reinforced borders of the wing, leading to a pre-tension gradient. Anisotropic membranes (through imbedded elastic fibers or crinkled/pleated geometries) are an attractive alternative for directional wing skin stiffness. The excess area of the skin may also be a useful variable. As the number of variables in a tailoring study is relatively small (~10), gradient-free global optimizers such as evolutionary algorithms or response surface techniques may become applicable.

REFERENCES

[1] Abdulrahim, M., Garcia, H., Lind, R., "Flight Characteristics of Shaping the Membrane Wing of a Micro Air Vehicle," *Journal of Aircraft*, Vol. 42, No. 1, 2005, pp. 131-137.

[2] Young, A., Horton, H, "Some Results of Investigation of Separation Bubbles," *AGARD Conference Proceedings*, No. 4, 1966, pp. 779-811.

[3] Torres, G., "Aerodynamics of Low Aspect Ratio Wings at Low Reynolds Numbers with Applications to Micro Air Vehicle Design," Ph.D. Dissertation, Department of Aerospace and Mechanical Engineering, University of Notre Dame, South Bend, IN, 2002.

[4] Shyy, W., Ifju, P., Viieru, D., "Membrane Wing-Based Micro Air Vehicles," *Applied Mechanics Reviews*, Vol. 58, No. 4, 2005, pp. 283-301.

[5] Hoerner, S., Borst, H., *Fluid-Dynamic Lift*, Hoerner Fluid Dynamics, Brick Town, NJ, 1975.

[6] Tang, J., Zhu, K., "Numerical and Experimental Study of Flow Structure of Low-Aspect Ratio Wing," *Journal of Aircraft*, Vol. 41, No. 5, 2004, pp. 1196-1201.

[7] Jenkins, D., Ifju, P., Abdulrahim, M., Olipra, S., "Assessment of the Controllability of Micro Air Vehicles," *Bristol International RPV/UAV Conference*, Bristol, UK, April 2-4, 2001.

[8] Lian, Y., Shyy, W., "Laminar-Turbulent Transition of a Low Reynolds Number Rigid or Flexible Airfoil," *AIAA Journal*, Vol. 45, No. 7, 2007, pp. 1501-1513.

[9] Albertani, R., Stanford, B., Hubner, J., Ifju, P., "Aerodynamic Coefficients and Deformation Measurements on Flexible Micro Air Vehicle Wings," *Experimental Mechanics*, Vol. 47, No. 5, 2007, pp. 625-635.

[10] Ifju, P., Jenkins, D., Ettinger, S., Lian, Y., Shyy, W., Waszak, M., "Flexible-Wing-Based Micro Air Vehicles," *Confederation of European Aerospace Societies Aerodynamics Conference*, London, UK, June 10-12, 2003.

[11] Shirk, M., Hertz, T., Weisshaar, T., "Aeroelastic Tailoring-Theory, Practice and Promise," *Journal of Aircraft*, Vol. 23, No. 1, 1986, pp. 6-18.

[12] Griffin, C., "Pressure Deflection Behavior of Candidate Materials for a Morphing Wing," Masters Thesis, Department of Mechanical and Aerospace Engineering, West Virginia University, Morgantown, WV, 2007.

[13] Waszak, M., Jenkins, L., Ifju, P., "Stability and Control Properties of an Aeroelastic Fixed Wing Micro Air Vehicle," *AIAA Atmospheric Flight Mechanics Conference and Exhibit*, Montreal, Canada, August 6-9, 2001.

[14] Stanford, B., Ifju, P., "Membrane Micro Air Vehicles with Adaptive Aerodynamic Twist: Numerical Modeling," *AIAA Structures, Structural Dynamics, and Materials Conference*, Honolulu, HI, April 23-26, 2007.

[15] Ormiston, R., "Theoretical and Experimental Aerodynamics of the Sail Wing," *Journal of Aircraft*, Vol. 8, No. 2, 1971, pp. 77-84.

[16] Bendsøe, M., Sigmund, O., *Topology Optimization*, Springer-Verlag, Berlin, Germany, 2003.

[17] Carmichael, B., "Low Reynolds Number Airfoil Survey," *NASA Contractor Report*, CR 165803, 1981.

[18] Lin, J., Pauley, L., "Low-Reynolds-Number Separation on an Airfoil," *AIAA Journal*, Vol. 34, No. 8, 1996, pp. 1570-1577.

[19] Mooney, M., "A Theory of Large Elastic Deformation," *Journal of Applied Physics*, Vol. 11, 1940, pp. 582-592.

[20] Dodbele, S., Plotkin, A., "Loss of Lift Due to Thickness for Low-Aspect-Ratio Wings in Incompressible Flow," *NASA Technical Report*, TR 54409, 1987.

[21] Gopalarathnam, A., Selig, M., "Low-Speed Natural-Laminar-Flow Airfoils: Case Study in Inverse Airfoil Design," *Journal of Aircraft*, Vol. 38, No. 1, 2001, pp. 57-63.

[22] Kellogg, M., Bowman, J., "Parametric Design Study of the Thickness of Airfoils at Reynolds Numbers from 60,000 to 150,000," *AIAA Aerospace Sciences Meeting and Exhibit*, Reno, NV, January 5-8, 2004.

[23] Laitone, E., "Wind Tunnel Tests of Wings at Reynolds Numbers Below 70,000," *Experiments in Fluids*, Vol. 23, No. 5, 1997, pp. 405-409.

[24] Mueller, T., "The Influence of Laminar Separation and Transition on Low Reynolds Number Airfoil Hysteresis," *Journal of Aircraft*, Vol. 22, No. 9, 1985, pp. 763-770.

[25] Gad-el-Hak, M., "Micro-Air-Vehicles: Can They be Controlled Better?" *Journal of Aircraft*, Vol. 38, No. 3, 2001, pp. 419-429.

[26] Shyy, W., Lian, Y., Tang, J., Viieru, D., Liu, H., *Aerodynamics of Low Reynolds Number Flyers*, Cambridge University Press, New York, NY, 2008.

[27] Katz, J., Plotkin, A., *Low-Speed Aerodynamics*, Cambridge University Press, Cambridge, UK, 2001.

[28] Lian, Y., Shyy, W., Viieru, D., Zhang, B., "Membrane Wing Mechanics for Micro Air Vehicles," *Progress in Aerospace Sciences*, Vol. 39, No. 6, 2003, pp. 425-465.

[29] Nagamatsu, H., "Low Reynolds Number Aerodynamic Characteristics of Low Drag NACA 63-208 Airfoil," *Journal of Aircraft*, Vol. 18, No. 10, 1981, pp. 833-837.

[30] Masad, J., Malik, M., "Link Between Flow Separation and Transition Onset," *AIAA Journal*, Vol. 33, No. 5, 1995, pp. 882-887.

[31] Schroeder, E., Baeder, J., "Using Computational Fluid Dynamics for Micro Air Vehicle Airfoil Validation and Prediction," *AIAA Applied Aerodynamics Conference*, Toronto, Canada, June 6-9, 2005.

[32] Winter, H., "Flow Phenomena on Plates and Airfoils of Short Span," *NACA Technical Report*, TR 539, 1935.

[33] Sathaye, S., Yuan, J., Olinger, D., "Lift Distributions on Low-Aspect-Ratio Wings at Low Reynolds Numbers for Micro-Air-Vehicle Applications," *AIAA Applied Aerodynamics Conference and Exhibit*, Providence, RI, Aug. 16-19, 2004.

[34] Pellettier, A., Mueller, T., "Low Reynolds Number Aerodynamics of Low Aspect Ratio Thin/Flat/Cambered-Plate Wings," *Journal of Aircraft*, Vol. 37, No. 5, 2000, pp. 825-832.

[35] Bartlett, G., Vidal, R., "Experimental Investigation of Influence of Edge Shape on the Aerodynamic Characteristics of Low Aspect Ratio Wings at Low Speeds," *Journal of Aeronautical Sciences*, Vol. 22, No. 8, 1955, pp. 517-533.

[36] Polhamus, E., "A Note on the Drag Due to Lift of Rectangular Wings of Low Aspect Ratio," *NACA Technical Report*, TR 3324, 1955.

[37] Kaplan, S., Altman, A., Ol, M., "Wake Vorticity Measurements for Low Aspect Ratio Wings at Low Reynolds Numbers," *Journal of Aircraft*, Vol. 44, No. 1, 2007, pp. 241-251.

[38] Viieru, D., Albertani, R., Shyy, W., Ifju, P., "Effect of Tip Vortex on Wing Aerodynamics of Micro Air Vehicles," *Journal of Aircraft*, Vol. 42, No. 6, 2005, pp. 1530-1536.

[39] Mueller, T., DeLaurier, J., "Aerodynamics of Small Vehicles," *Annual Review of Fluid Mechanics*, Vol. 35, No. 35, 2003, pp. 89-111.

[40] Gursul, I., Taylor, G., Wooding, C., "Vortex Flows Over Fixed-Wing Micro Air Vehicles," *AIAA Aerospace Sciences Meeting and Exhibit*, Reno, NV, January 14-17, 2002.

[41] Cosyn, P., Vierendeels, J., "Numerical Investigation of Low-Aspect-Ratio Wings at Low Reynolds Numbers," *Journal of Aircraft*, Vol. 43, No. 3, 2006, pp. 713-722.

[42] Brion, V., Aki, M., Shkarayev, S., "Numerical Simulation of Low Reynolds Number Flows Around Micro Air Vehicles and Comparison against Wind Tunnel Data," *AIAA Applied Aerodynamics Conference*, San Francisco, CA, June 5-8, 2006.

[43] Stanford, B., Sytsma, M., Albertani, R., Viieru, D., Shyy, W., Ifju, P., "Static Aeroelastic Model Validation of Membrane Micro Air Vehicle Wings," *AIAA Journal*, Vol. 45, No. 12, 2007, pp. 2828-2837.

[44] Zhan, J., Wang, W., Wu, Z., Wang, J., "Wind-Tunnel Experimental Investigation on a Fix-Wing Micro Air Vehicle," *Journal of Aircraft*, Vol. 43, No. 1, 2006, pp. 279-283.

[45] Ramamurti, R., Sandberg, W., Löhner, R., "Simulation of the Dynamics of Micro Air Vehicles," *AIAA Aerospace Sciences Meeting and Exhibit*, Reno, NV, January 10-13, 2000.

[46] Gyllhem, D., Mohseni, K., Lawrence, D., "Numerical Simulation of Flow Around the Colorado Micro Aerial Vehicle," *AIAA Fluid Dynamics Conference and Exhibit*, Toronto, Canada, June 6-9, 2005.

[47] Albertani, R., "Experimental Aerodynamics and Elastic Deformation Characterization of Low Aspect Ratio Flexible Fixed Wings Applied to Micro Aerial Vehicles," Ph.D. Dissertation, Department of Mechanical and Aerospace Engineering, University of Florida, Gainesville, FL, 2005.

[48] Morris, S., "Design and Flight Test Results for Micro-Sized Fixed Wing and VTOL Aircraft," *International Conference on Emerging Technologies for Micro Air Vehicles*, Atlanta, GA, February 3-5, 1997.

[49] Rais-Rohani, M., Hicks, G., "Multidisciplinary Design and Prototype Development of a Micro Air Vehicle," *Journal of Aircraft*, Vol. 36, No. 1, 1999, pp. 227-234.

[50] Kajiwara, I., Haftka, R., "Simultaneous Optimal Design of Shape and Control System for Micro Air Vehicles," *AIAA Structures, Structural Dynamics, and Materials Conference,* St. Louis, MO, April 12-15, 1999.

[51] Lundström, D., Krus, P., "Micro Aerial Vehicle Design Optimization using Mixed Discrete and Continuous Variables," *AIAA/ISSMO Multidisciplinary Analysis and Optimization Conference*, Portsmouth VA, September 6-8, 2006.

[52] Ng, T., Leng, G., "Application of Genetic Algorithms to Conceptual Design of a Micro Air Vehicle," *Engineering Applications of Artificial Intelligence*, Vol. 15, No. 5, 2003, pp. 439-445.

[53] Sloan, J., Shyy, W., Haftka, R., "Airfoil and Wing Planform Optimization for Micro Air Vehicles," *Symposium of RTO Applied Vehicle Technology Panel*, Ottawa, Canada, October 19-21, 1999.

[54] Lian, Y., Shyy, W., Haftka, R., "Shape Optimization of a Membrane Wing for Micro Air Vehicles," *AIAA Journal*, Vol. 42, No. 2, 2004, pp. 424-426.

[55] Boria, F., Stanford, B., Bowman, W., Ifju, P., "Evolutionary Optimization of a Morphing Wing with Wind Tunnel Hardware-in-the-Loop," *Aerospace Science and Technology*, submitted for publication.

[56] Hunt, R., Hornby, G., Lohn, J., "Toward Evolved Flight," *Genetic and Evolutionary Computation Conference*, Washington, DC, June 25-29, 2005.

[57] Day, A., "Optimization of a Micro Aerial Vehicle Planform Using Genetic Algorithms," Masters Thesis, Department of Mechanical Engineering, Worcester Polytechnic Institute, Worcester, MA, 2007.

[58] Fitt, A., Pope, M., "The Unsteady Motion of Two-Dimensional Flags With Bending Stiffness," *Journal of Engineering Mechanics*, Vol. 40, No. 3, 2001, pp. 227-248.

[59] Wilkinson, M, "Sailing the Skies: the Improbable Aeronautical Success of the Pterosaurs," *Journal of Experimental Biology*, Vol. 210, No. 10, 2007, pp. 1663-1671.

[60] Bisplinghoff, R., Ashley, H., Halfman, R., *Aeroelasticity*, Dover, Mineola, NY, 1955.

[61] Stanford, B., Abdulrahim, M., Lind, R., Ifju, P., "Investigation of Membrane Actuation for Roll Control of a Micro Air Vehicle," *Journal of Aircraft*, Vol. 44, No. 3, 2007, pp. 741-749.

[62] Argentina, M., Mahadevan, L., "Fluid-Flow-Induced Flutter of a Flag," *Proceedings of the National Academy of Science: Applied Mathematics*, Vol. 102, No. 6, 2005, pp. 1829-1834.

[63] Alben, S., Shelley, M., Zhang, J., "How Flexibility Induces Streamlining in a Two-Dimensional Flow," *Physics of Fluids*, Vol. 16, No. 5, 2004, pp. 1694-1713.

[64] Voelz, K., "Profil und Auftrieb Eines Segels," *Zeitschrift f'ur Angewandte Mathematik und Mechanik*, Vol. 30, 1950, pp. 301-317.

[65] Thwaites, B., "The Aerodynamic Theory of Sails," *Proceedings of the Royal Society of London*, Vol. 261, No. 1306, 1961, pp. 402-422.

[66] Nielsen, J., "Theory of Flexible Aerodynamic Surfaces," *Journal of Applied Mechanics*, Vol. 30, No. 3, 1963, pp. 435-442.

[67] Haselgrove, M., Tuck, E., "Stability Properties of the Two-Dimensional Sail Model," *Society of Naval Architects and Marine Engineers New England Sailing Yacht Symposium*, New London, CN, January 24, 1976.

[68] Murai, H., Murayama, S., "Theoretical Investigation of Sailwing Airfoils Taking Account of Elasticities," *Journal of Aircraft*, Vol. 19, No. 5, 1982, pp.385-389.

[69] Jackson, P., "A Simple Model for Elastic Two-Dimensional Sails," *AIAA Journal*, Vol. 21, No. 1, 1983, pp.153-155.

[70] Sneyd, A., "Aerodynamic Coefficients and Longitudinal Stability of Sail Aerofoils," *Journal of Fluid Mechanics*, Vol. 149, No. 7, 1984, pp.127-146.

[71] Cyr, S., Newman, B., "Flow Past Two-Dimensional Membrane Aerofoils with Rear Separation," *Journal of Wind Engineering and Industrial Aerodynamics*, Vol. 63, No. 1, 1996, pp. 1-16.

[72] Smith, R., Shyy, W., "Computational Model of Flexible Membrane Wings in Steady Laminar Flow," *AIAA Journal*, Vol. 33, No. 10, 1995, pp. 1769-1777.

[73] Newman, B., Low H., "Two-Dimensional Impervious Sails: Experimental Results Compared with Theory," *Journal of Fluid Mechanics*, Vol. 144, 1984, pp. 445-462.

[74] Smith, R., Shyy, W., "Computation of Aerodynamic Coefficients for a Flexible Membrane Airfoil in Turbulent Flow: A Comparison with Classical Theory," *Physics of Fluids*, Vol. 8, No. 12, 1996, pp. 3346-3353.

[75] Lorillu, O., Weber, R., Hureau, J., "Numerical and Experimental Analysis of Two-Dimensional Separated Flows over a Flexible Sail," *Journal of Fluid Mechanics*, Vol. 466, 2002, pp. 319-341.

[76] Jackson, P., Christie, G., "Numerical Analysis of Three-Dimensional Elastic Membrane Wings," *AIAA Journal*, Vol. 25, No. 5, 1987, pp. 676-682.

[77] Sneyd, A., Bundock, M., Reid, D., "Possible Effects of Wing Flexibility on the Aerodynamics of Pteranodon," *The American Naturalist*, Vol. 120, No. 4, 1982, pp. 455-477.

[78] Boudreault, R., "3-D Program Predicting the Flexible Membrane Wings Aerodynamic Properties," *Journal of Wind Engineering and Industrial Aerodynamics*, Vol. 19, No. 1, 1985, pp. 277-283.

[79] Holla, V., Rao, K., Arokkiaswamy, A., Asthana, C., "Aerodynamic Characteristics of Pretensioned Elastic Membrane Rectangular Sailwings," *Computer Methods in Applied Mechanics and Engineering*, Vol. 44, No. 1, 1984, pp. 1-16.

[80] Sugimoto, T., "Analysis of Circular Elastic Membrane Wings," *Transactions of the Japanese Society of Aerodynamics and Space Sciences*, Vol. 34, No. 105, 1991, pp. 154-166.

[81] Charvet, T., Hauville, F., Huberson, S., "Numerical Simulation of the Flow Over Sails in Real Sailing Conditions," *Journal of Wind Engineering and Industrial Aerodynamics*, Vol. 63, No. 1, 1996, pp. 111-129.

[82] Schoop, H., Bessert, N., Taenzer, L., "On the Elastic Membrane in a Potential Flow," *International Journal for Numerical Methods in Engineering*, Vol. 41, No. 2, 1998, pp. 271-291.

[83] Stanford, B., Albertani, R., Ifju, P., "Static Finite Element Validation of a Flexible Micro Air Vehicle," *Experimental Mechanics*, Vol. 47, No. 2, 2007, pp. 283-294.

[84] Ferguson, L., Seshaiyer, P., Gordnier, R., Attar, P., "Computational Modeling of Coupled Membrane-Beam Flexible Wings for Micro Air Vehicles," *AIAA Structures, Structural Dynamics, and Materials Conference*, Honolulu, HI, April 23-26, 2007.

[85] Smith, R., Shyy, W., "Incremental Potential Flow Based Membrane Wing Element," *AIAA Journal*, Vol. 35, No. 5, 1997, pp. 782-788.

[86] Heppel, P., "Accuracy in Sail Simulation: Wrinkling and Growing Fast Sails," *High Performance Yacht Design Conference*, Auckland, New Zealand, December 4-6, 2002.

[87] Fink, M., "Full-Scale Investigation of the Aerodynamic Characteristics of a Model Employing a Sailwing Concept," *NASA Technical Report*, TR 4062, 1967.

[88] Greenhalgh, S., Curtiss, H., "Aerodynamic Characteristics of a Flexible Membrane Wing," *AIAA Journal*, Vol. 24, No. 4, 1986, pp. 545-551.

[89] Galvao, R., Israeli, E., Song, A., Tian, X., Bishop, K., Swartz, S., Breuer, K., "The Aerodynamics of Compliant Membrane Wings Modeled on Mammalian Flight Mechanics," *AIAA Fluid Dynamics Conference and Exhibit*, San Francisco, CA, June 5-8, 2006.

[90] Pennycuick, C., Lock, A., "Elastic Energy Storage in Primary Feather Shafts," *Journal of Experimental Biology*, Vol. 64, No. 3, 1976, pp. 677-689.

[91] Parks, H., "Three-Component Velocity Measurements in the Tip Vortex of a Micro Air Vehicle," Masters Thesis, School of Engineering and Management, Air Force Institute of Technology, Wright Patterson Air Force Base, OH, 2006.

[92] Gamble, B., Reeder, M., "Experimental Analysis of Propeller Interactions with a Flexible Wing Micro Air Vehicle," *AIAA Fluid Dynamics Conference and Exhibit*, San Francisco, CA, June 5-8, 2006.

[93] Stults, J., Maple, R., Cobb, R., Parker, G., "Computational Aeroelastic Analysis of a Micro Air Vehicle with Experimentally Determined Modes," *AIAA Applied Aerodynamics Conference*, Toronto, Canada, June 6-9, 2005.

[94] Ifju, P., Ettinger, S., Jenkins, D., Martinez, L., "Composite Materials for Micro Air Vehicles," *Society for the Advancement of Material and Process Engineering Annual Conference*, Long Beach, CA, May 6-10, 2001.

[95] Frampton, K., Goldfarb, M., Monopoly, D., Cveticanin, D., "Passive Aeroelastic Tailoring for Optimal Flapping Wings," *Proceedings of Conference on Fixed, Flapping, and Rotary Wing Vehicles at Very Low Reynolds Numbers*, South Bend, IN, June 5-7, 2000.

[96] Snyder, R., Beran, P., Parker, G., Blair, M., "A Design Optimization Strategy for Micro Air Vehicles," *AIAA Structures, Structural Dynamics, and Materials Conference*, Honolulu, HI, April 23-26, 2007.

[97] Allen, M., Maute, K., "Probabilistic Structural Design of UAVs under Aeroelastic Loading," *AIAA "Unmanned Unlimited" Conference*, San Diego, CA, September 15-18, 2003.

[98] Weisshaar, T., Nam, C., Batista-Rodriguez, A., "Aeroelastic Tailoring for Improved UAV Performance," *AIAA Structures, Structural Dynamics, and Materials Conference*, Long Beach, CA, April 20-23, 1998.

[99] Garrett, R., *The Symmetry of Sailing: The Physics of Sailing for Yachtsmen*, Adlard Coles, Dobbs Ferry, NY, 1996.

[100] Eden, M., *The Magnificent Book of Kites: Explorations in Design, Construction, Enjoyment, and Flight*, Sterling Publishing, New York, NY, 2002.

[101] Templin, R., Chatterjee, S., "Posture, Locomotion, and Paleoecology of Pterosaurs," Geological Society of America Special Paper 376, 2004.

[102] Swartz, S., Groves, M., Kim, H., Walsh, W., "Mechanical Properties of Bat Wing Membrane Skin," *Journal of Zoology*, Vol. 239, 1996, pp. 357-378.

[103] Norberg, U., "Bat Wing Structures Important for Aerodynamics and Rigidity," *Zoomorphology*, Vol. 73, No. 1, 1972, pp. 45-61.

[104] Levin, O., Shyy, W., "Optimization of a Low Reynolds Number Airfoil with Flexible Membrane," *Computer Modeling in Engineering and Sciences*, Vol. 2, No. 4, 2001, pp. 523-536.

[105] Zuo, K., Chen, L., Zhang, Y., Yang, J., "Study of Key Algorithms in Topology Optimization," *International Journal of Advanced Manufacturing Technology*, Vol. 32, No. 7, 2007, pp. 787-796.

[106] Maute, K., Reich, G., "Integrated Multidisciplinary Topology Optimization Approach to Adaptive Wing Design," *Journal of Aircraft*, Vol. 43, No. 1, 2006, pp. 253-263.

[107] Pingen, G., Evgrafov, A., Maute, K., "Topology Optimization of Flow Domains Using the Lattice Boltzmann Method," *Structural and Multidisciplinary Optimization*, Vol. 34, No. 6, 2007, pp. 507-524.

[108] Beckers, M., "Topology Optimization using a Dual Method with Discrete Variables," *Structural and Multidisciplinary Optimization*, Vol. 17, No. 1, 1999, pp. 14-24.

[109] Deb, K., Goel, T., "A Hybrid Multi-Objective Evolutionary Approach to Engineering Shape Design," *International Conference on Evolutionary Multi-Criterion Optimization*, March 7-9, Zurich, Switzerland, 2001.

[110] Maute, K., Nikbay, M., Farhat, C., "Sensitivity Analysis and Design Optimization of Three-Dimensional Non-Linear Aeroelastic Systems by the Adjoint Method," *International Journal for Numerical Methods in Engineering*, Vol. 56, No. 6, 2002, pp. 911-933.

[111] Min, S., Nishiwaki, S., Kikuchi, N., "Unified Topology Design of Static and Vibrating Structures Using Multiobjective Optimization," *Computers and Structures*, Vol. 75, No. 1, 2000, pp. 93-116.

[112] Borrvall, T., Petersson, J., "Topology Optimization of Fluids in Stokes Flow," *International Journal for Numerical Methods in Fluids*, Vol. 41, No. 1, 2003, pp. 77-107.

[113] Balabanov, V., Haftka, R., "Topology Optimization of Transport Wing Internal Structure," *Journal of Aircraft*, Vol. 33, No. 1, 1996, pp. 232-233.

[114] Eschenauer, H., Olhoff, N., "Topology Optimization of Continuum Structures: A Review," *Applied Mechanics Reviews*, Vol. 54, No. 4, 2001, pp. 331-390.

[115] Krog, L., Tucker, A. Kemp, M., "Topology Optimization of Aircraft Wing Box Ribs," *AIAA/ISSMO Multidisciplinary Analysis and Optimization Conference*, Albany, NY, August 30-September 1, 2004.

[116] Luo, Z., Yang, J., Chen, L., "A New Procedure for Aerodynamic Missile Designs Using Topological Optimization Approach of Continuum Structures," *Aerospace Science and Technology*, Vol. 10, No. 5, 2006, pp. 364-373.

[117] Santer, M., Pellegrino, S., "Topology Optimization of Adaptive Compliant Aircraft Leading Edge," *AIAA Structures, Structural Dynamics, and Materials Conference*, Honolulu, HI, April 23-26, 2007.

[118] Maute, K., Allen, M., "Conceptual Design of Aeroelastic Structures by Topology Optimization," *Structural and Multidisciplinary Optimization*, Vol. 27, No. 1, 2004, pp. 27-42.

[119] Martins, J., Alonso, J., Reuther, J., "Aero-Structural Wing Design Optimization Using High-Fidelity Sensitivity Analysis," *Confederation of European Aerospace Societies Conference on Multidisciplinary Analysis and Optimization*, Cologne, Germany, June 25-26, 2001.

[120] Gomes, A., Suleman, A., "Optimization of Aircraft Aeroelastic Response Using the Spectral Level Set Method," *AIAA Structures, Structural Dynamics, and Materials Conference*, Austin, TX, April 18-21, 2005.

[121] Combes, S., Daniel, T., "Flexural Stiffness in Insect Wings: Scaling and Influence of Wing Venation," *The Journal of Experimental Biology*, Vol. 206, No. 6, 2003, pp. 2979-2987.

[122] Marchman, J., "Aerodynamic Testing at Low Reynolds Numbers," *Journal of Aircraft*, Vol. 24, No. 2, 1987, pp. 107-114.

[123] Recommended Practice R-091-2003, "Calibration and Use of Internal Strain-Gage Balances with Application to Wind Tunnel Testing," AIAA, Reston, VA, 2003.

[124] Kochersberger, K., Abe, C., "A Novel, Low Reynolds Number Moment Balance Design for Micro Air Vehicle Research," *AIAA Fluid Dynamics Conference and Exhibit*, Toronto, Canada, June 6-9, 2005.

[125] Moschetta, J., Thipyopas, C., "Aerodynamic Performance of a Biplane Micro Air Vehicle," *Journal of Aircraft*, Vol. 44, No. 1, 2007, pp. 291-299.

[126] Mueller, T., "Aerodynamic Measurements at Low Reynolds Numbers for Fixed Wing Micro-Air Vehicles," *RTO Special Course on the Development and Operation of UAVs for Military and Civil Applications*, Von Karman Institute, Belgium, September 13-17, 1999.

[127] Kline, S., McClintock, F., "Describing Uncertainties in Single-Sample Experiments," *Mechanical Engineering*, Vol. 75, No. 1, 1953, pp. 3-8.

[128] Pankhurst, R., Holder, D., *Wind Tunnel Technique*, Sir Isaac Pitman and Sons, London, UK, 1952.

[129] Barlow, J., Rae, W., Pope, A., *Low-Speed Wind Tunnel Testing*, Wiley, New York, NY, 1999.

[130] Fleming, G., Bartram, S., Waszak, M., Jenkins, L., "Projection Moiré Interferometry Measurements of Micro Air Vehicle Wings," SPIE Paper 4448-16.

[131] Burner, A., Fleming, G., Hoppe, J., "Comparison of Three Optical Methods for Measuring Model Deformation," *AIAA Aerospace Sciences Meeting and Exhibit*, Reno, NV, January 10-13, 2000.

[132] Sutton, M., Turner, J., Bruck, H., Chae, T., "Full Field Representation of the Discretely Sampled Surface Deformation for Displacement and Strain Analysis," *Experimental Mechanics*, Vol. 31, No. 2, 1991, pp. 168-177.

[133] Schreier, H., Braasch, J., Sutton, M., "Systematic Errors in Digital Image Correlation caused by Intensity Interpolation," *Optical Engineering*, Vol. 39, No. 11, 2000, pp. 2915-2921.

[134] Sutton, M., McFadden, C., "Development of a Methodology for Non-Contacting Strain Measurements in Fluid Environments Using Computer Vision," *Optics and Lasers in Engineering*, Vol. 32, No. 4, 2000, pp. 367-377.

[135] Albertani, R., Stanford, B., Sytsma, M., Ifju, P., "Unsteady Mechanical Aspects of Flexible Wings: an Experimental Investigation Applied to Biologically Inspired MAVs," *European Micro Air Vehicle Conference and Flight Competition*, Toulouse, France, September 17-21, 2007.

[136] Batoz, J., Bathe, K., Ho, L., "A Study of Three-Node Triangular Plate Bending Elements," *International Journal for Numerical Methods in Engineering*, Vol. 15, No. 12, 1980, pp. 1771-1812.

[137] Cook, R., Malkus, D., Plesha, M., Witt, R., *Concepts and Applications of Finite Element Analysis*, Wiley, New York, NY, 2002.

[138] Reaves, M., Horta, L., Waszak, M., Morgan, B., "Model Update of a Micro Air Vehicle (MAV) Flexible Wing Frame with Uncertainty Quantification," *NASA Technical Memorandum*, TM 213232, 2004.

[139] Isenberg, C., *The Science of Soap Films and Soap Bubbles*, Dover, New York, NY, 1992.

[140] Pujara, P., Lardner, T., "Deformations of Elastic Membranes – Effect of Different Constituitive Relations," *Zeitschrift für Angewandte Mathematik und Physik*, Vol. 29, No. 2, 1978, pp. 315-327.

[141] Small, M., Nix, W., "Analysis of the Accuracy of the Bulge Test in Determining the Mechanical Properties of Thin Films," *Journal of Materials Research*, Vol. 7, No. 6, 1992, pp. 1553-1563.

[142] Pauletti, R., Guirardi, D., Deifeld, T., "Argyris' Natural Finite Element Revisited," *International Conference on Textile Composites and Inflatable Structures*, Stuttgart, Germany, October 2-5, 2005.

[143] Lian, Y., Shyy, W., Ifju, P., Verron, E., "A Computational Model for Coupled Membrane-Fluid Dynamics," *AIAA Fluid Dynamics Conference and Exhibit*, St. Louis, MO, June 24-26, 2002.

[144] Wu, B., Du, X., Tan, H., "A Three-Dimensional FE Nonlinear Analysis of Membranes," *Computers and Structures*, Vol. 59, No. 4, 1996, pp. 601-605.

[145] Campbell, J., "On the Theory of Initially Tensioned Circular Membranes Subjected to Uniform Pressure," *Quarterly Journal of Mechanics and Applied Mathematics*, Vol. 9, No. 1, 1956, pp. 84-93.

[146] Mase, G., Mase, G., *Continuum Mechanics for Engineers*, CRC Press, Boca Raton, FL, 1999.

[147] Stanford, B., Boria, F., Ifju, P., "The Validity Range of Pressurized Membrane Models with Varying Fidelity," *Society for Experimental Mechanics*, Springfield, MA, June 4-6, 2007.

[148] Tannehill, J., Anderson, D., Pletcher, R., *Computational Fluid Mechanics and Heat Transfer*, Taylor and Francis, Philadelphia, PA, 1997.

[149] Shyy, W., *Computational Modeling for Fluid Flow and Interfacial Transport*, Elsevier, Amsterdam, The Netherlands, 1994.

[150] Thakur, S., Wright, J., Shyy, W., "STREAM: A Computational Fluid Dynamics and Heat Transfer Navier-Stokes Solver: Theory and Applications," Streamline Numerics, Inc., Gainesville, FL, 2002.

[151] Lewis, W., *Tension Structures: Form and Behavior*, Thomas Telford Ltd, London, UK, 2003.

[152] Kamakoti, R., Lian, Y., Regisford, S., Kurdila, A., Shyy, W., "Computational Aeroelasticity Using a Pressure-Based Solver," *Computer Methods in Engineering and Sciences*, Vol. 3, No. 6, 2002, pp. 773-790.

[153] Sytsma, M., "Aerodynamic Flow Characterization of Micro Air Vehicles Utilizing Flow Visualization Methods," Masters Thesis, Department of Mechanical and Aerospace Engineering, University of Florida, Gainesville, FL, 2006.

[154] Hepperle, M., "Aerodynamics of Spar and Rib Structures," *MH AeroTools Online Database*, http://www.mh-aerotools.de/airfoils/ribs.htm, March 2007.

[155] Gürdal, Z., Haftka, R., Hajela, P., *Design and Optimization of Laminated Composites Materials*, Wiley, New York, NY, 1999.

[156] Deb, K., Pratap, A., Agarwal, S., Meyarivan, T., "A Fast and Elitist Multiobjective Genetic Algorithm: NSGA-II," *IEEE Transactions on Evolutionary Computation*, Vol. 6, No. 2, 2002, pp. 182-197.

[157] Antony, J., *Design of Experiments for Engineers and Scientists*, Butterworth-Heinemann, Boston, MA, 2003.

[158] Chen, T., Wu, S., "Multiobjective Optimal Topology Design of Structures," *Computational Mechanics*, Vol. 21, No. 6, 2998, pp. 483-492.

[159] Haftka, R., Gürdal, Z, *Elements of Structural Optimization*, Kluwer, Dordrecht, The Netherlands, 1992.

[160] Maute, K., Nikbay, M., Farhat, C., "Coupled Analytical Sensitivity Analysis and Optimization of Three-Dimensional Nonlinear Aeroelastic Systems," *AIAA Journal*, Vol. 39, No. 11, 2001, pp. 2051-2061.

[161] Lyu, N., Saitou, K., "Topology Optimization of Multicomponent Beam Structure via Decomposition-Based Assembly Synthesis," *Journal of Mechanical Design*, Vol. 127, No. 2, 2005, pp. 170-183.

[162] Hsu, M., Hsu, Y., "Interpreting Three-Dimensional Structural Topology Optimization Results," *Computers and Structures*, Vol. 83, No. 4, 2005, pp. 327-337.

[163] Rohl, P., Schrage, D., Mavris, D., "Combined Aerodynamic and Structural Optimization of a High-Speed Civil Transport Wing," *AIAA Structures, Structural Dynamics, and Materials Conference*, New Orleans, LA, April 18-21, 1995.

BIOGRAPHICAL SKETCH

Bret Kennedy Stanford was born in Richmond, Virginia on September 30, 1981, though his grandmother claims it was on September 29. School was never really an option for young Bret, forced by his parents at an early age to join the circus instead. He was taught to read, write, and juggle by a kindly group of clowns, despite his extreme terror of anything with big floppy shoes, a phobia which continues unabated to this day. Bret was reunited with his parents two years later, an act which was prompted by a recent increase in the Child Tax Credit. Several brush-ins with the law led to the Stanford family's expulsion from Virginia, escorted to the North Carolina border by a group of unsympathetic state troopers. The family subsequently relocated to Tampa, Florida in the fall of 1988, though Bret's grandmother claims it was in the summer.

Bret's time in Tampa was mostly spent selling hand-carved limestone trinkets and jewelry to tourists. At the age of 17, he was rejected from most of the universities along the eastern seaboard, who were collectively unimpressed with his artesian and entertainment backgrounds. A clerical error granted him acceptance to the University of Florida. He arrived in Gainesville in the fall of 1999 (a date his grandmother generally agrees upon) with the intent of studying French post-modern theatre. Nine convoluted years later he received his doctorate in aerospace engineering. Upon graduation, he plans on throwing all of his newfound knowledge, books, and lab journals into the River, in order to start a Beach Boys cover band. He hopes that his advisor will handle all of the journal review replies as they come back from the editors, so the research will not have gone to waste.